2 Euratom fusion programme

2.1 Theory and Modelling

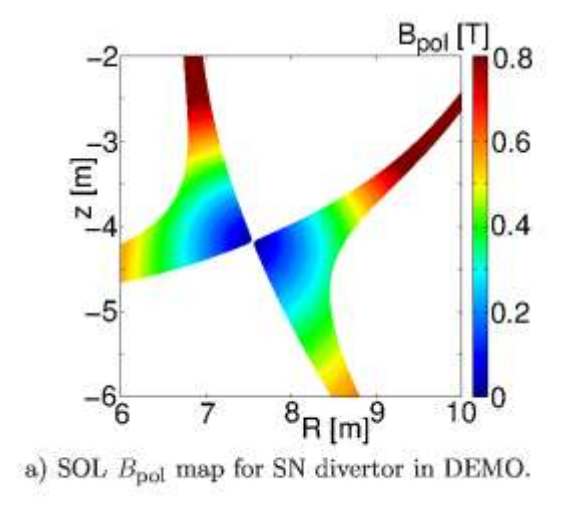
TECXY code simulation of the snowflake divertor configuration in DEMO reactor

Principal investigator:
R. Zagórski, <u>roman.zagorski@ifpilm.pl</u>
Collaborators from the Institute of Plasma Physics and Laser Microfusion:
G. Pełka, W. Stępniewski

Introduction

A snowflake (SF) divertor configuration, proposed in [1], has been proposed as a mean of lenghtening the life span of divertor plates. Now, we have obtained preliminary results of a SN vs. SF comparison in case of DEMO reactor for no impurity scrape-off layer plasma. The TECXY code used has also proved valid for the cases with impurity seeding. Here we present a shorthand version of our work [2] that is to be published in the PET-14 workshop proceedings.

The main difference between ordinary SN and SF divertor configuration is that the value of poloidal magnetic field B_{pol} has higher (second) order null in the X-point for the SF. As a result the area where $B_{pol}\approx 0$ is larger in the SF divertor (to be compared in fig. 1). Plasma spends a lot of time circulating close to X-point and may effectively spread energy to neutrals.



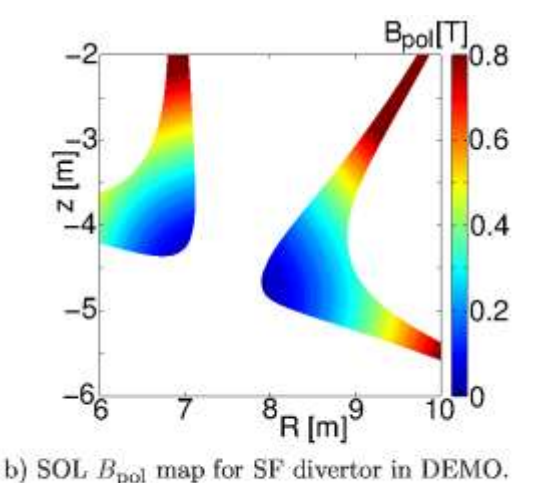


Fig. 1. The coordinates are: major radius R and height z.

Perfect snowflake configuration is a topologically unstable [3]. In practice, it is going to be deliberately slightly distorted, having two first order B_{pol} nulls located close to each other, instead of one second order null. The 'imperfection' does not alter the above-mentioned potential advantage of SF divertor. Our computations were performed for such a quasi-SF configuration.

We conducted density scans of scrape-off layer for SF and SN divertors in DEMO reactor. The results for the D-T mixture show up to 2.5 time heat load reduction around the strike point on the outer target divertor plate. The most probable mechanism of plasma cooling is neutral atoms radiation. Preliminary simulations of Ne-seeded discharges were also performed. Further work is essential but SF configuration already seems promissing.

DEMO1 parameters and simulation details

Our computations were done for the DEMO1 parameter set. [4]

Deuterium-tritium only simulations

Just as it was done for FAST [5], as an entry point we do not include impurities in the main part of our simulation. In fact, a strong radiation both from the core and SOL impurities was to be expected. Indeed, intensive tungsten core radiation had been predicted [6]. To account for that effect, we set the power flowing to SOL to P_{SOL} = 100 MW \approx 13% (P_{th} - P_{fus} + P_{fus} /5) in our model. Altogether 12 cases were studied.

Neon-seeded symulations

We considered a few cases of neonium-seeded discharges: impurity concentration was equal to $2.6615 \cdot 10^{-2}$, $P_{SOL}=100$ MW, $D_{\perp}=0.5$ m²/s; recycling, D_{\perp}/χ_{\perp} and a few other, minor parameters were fixed as above. Our aim was to prove the code can be successfully applied to simulate externally seeded SOL.

The TECXY code and meshes

The fast and easily applicable 2D code TECXY [7] computes steady-state solutions for the tokamak scrape-off layer (SOL). The code is based on a fluid model, where electrons and ions are treated as separate fluids. Energy and particle fluxes leaving the core through separatrix and recycling coefficient are fixed prior to computations. The transport along field lines is computed from Braginskii equations.

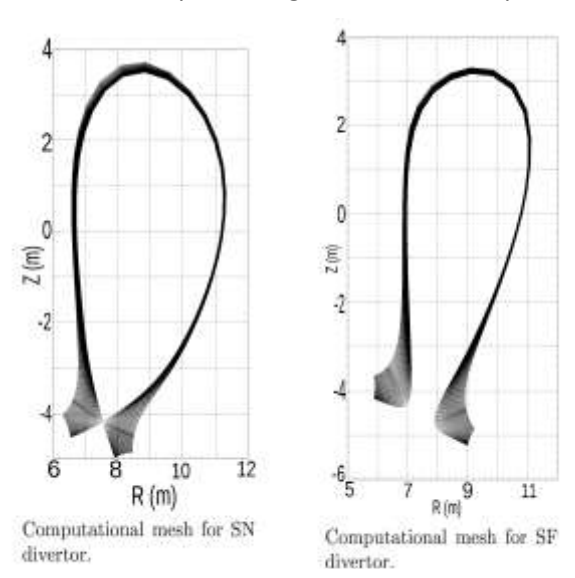


Fig. 2. The coordinates are: major radius R height z.

The neutrals are treated in a simplified way—an analytical model of their distribution is assumed. This simplified treatment makes detachment regime, where neutrals dynamics is of major importance, inaccessible for the code.

Computational meshes for both SN and SF configurations are presented in fig. 2. They were produces according to magnetic field found by ENEA group (see fig. 1). Curvilinear grids follow the shape of flux surfaces.

Results

General simulation results

There are generic facts we recognised when we compared SN and SF results case by case—see fig. 4. The peak q generally diminishes and the total number of neutral atoms rises with rising $n_{e,\text{sep}}$. For equal D_{\perp} and $n_{e,\text{sep}}$ SF simulations always yielded higher (but <11% higher) particle flux crossing separatrix, higher total neutral atom number (only \approx 20% higher for small densities, but almost 3 times higher for D_{\perp} = 0.5m²/s and $n_{e,\text{sep}}$ =3.85·10¹⁹ m⁻³) and stronger overall SOL plasma radiation.

Plasma parameters profiles

We focused our discussion on the vicinity of the strike point on the outer target plate—the area hardest-hit by particle and heat fluxes.

The distance particles have to travel before reaching divertor plate is roughly equal to the magnetic connection length $L \propto 1/\langle B_{pol} \rangle$ where the averaging takes place over the field line length. The longer they travel the more energy they can radiate out due to interactions with neutrals. Our results confirm this picture.

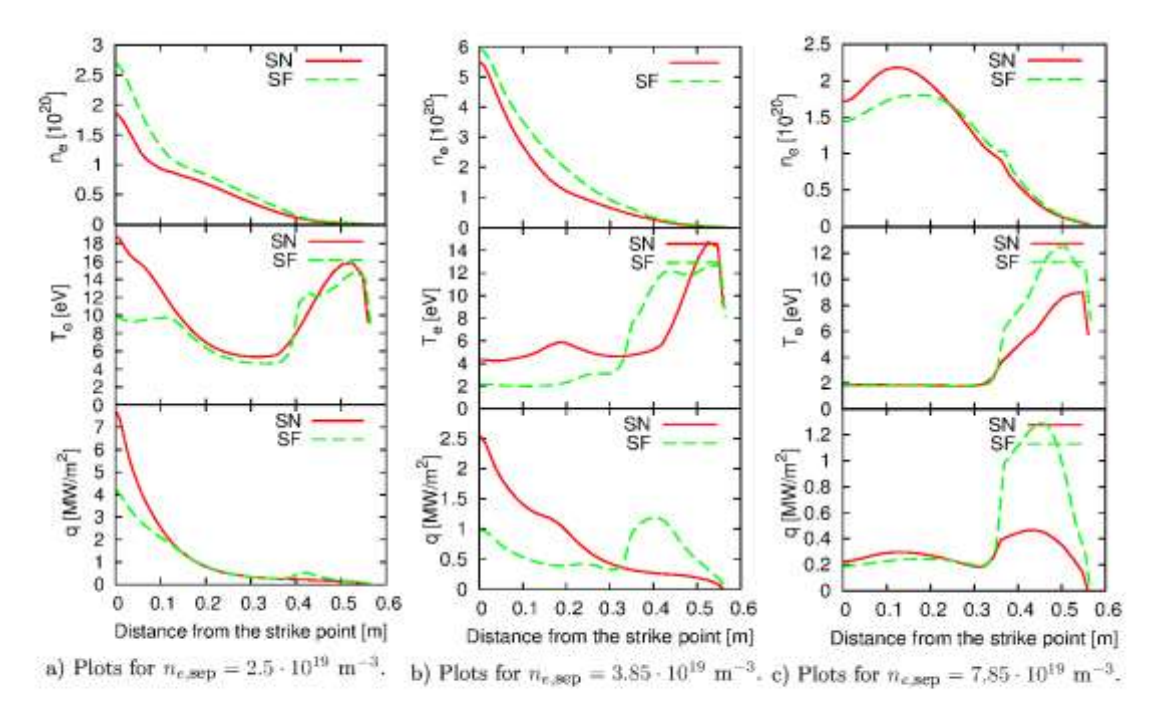


Fig. 4. Outer divertor n_e, T_e and heat load q profiles for the case of D_{\perp} = 0.5 m²/s.

Geometrical effect

Magnetic field lines, which guide particles, spread them over the plate according shape the lines have. This spreading difference we call the geometrical effect. Heat load reduction due to geometry only was estimated by the ENEA group: $f_{q,\,\mathrm{geom}}$ =0.855, 0.87, 0.88, 0.89 for flux tubes gradually farther and farther away from the separatrix. It means that, in the currently studed settings, the geometrical effect favours the SN divertor. Further work is needed since computations (e.g. for FAST [5]) show that SF can be geometrically better than SN.

Ne-seeded discharges

After a number of successful runs we completed some comparatory material; that is, we simulated Neseeded and no-impurity discharges for D_{\perp} =0.5 m²/s and P_{SOl} =100 MW. The density was $n_{e,\text{sep}}$ =1.23·10¹⁹ m⁻³ in the SF case (fig. 5a) and $n_{e,\text{sep}}$ =1.36·10¹⁹ m⁻³ for SN divertor (fig. 5b). Both are

where calculated in rectangular geometry, the arbitary coordinate is similar, but not equal to the 'distance along the divertor plate' we used earlier.

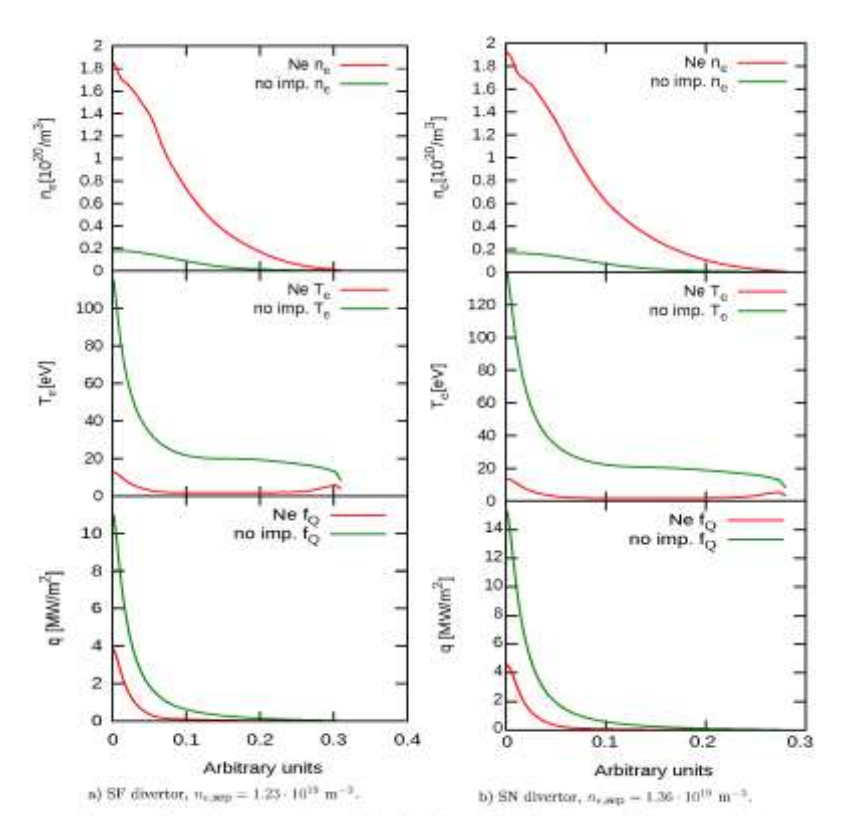


Fig. 5.Outer divertor n_e, T_e and heat load q profiles for the case of D_{\perp} = 0.5 m²/s.

Conclusions

The SF divertor performs up to 2.5 times better than SN as far as heat flux density mitigation is concerned—compare on fig. 4. The plasma cooling in case of snowflake divertor is particularly advantageous over the SN case for DEMO-relevant separatrix densities. The effect cannot be ascribed to favourable geometry (on the contrary, $f_{q,geom}<1$), and is likely caused by increased divertor-region neutral radiation. The SF configuration picked is still not optimal and needs improving, but the simulation results are already promising. The code is ready to scan parameter space for both non-seeded and seeded discharges.

Collaboration

The input for this work and geometrical effect calculations were provided by ENEA, Frascati, Italy group headed by prof. Ridolfini.

References

- [1] D.D. Yutov Geometrical properties of a "snowflake" divertor, Physics of Plasmas **14**(6), 064502 (2007).
- [2] G. Pełka, R. Zagórski, V. Pericoli Ridolfini, G. Artasere, G. Calabro, F. Crisanti, G. Maddaluno, G. Ramogida, and B. Viola, TECXY code simulation of snowflake divertor configuration in DEMO reactor Contribution to Plasma Physics, to be published in the Proceedings of PET-14 workshop (Cracow, 2013).
- [3] D.D. Ryutov, M.A. Makowski, and M.V. Umansky, Local properties of the magnetic field in a snowflake divertor, Plasma Physics and Controlled Fusion **52**(10), 105001 (2010).

- [4] D. Ward and R. Kemp, Demo baselines 23/5/13, Tech. rep., CCFE, 2013.
- [5] V.P. Ridolfini, R. Zagórski, G. Artaserse, G. Calabro, F. Crisanti, G. Maddaluno, G. Ramogia, and B. Viola, Comparativestudy of a conventional and snowflake divertor for the {FAST} (fusion advanced studies torus) tokamak, Journal of Nuclear Materials **438**, **Supplement**(0), S414–S417 (2013), Proceedings of the International Conference on Plasma-Surface Interactions in Controlled Fusion Devices.
- [6] R. Zagórski, I. Ivanova-Stanik, and R. Stankiewicz, Simulations with the COREDIV code of demo discharges, Nuclear Fusion **53**(7), 073030 (2013).
- [7] R. Zagórski http://www.efda-itm.eu/itm/imports/codcat/exhaust/modelling/tecxy.htm, Tech. rep., IPPLM, 2004.

Numerical simulations with the COREDIV code of plasma parameters in the WEST tokamak

Principal investigator:

I. Ivanova-Stanik; <u>irena.ivanova-stanik@ipplm.pl</u>

Collaborator from the Institute of Plasma Physics and Laser Microfusion:

R. Zagórski

Introduction

The WEST (Tungsten(W) Environment in Steady-state Tokamak) project is based on an upgrade of Tore Supra, transforming it in X point divertor device with tungsten targets [1]. The divertor is a critical component for fusion devices, which must handle the highest thermal and particle loads in the vessel. The WEST configuration aims at providing for the first time the capability to test ITER-relevant actively cooled plasma facing components under realistic plasma conditions. This requires in particular stationary heat flux densities of 10 MW/m² or higher, with plasma temperatures compatible with W operation. A simple power balance, with the heating capabilities installed on WEST (essentially 9MW of Ion Cyclotron Resonance Heating (ICRH) and 7 MW of LHCD (Lower Hybrid Current Drive) and in addition 0.7 MW of Electron Cyclotron Resonance Heating (ECRH)) show, shows that ITER relevant peak heat fluxes are within reach [1]. The present work focuses on W compatibility, using the self consistent core-edge code COREDIV [2]. Next, we investigate the importance of core-edge coupling in WEST in the presence of light impurities, whose effect is considered. Finally we conclude and discuss the perspectives of this work.

The importance of core-edge coupling in the WEST tokamak via tungsten production and core radiation is investigated with COREDIVcode. We first focus on the idealized situation where the plasma is free of light impurities, and show that for achievable high density discharges tungsten production can be essentially extinguished. For lower densities, core edge coupling is strong, that is tungsten plays a major role in regulating the power flowing through the Scrape-off layer. The latter is found to saturate with increasing heating power due to increasing radiation losses in the core. Then we investigate the extent to which light impurities change this picture by performing a scan in boron concentration, since Ion Cyclotron Resonance Heating antenna protection will be boron coated.

Physics of the COREDIV model

The COREDIV code solves self-consistently the Scrape-off Layer (SOL) and core dynamics, using respectively a 2D and a 1D model. The global solution is obtained by iterating between the core and edge parts until convergence is achieved. In order to make this procedure tractable in practice, both core and edge models have to kept reasonably simple and focused on the problem of interest here, that is core-edge coupling effects mediated by impurities. In the core, 1D radial transport equations are solved for main ions as well as for all ionization stages of impurity species. The temperature of all ions are assumed to be equal. The cross field heat conductivities at radius r are such that $\chi_{i,e}(r) = C_{i,e} a^2 / \tau_E \times F(r)$ [3], where a = 0.41 m is the minor radius and τ_E the energy confinement time. The latter follows the ELMy H-mode scaling law [4], and the pre-factors $C_{e;i}$ are set so that the actual confinement time is consistent with the scaling law. The particle transport coefficients for the main ion and electrons are such that $D_i = 0.1\chi_e$. In the simulations presented here, the pinch velocity for impurity transport does not include the neoclassical contribution, and is taken as $V_{pinch} \propto \tau_E^2 D_i r / a^2$. This precludes impurity accumulation in the core, which we suppose is controlled by core electron heating (ECRH and/or ICRH) [5]. The ion source term is of the form $S_i(r) = S_{i0} \exp(-(\alpha - r)\lambda_{i0})$, where λ_{i0} is an effective ionization mean free path. The value of S_{io} is determined iteratively in such a way that the average density reaches the value prescribed as input. In the SOL, COREDIV relies on the 2D multi-fluid EPIT code (e.g. [6]). Neutrals are treated analytically (in a two group model for deuterium), and originate either from recycling, sputtering, or gas puff. The geometry used here is slab, and assumes inner-outer symmetry with the stagnation point in the mid plane. Parallel transport is classical while anomalous perpendicular transport is described by diffusion coefficients such that $D_i^{SOL} = \chi_i^{SOL} = 0.5\chi_e^{SOL}$ = 0.25 m²/s. Continuity of particle and energy fluxes, as well as of densities and temperatures is imposed at the separatrix. The fluxes computed by the core transport solver are imposed as boundary conditions to the edge solver, while the temperatures and densities obtained from the latter are subsequently used for the core solver. COREDIV results have been compared to AUG and JET experiments quite successfully [7,8], and the code used here is the same (only the geometrical parameters have been modified).

Core-edge coupling without light impurities

The major and minor radiuses for WEST are respectively R=2.55 m and a=0.41 m. We consider an operating scenario with B=3.7 T, $I_p=776$ kA, $q_{95}=3$ at the edge, and an average density of $< n_e > = 6$ x10¹⁹ m⁻³ = 0.4 n_{GW} (where n_{GW} is the Greenwald density). The separatrix density is set such that $n^{\rm sep}_{e}=3$ x10¹⁹ m⁻³, in accordance with the assumptions used in Ref. [8] to model AUG discharges. We further assume that $H_{98}=0.8$ for all cases considered here. The sensitivity to these assumptions will be discussed at the end of the section. We first neglect the effects of light impurities (such as C, O, ...) which are always present to some extent in fusion devices. The latter are known to play an important role in W machines (e.g. [9])], but in order to disentangle the different physical mechanisms at play in the simulations it is useful to first ignore them.

Since the geometry used in the edge module of COREDIV is a slab, we focus on the total power reaching the divertor plates P^{plate} rather than on the heat flux density Q. In the conditions considered here the L-H threshold is 4MW (using the scaling law in Ref. [10]). We thus consider an auxiliary power scan from $P_{aux} = 6$ MW to 15MW, and plot the main plasma parameters on Fig. 1. For $P_{aux} > 10$ MW, the core radiation start to rise at a pace slightly below 1 MW per MW injected. The power crossing the separatrix, and ultimately the power to the plate thus show a strong saturation around 10 MW with increasing P_{aux} (compare the evolution of P^{plate}). In fact, by adding 5 MW to the plasma, P^{plate} rises only of ~1.2 MW. This saturation clearly results from W contamination, since radiation losses from the core exclusively come for W in these simulations. The W concentration in the core, C_W , is plotted versus P_{aux} on Fig. 1c, and increases roughly fivefold when P_{aux} increases from 10 to 15 MW.This is essentially a source effect, rather than a SOL screening effect, since as shown again on Fig. 1c, where the W influx from the divertor Γ_W increases by a

comparable factor. As already discussed in Ref. [8, 9], this behaviour essentially stems from the very strong temperature dependence of the sputtering yield. Fig. 1d compares the plasma temperatures at the divertor plate. In the latter case, the temperatures obtained are such that W would be strongly eroded, and the resulting core radiation brings down these temperatures to a self-regulated level by reducing the power flowing to the SOL. In all cases presented here, W is predominantly produced by selfsputtering because of the still fairly large edge temperatures.

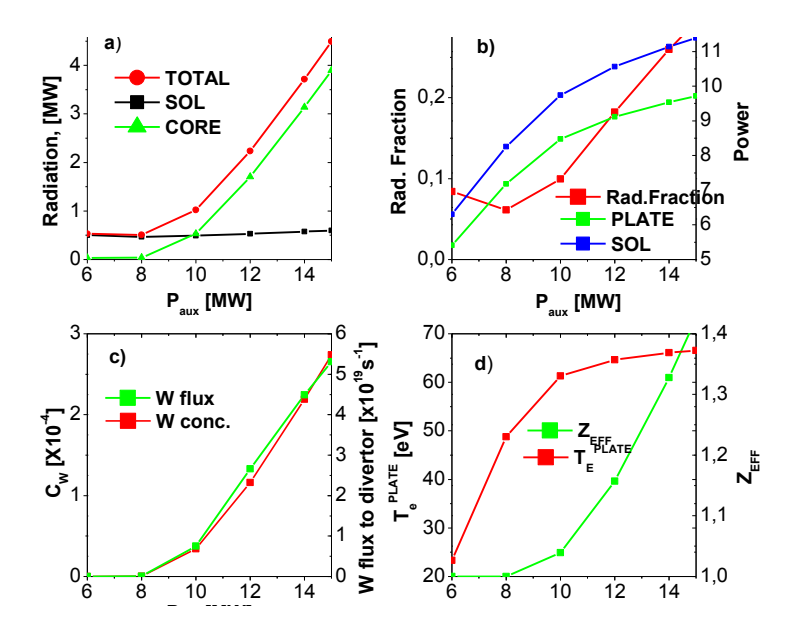


Fig. 1. a) Radiation losses: total, in SOL and in core b) radial fraction, power to plate and SOL, c) tungsten concentration and flux to divertor, d) electron temperature to plate and Z_{EFF}

Not surprisingly, the separatrix density n_{sep} is the most critical parameter, since it has a large effect on the temperature drop in the SOL (as illustrated on Fig. 1). All other parameter being kept constant, decreasing n_{sep} from 3x 10¹⁹ to 2x 10¹⁹ m⁻³ roughly doubles the W concentration in the core ($C_W = 2.4 \times 10^{-4}$) with respect to our reference case (see Fig. 1 c) for $P_{aux} = 12$ MW), and hence the radiation losses ($P^{core} = 3.6$ MW). If now n_{sep} is increased to 3.5x 10¹⁹ m⁻³, C_W comes down to 2.7 x10⁻⁵ and the core radiation losses ($P^{core} \cong 0.4$ MW) become somewhat smaller than deuterium radiation losses in the SOL. Finally, it should be noted that the average density considered here is such that $< n_e > = 0.4 n_{GW}$, so that the value for the separatrix density used for most of the simulations presented here ($n^{sep}_{e} = 2 \times 10^{19}$ m⁻³) may be regarded as rather conservative.

Role of light impurities

We now consider the role of low Z impurities, the case of boron, since the ICRH antennae protections will be boron coated in WEST. In fact, experiments carried out on AUG have shown that using W coated protections can lead to unacceptably high W production. These W sources are though to be related to parallel electric fields that develop in the SOL during ICRH operation, and thus depend on the antenna design [11, 12]. In our simulations, the boron influx Γ_B is taken as proportional to the plasma out-flux to the first wall Γ_{fw} , such that $\Gamma_B = Y^{eff}_B \Gamma_{fw}$, where Y^{eff}_B is an effective sputtering yield.

The boron concentration C_B (expressed in percent) is then an output of the simulation. Scan in boron concentration are made in practice by varying Y^{eff}_B from 0.1 to 10, which typically correspond to concentrations from 0.03 to 4% (and values of Z_{eff} up to 3 in the worse case(Fig.2c)). It should be noted that the latter is a fairly high value, above value expected in WEST. In the all W AUG, light impurity concentrations given in Ref. [12] are 2% for C and 0.2% for O before a boronisation, and 0.7% for C, 0.04% for O and 0.7% for B long after the boronisation. We consider here as a basis for the discussion the case at $P_{aux} = 12$ MW, the other parameters being the same as in the previous section. As the

concentration of Boron increases, the sputtered W flux increases (Fig. 2 b)), but remains dominated by self-sputtering for boron concentrations lower than 1 %.

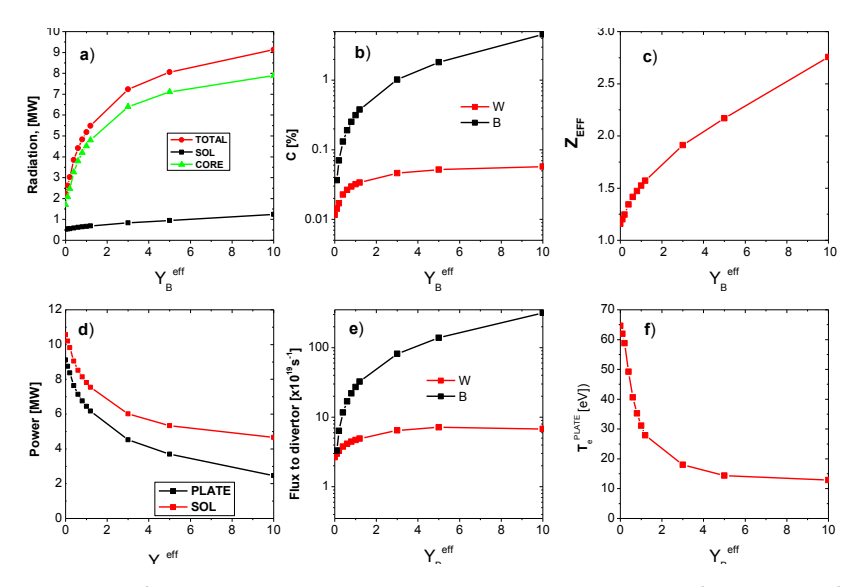


Fig. 2. In case with boron:a) Radiation losses: total, in SOL and in core, b) tungsten (W) and boron (B) concentration, c) Z_{EFF},d) power to plate and to SOL, e)tungsten and boron flux to divertor, f) electron temperature to plate

However, the initial production of W is clearly dominated by boron sputtering, which is stronger than deuterium sputtering even at the lowest concentration considered here. The W concentration in the core C_W increases by a factor of 5 for the highest concentration, from an already significant level of the order of ~10⁻² % in the case where there is no boron, while the total sputtered fluxes rises by a factor of 2 only. This signals a degradation of the SOL screening efficiency, related to the fact that the parallel gradients in the SOL increase when lowering the power influx to the SOL (at constant $n^{sep}_{e} = 3 \times 10^{19} \text{ m}^{-3}$), thus increasing the thermal force. The effect of boron on the power flowing to the plate is strong (black squares on Fig. 2 d), since W radiation losses are large for the range of concentration considered here. To first order, the decrease of the power to the plates is thus explained by a decrease in the power influx to the SOL. The power losses in the SOL from boron become comparable to the hydrogen radiation losses for concentration of the order of 0.5 %, but this remains a fairly modest contribution except for the highest concentrations.

Conclusions

The COREDIV model has been applied to study core-edge coupling mediated by tungsten for WEST. For all configurations, an acceptable level of tungsten is found with low radiation levels. Simultaneously, tolerable heat loads to the plate are observed, at ITER relevant levels. The power to the plate saturates when heating increases (for a given density). Changes to average or separatrix density can strongly influence the results. Self-sputtering appears to be the dominant mechanism for tungsten production. This effect of core-edge coupling increases strongly with light impurities (here boron), because the sputtering threshold for boron on tungsten is much lower than for deuterium. T

Collaboration

Association EURATOM – CEA
Aix-Marseille Universit'e, CNRS, PIIM, UMR 7345, F-13397 Marseille Cedex 20, France,
Yannick Maranded

References

- [1] A. Grosman et al., Fusion Engineering and Design, http://dx.doi.org/10.1016/j.fusengdes.2013.
 02.039.
- [2] R. Zagórski et al., Contrib. Plasma Phys. 48, 179 (2008)
- [3] J. Mandrekas and W. M., Stacey Nucl. Fusion 35, 843 (1995).
- [4] ITER Physics Expert Groups on Confinement and Transport and Confinement Modelling and Database, ITER Physics, Basis Editors and ITER EDA, Nucl. Fusion 39 2175 (1999).
- [5] R. Neu et al., Nucl. Fusion 45, 209 (2005).
- [6] M. Leigheb et al., J. Nucl. Mater. 241-243, 914 (1997).
- [7] R. Zagórski et al., J. Nucl. Mater. 390-391, 404 (2009).
- [8] R. Zagórski et al., Contrib. Plasma Phys. 52(5-6), 379 (2012).
- [9] A. Kallenbach et al., Plasma Phys. Control. Fusion 47 B207 (2005).
- [10] M. Shimada et al., IAEA- CN-77/ITERP/05.
- [11] V. Bobkov et al., Nucl. Fusion 50, 035004 (2010).
- [12] V. Bobkov et al., Proc. of the 24th IAEA Fusion Energy Conference, San Diego, USA, EX/P5-19.

Numerical analyses of impurity seeded JET plasma discharges with the help of the code COREDIV

Principal investigator:

I. Ivanova-Stanik; <u>irena.ivanova-stanik@ipplm.pl</u>

Collaborators from the Institute of Plasma Physics and Laser Microfusion:

R. Zagórski, R. Stankiewicz, A. Czarnecka

Introduction

Impurities released from interactions between plasma and material surfaces can lead to major effects on plasma behaviour in tokamaks. This is in particular true for JET experiments with the new ITER-like wall (ILW) configuration (ILW: Beryllium wall + W (metallic divertor)), which shows that the plasma performance is strongly affected by tungsten impurity [1]. In view of possible realistic prediction for ITER plasma scenarios, it is necessary to developed validated numerical tools. For this aim, COREDIV code [2] has been constructed, which self-consistently couples the plasma core with the plasma edge and the main plasma with impurities. The code was in the past successfully benchmarked against a number of JET discharges with carbon plates and impurity seeding [2–4] proving its capability of reproducing the main features of JET seeded discharges as the electron density and temperature profiles, the total radiated power, and the effective ion charge, Z_{eff} . The model has also been applied for ASDEX-U discharges in the full tungsten machine environment [5] and recently, first results for L-mode pulses of JET ILW configuration has been presented is Ref. [6].

In this report numerical simulations with COREDIV code of JET discharges with ITER-like wall for H-mode and hybrid scenarios with nitrogen seeding are presented. Since the energy balance in tokamaks with metallic walls depends strongly on the coupling between bulk and the SOL plasma, joint treatment of both regions is necessary. Therefore the physical model used in the COREDIV is based on a self-consistent coupling of the radial transport in the core to the 2D multi-fluid description of the scrape-off

layer (SOL) and has been already presented else where [2, 4, 6-8]. In the core, the 1D radial transport equations for bulk ions, for each ionization state of impurity ions and for the electron and ion temperature are solved. For auxiliary heating parabolic like deposition profile is assumed and the energy losses are determined by Bremsstrahlung, ionization and line radiation. The energy and particle transport are defined by the local transport model proposed in Ref. [9] which reproduces a prescribed energy confinement law. In the SOL, the 2D fluid equations are solved in the simplified slab geometry but taking into account plasma recycling in the divertor and sputtering processes due to all ions (D, Be, N_2 , W) at the target plate.

In this report numerical simulations with COREDIV code of JET discharges with ITER-like wall are presented. We concentrate on the JET H-mode and hybrid scenarios with nitrogen seeding and all simulations have been performed with the same transport model and only the discharge input parameters like auxiliary heating P_{aux} , line average plasma density n_{line} , confinement factor H_{98} , nitrogen input flux Γ^{puff}_{N} were changed in the calculations. The separatrix density n^{sep}_{e} is an input parameter in our model and has been kept equal to $0.4 \div 0.5 n_{line}$ in the simulations, with the recycling coefficient adjusted accordingly. It has been shown that COREDIV is able to reproduce basic parameters of nitrogen seeded discharges for both H-mode and hybrid scenarios. We have achieved reasonable agreement with global plasma parameters like radiations levels, Z_{eff} and tungsten concentrations and the plasma profiles, including density, temperature and radiation are in very good agreement with experimental data. The agreement of the code results with the experimental data might be even better, if the simulations are further tuned taking into account uncertainties to the sputtering model, separatrix density or SOL transport. Simulations show that the observed Z_{eff} level is defined mostly by the low Z impurity content, Be and N_2 in the considered shots. It has been found that the tungsten radiation plays always very important role and can not be mitigated even by strong influx of nitrogen.

Modelling results for H-mode and hybrid scenario

We note that all simulations have been performed with the same transport model and only the discharge input parameters like auxiliary heating P_{aux} , line average plasma density n_{line} , confinement factor H_{98} , nitrogen input flux Γ^{puff}_{N} were changed in the calculations. The separatrix density n^{sep}_{e} is an input parameter in our model and has been kept equal to $0.4 \div 0.5 n_{line}$ in the simulations, with the recycling coefficient adjusted accordingly. The input power has been split between electrons and ions, as 3/1.

The code was run in a steady-state mode neglecting fast phenomena like e.g. ELM's. This corresponds to the experimental results averaged over energy confinement time and seems to not impose strong limitations on the code-experiment comparison.

Results of simulations of two series of JET H-mode discharges with different level of auxiliary power are considered first and the comparison of global parameters with experimental data is shown in the Table 1 for pulses 82031 and 82033 (I_p =1.98 MA, B_T =2.18 T) with P_{aux} = 10.8 MW and pulses 83178-80 (I_p =2.47 MA, B_T =2.7 T) with P_{aux} ~ 17 MW. In the this same table is present, also results for bybrid scenario (shots 83568, 83570; I_p =1.68 MA, B_T =1.975 T), where P^{core}_{rad} is the core radiation (mostly by tungsten), P^{tot}_{rad} is the total radiation, n_{line} is line average plasma density (experimentally measurement by HRTS diagnostic) and c_W is the volume averaged tungsten concentration.

Table 1. The experimental and simulated global plasma parameters for shots 83178-80

JET	P _{aux}	t _E	Z _{EFF}	P ^{CORE} rad	P ^{TOTAL} rad	Γ ^{puff} _N	n _e lin	C _w
Shot	[MW]	[s]		[MW]	[MW]	[x10 ²¹ el/s]	[x10 ¹⁹ m ⁻³]	x10 ⁻⁵
H – mode								
82031(exp)	10.8	0.31	1.36	3.1	5.4	1.1	6.34	1-2
COREDIV	11	0.3	1.26	2.3	5.51	1.05	6.8	1.36

82033(exp)	10.8	0.34	1.26	2.1	5.0	1.6	7.1	1-2
COREDIV	11	0.3	1.26	2.46	5.88	1.05	7.34	1.16
83178 (exp)	16.7	0.32	1.46	3.54	6.31	3.03	7.23	~3.5
COREDIV	17	0.29	1.41	3.78	8.7	1.05	8.17	1.52
83179 (exp)	16.7	0.34	1.36	4.13	7.8	1.54	7.9	-
COREDIV	17	0.29	1.18	4.66	7.88	0.35	8.26	2,2
83180 (exp)	17	0.32	1.33	4.38	6.8	0.78	7.8	~2.1
COREDIV	17	0.32	1.12	3.14	6.71	0.35	8.26	1.38
				Hybryd sce	narios			
83568 (exp)	25.7	0.16	2.51	~5	17	6.2	6.77	-
COREDIV	24	0.17	2.5	11	17.5	2.8	6.79	9.01
83570 (exp)	20.5	0.17	3.07	5.1	15.7	4.9	6.46	-
COREDIV	20.5	0.15	2.94	7.6	14.7	3.3	6.86	6.65

The beryllium flux from the wall has been assumed to be equal to Γ_{Be} = 2 $x10^{20}$ part./s for the low power shots and to be proportional to the particle flux crossing the separatrix with the proportionality coefficient equal to 0.8 for all other shots in order to reproduce the low Z impurity level. For the low power shots (Table 1) the comparison with the experimental data is very good whereas for high power H-mode discharges there is some discrepancy when comparing all radiations and the Z_{eff} values. We note also that the experimental values of the nitrogen influx (Γ^{puff}_N) are usually larger than in simulations since in latter case all the gas goes to the plasma which is not necessarily true for experimental situation (a significant part of the gas might be lost to the wall not reaching the plasma). The simulated Z_{eff} is lower than the experimental value for two pulses 83179-83180, but simultaneously the total radiation is correct in contrast to the shot 83178, when Z_{eff} is correct but the total radiation is higher in the experiment, however the radiation in the core is similar to the experimental one.

For hybrid scenarios, measured values of $Z_{\it eff}$ and total radiated power are very well reproduced by simulations, but there is some difference between simulations and experiment regarding power radiated in the core as it can be seen from Table 3. We note, that W concentration for hybrid scenarios is much higher than for H-mode shots mostly due to the lower plasma density and stronger heating. That means that in spite of very strong seeding, the tungsten radiation remains important energy loss channel.

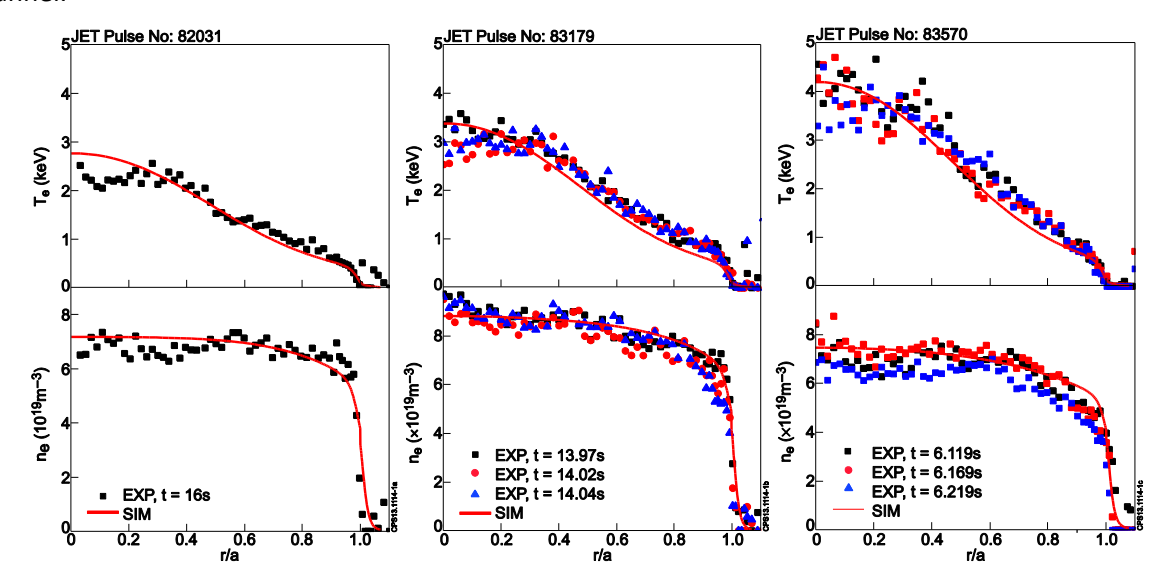


Fig. 1. Electron temperature (top) and density (bottom) profiles from HRTS diagnostic at different time and from COREDIV simulations, as function of the normalized minor radius for 82031(left), shot 83179(middle) and shot 83570(right).

In Fig.1, the experimental and simulated electron density and temperature profiles are shown for shots 82031,83179 (H-mode) and 83570 (hybrid scenario), respectively. It can be seen that radial profiles are nicely reproduced by the code. We note also, that in the considered shots tungsten accumulation is not observed which is consistent with our assumption, that the impurity transport is dominated by anomalous contribution. This assumption is also consistent with the radiation distribution as it can be seen from Fig.2, where experimental and simulated radiation profiles in the plasma core are shown for H-mode shots (82031, 83179) and hybrid scenario (83570), respectively. The calculated radiation profiles agree relatively well with the experimental data showing strong contribution of tungsten to the radiation losses. Radiation losses due to nitrogen are important only very close to the separatrix.

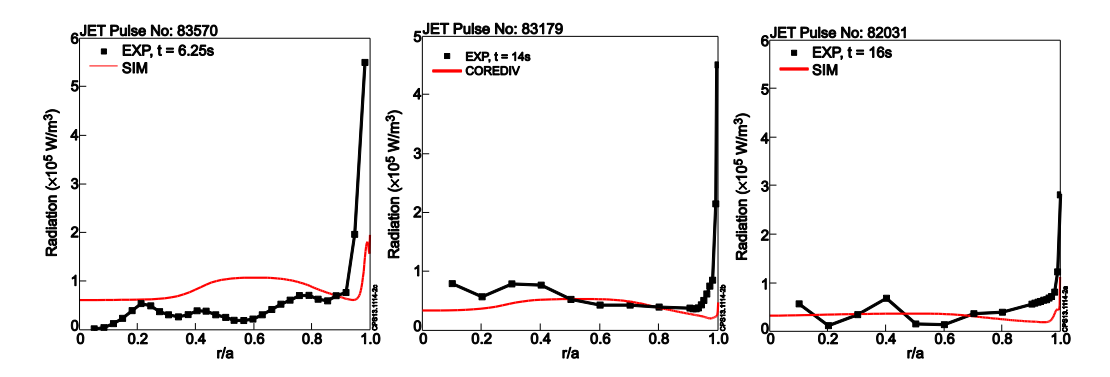


Fig. 2. Profile of the radiation at t = 56s for shot 82031(left), at t = 54s for shot 83179 (middle) and at t = 46.25s for shot 83570 (right).

It is important to note that in all considered shots tungsten radiation in the core is the dominant energy loss mechanism, which is good correlation with JET experimental results showing that the JET plasma performance is strongly affected by tungsten impurity [1]. This is even true for strongly seeded hybrid shot $83570(\Gamma^{puff}_{N} \sim 5x10^{22}el/s)$ for which 37% of the radiated power is still due to W. For this particular case, COREDIV simulations indicate semi-detached conditions in the divertor, with the plate temperature $T^{plate}_{e} \approx 2eV$ but still with significant tungsten production by N ($\Gamma_{W} = 6.64x10^{19} \text{ 1/s}$).

Sensitivity analysis

As already mentioned, in some cases it is difficult to fit by COREDIV simulations all the experimental global parameters like radiations and Z_{eff} simultaneously. It can be attributed to the assumptions made in the model as well as to the unknowns related to the experimental data. It is important to know for example what is the role of sputtering model used in the code and in particular the effect of prompt redeposition on the results. Certainly plasma parameters in the SOL, like separatrix density, deuterium puff or radial transport have influence on tungsten retention and in consequence on core parameters. In order to understand the reason for the differences between experimental and computation results, we have performed numerical studies to see which parameters have strong influence on the plasma parameters, in particular on the radiation level and its distribution.

Influence of the sputtering coefficient

It is believed that in case of tungsten, the prompt redeposition might strongly reduce effective sputtering yield. Therefore, simulations have been performed to check sensitivity of the results on the total sputtering yield. For this aim, the sputtering yield due to all ions was reduced by factor: 0.3, 0.24,0.18 and 0.06 in comparison to the standard model (first row in the table) and the results are presented in Table 2. It can be seen, that the reduction of the sputtering coefficient leads as expected to the smaller tungsten production and in consequence to the reduction of the core and total radiation. However, the effect is rather moderate, since the change of the sputtering yield by factor ~17, reduces W concentration 4 times, core radiation by factor 3 and total radiation only by 1.5. The reason is such

that the reduction of the sputtering yield is compensated by the increase of the plate temperature due to self-regulating mechanism coupling efficiently W production in the SOL with tungsten radiation in the core. In addition, sputtering yield has almost no influence on the effective charge and SOL radiation.

Table 2 The caption inside a table environment

Sput. Coeff.	C _W x10 ⁻⁵	Z _{EFF}	T _e ^{plate} [eV]	P ^{TOTAL} rad [MW]	P ^{CORE} rad [MW]
1	1.96	1.14	5.62	5.63	2.92
0.3	1.72	1.13	5.95	5.3	2.62
0.24	1.49	1.11	6.13	5	2.33
0.18	1.22	1.11	6.27	4.64	1.98
0.06	0.5	1.11	7.25	3.66	1.05

<u>Influence of the Nitrogen puff level and the separatrix density</u>

In the Fig. 3 we present scan with nitrogen gas puff for hybrid scenario with input parameters fixed for the shot 83570 and with three different density values at the separatrix. The initial increase of the N_2 influx (Γ^{puff}_{N} <1x10²¹ 1/s) leads to strong increase of the tungsten concentration and consequently core radiation as a result of increased tungsten production. However, for higher fluxes (Γ^{puff}_{N} >1x10²¹ 1/s) the changes to the core parameters are rather weak. This is the result of a self-regulating mechanism being a specific feature of tungsten (metallic) targets. This mechanism regulates the tungsten production due to sputtering processes at the target plates by radiative cooling of tungsten ions in plasma centre. Since the radiation efficiency of tungsten is very high and simultaneously the dependence of the sputtering yield on the temperature (incident ion energy) is very steep the equilibrium between production and radiation appears at temperature values very close to the sputtering threshold (in this case for nitrogen). The SOL radiation increase linearly with gas puffing reducing effectively power to the targets. For the highest seeding levels, semi-detached conditions are achieved in divertor with (T_e^{plate} <3eV).

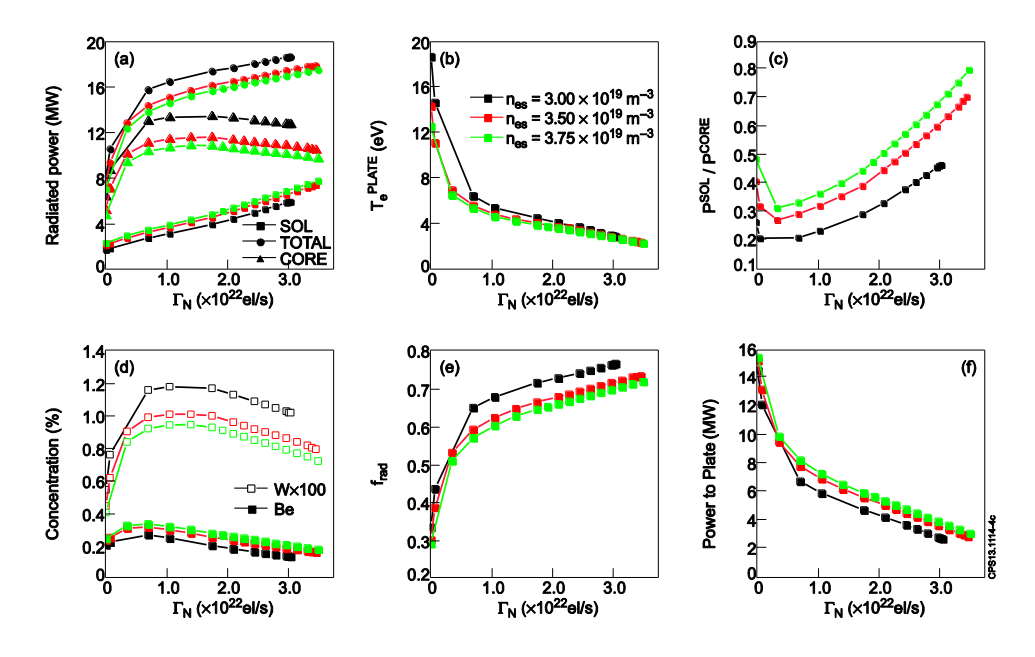


Fig. 4. Hybrid regime: plasma parameters versus nitrogen gas puf for three different electron density on the separatrix electron density is n^{sep}_{e} = 3.0 x10¹⁹ m^{-3} (black line), n^{sep}_{e} = 3.5 x10¹⁹ m^{-3} (red line) n^{sep}_{e} = 3.75 x10¹⁹ m^{-3} (green line): total (circle simbols), core (square simbol) and SOL (triangle) radiation (a), electron temperature at the plate (b), radiation SOL/CORE (c), W and Be concentration (d), radial fraction (e), power to plate (f).

The separatrix density being the code input parameter appears to be a very important quantity controlling the SOL plasma properties. In the self-consistent simulations its effect is however limited mostly to the changes in the screening efficiency of the SOL, which leads to the better confinement of W ions in the edge and consequently to lower radiation losses in the core.

Conclusions

The COREDIV code has been used to simulate JET discharges in the new ITER-like wall configuration. The focus has been put on auxiliary heated H-mode and hybrid scenarios with nitrogen seeding. The work was motivated by the need to develop validated numerical tool which can be used for fast analysis of the experimental data and for prediction of future experiments, in particular with extensive level of auxiliary power and seeding. It has been shown that COREDIV is able to reproduce basic parameters of nitrogen seeded discharges for both H-mode and hybrid scenarios. We have achieved reasonable agreement with global plasma parameters like radiations levels, Z_{eff} and tungsten concentrations and the plasma profiles, including density, temperature and radiation are in very good agreement with experimental data. The agreement of the code results with the experimental data might be even better, if the simulations are further tuned taking into account uncertainties to the sputtering model, separatrix density or SOL transport. Simulations show that the observed Z_{eff} level is defined mostly by the low Z impurity content, Be and N_2 in the considered shots. It has been found that the tungsten radiation plays always very important role and can not be mitigated even by strong influx of nitrogen.

Collaboration

Association EURATOM/CCFE Fusion Association, Culham, Abingdon, Oxon. OX14 3DB, UK Department of Applied Physics, Ghent University, B-9000 Gent, Belgium

References

- [1] Yu. F. Baranov, C. D. Challis, J. Hobirk, et al., 40th EPS conference on Plasma Physics, Espoo, Finland, pp.P5.142(2013)
- [2] R. Zagórski et al., Contrib. Plasma Phys. 48(1-3), 179 (2008)
- [3] J. Rapp, et al., J. Nuclear Materials, 337-339, 826 (2005)
- [4] R. Zagórski, et al. J. Nuclear. Mater. 390-391,404 (2009)
- [5] R. Zagórski, et al. Contrib. Plasma Phys. 52(5-6), 379 (2012)
- [6] G. Telesca, R. Zagórski, et al., Journal of Nuclear Materials 438, S567 (2013)
- [7] G. Telesca, R. Zagórski, et al., Plasma Phys. Control. Fusion (53), 115002 (2011).
- [8] G. Telesca, I. Ivanova-Stanik, PET14, Cracow, (2013)
- [9] J. Mandrekas and W.M. Stacey, Nucl. Fusion 35 (1995) 843

Maintenance, continuing development, verification and validation of the ETS and other core components

Principal investigator:

R. Stankiewicz; <u>roman.stankiewicz@ipplm.pl</u>

Collaborator from the Institute of Plasma Physics and Laser Microfusion:

I. Ivanova-Stanik

Introduction

The ultimate goal of ITM project is the development of the system of codes represented all important physical problems of modelling of plasma in tokamak. The system of codes is written as moduli which can be transform to actors on the Kepler platform. Predefined structures of data CPO (Consistent physical object) is used in communication between moduli (actors). The Kepler workflow can be prepared using User Graphical Interface. Main part of ITM structures is ETS solving the transport equation for the ion and electron densities and temperatures, the current evolution and the toroidal ions rotation. The results presented in the report are devoted to validation of ETS and improving the numerical procedures used in ETS. The first part of the report describes the modelling of ITER scenario undertaken in ISM (ITER Scenario Modelling) being the part of ITM activity using the tools outside ITM structure.

The 'European Transport Simulator' (ETS) is the new modular package for 1D discharge evolution developed within the EFDA Integrated Tokamak Modelling (ITM) Task Force. It consists of precompiled physics modules combined into a workflow through standardized input/output data structures. Ultimately, the ETS will allow for an entire discharge simulation from the start up until the current termination phase, including controllers and sub-systems. In the report the following topics are presented:1) Integrated modelling of ITER scenario based on the existing scenario developed with CRONOS, JETTO and ASTRA 2) Impurity modelling for JET (Be and W) with help of ETS. Comparison of simulated radiation profile with experiments. 3) work on stabilization of ETS numerical scheme for stiff transport problem.

Integrated modelling of ITER scenario with ITM ETS workflows, based on the existing scenario developed with CRONOS, JETTO and ASTRA

Recent JET experiments show that the plasma performance is strongly affected by tungsten impurity [1]. The procedure has been developed to use core transport code and take into account the coupling between core and scrape off layer and sputtering of tungsten at target plates with help of COREDIV code. Here the influence of impurities on the performance of ITER H-mode plasmas (I_{pl} = 15 MA, B_{tor} = 5.3 T, P_{NB} =33MW and P_{FCBH} =20 MW) is assessed via integrated core-SOL-divertor modeling performed with JETTO [2] and COREDIV [3] codes used iteratively. JETTO code provides the magnetic equilibrium, the current diffusion, the auxiliary heating and current drive and transport simulations for main ion species inside the sepatarix while the COREDIV code completes these simulations with impurity distribution and radiation, taking into account the core-SOL-divertor coupling. Such an approach allows one to combine a high level of complexity of core transport modelling with the impurity, SOL and divertor simulations needed for the self-consistent estimation of the core plasma performance, heat and particle fluxes to divertor and sputtering at divertor plates. The simulations are performed for medium $(n^{ped}_{e} = 6.12 \times 10^{19} \text{m}^{-3})$ and high $(n^{ped}_{e} = 9.0 \times 10^{19} \text{m}^{-3})$ pedestal density with a goal to compare the fusion performance in these two cases. Electron and ion temperatures and main ion density within the separatrix are simulated with the JETTO code using the GLF23 transport model [4], continuous ELM transport models, PENCIL module for NBI simulations and Gaussian ECCD profile located at ρ =0.4(ρ is the square root of normalised toroidal flux). Current diffusion is estimated using the NCLASS module [5] for resistivity and bootstrap current. Neoclassical thermal and main species transport is also computed with NCLASS. The pedestal temperatures in each case are estimated using the EPED model for pedestal width ($\Delta \rho = 0.07$) and defined pressure at pedestal [6]. The parameters (H_{98y} factor, volume averaged density and auxiliary heating of electron and ions and pedestal location) obtained in JETTO simulations are used as an input for COREDIV where the transport coefficients, gas puff and deutirium recycling coefficient are adjusted to match the temperatures and main ion density profiles obtained with JETTO (including separatrix density). Intrinsic Be and W impurities, Ne seeding (when applied) as well as helium ash are simulated with COREDIV assuming the same transport coefficients for all impurities and main ion species ($D_{imp} = D_D = 0.35 \mathcal{X}_e$; $V_{imp} = V_D$, where \mathcal{X}_e is electron heat conductivity). Electron conductivity in COREDIV is defined using the energy confinement scaling law. When a good match of n_e , T_e and T_i is achieved the impurity and radiation profiles are passed back to JETTO for simulations of main plasma species with GLF23 models. This procedure is repeated until the consistent solution is obtained. The usage of two codes is schematically illustrated on Fig. 1.

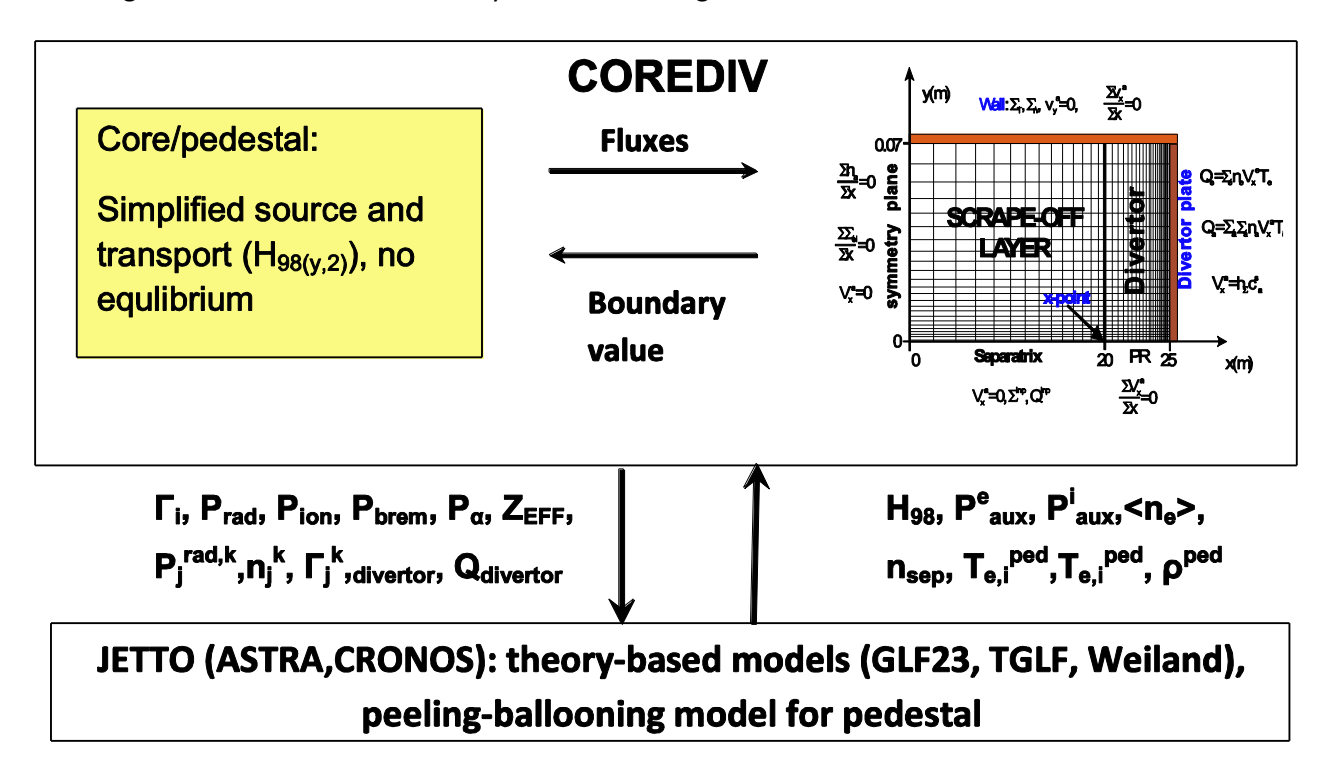


Fig. 1. Illustration of JETTO-COREDIV iterations. Using this approach the JETTO code can be replaced with any advanced core transport code (ASTRA, CRONOS).

The ion and electron temperatures and the electron density obtained in JETTO and COREDIV simulations for medium and high density cases are shown on Fig. 2. While the density profiles are similar in two codes it is difficult to match precisely the GLF23-computed temperature profiles with the parabolic H_{98y} -based transport coefficients. Nevertheless, a relatively good agreement between T_e and T_i computed with two codes is obtained at medium density, with 15% difference in alpha heating power ($P^{IETTO} = 93.6MW$; $P^{COREDIV} = 79MW$). The W concentration is $5.16 \times 10^{-3}\%$? In this plasma, and core and edge radiation are 42 MWand 8.4 MW, correspondingly.

With such core radiation the power through separatrix (P_{loss}) exceeds the L-H power threshold (P^{LH}) estimated with Martin scaling [7] by nearly 30%. However, the power to divertor is too high (70 MW) to be sustained by target plates. Provided that the divertor area is about $4m^2$ such power (even if it is distributed uniformly) strongly exceeds the divertor heat load limit $10MW=m^2$. The H-mode regime with high pedestal pressure is obtained in COREDIV by increasing the Duterium gas puff (from 9.1×10^{21} to $21.1\times10^{21}1/s$) while the transport coefficients remain roughly the same. The volume averaged

density rises by 30% while the core temperatures reduce (Fig. 2). The difference in core ion temperature computed with GLF23 and scaling-based transport models (Fig. 2, right column) results in a different alpha-heating. In COREDIV simulations 140 MW of alpha heating are obtained that leads to a higher power to divertor (85.3 MW), divertor temperature and W sputtering as compared to medium density case.

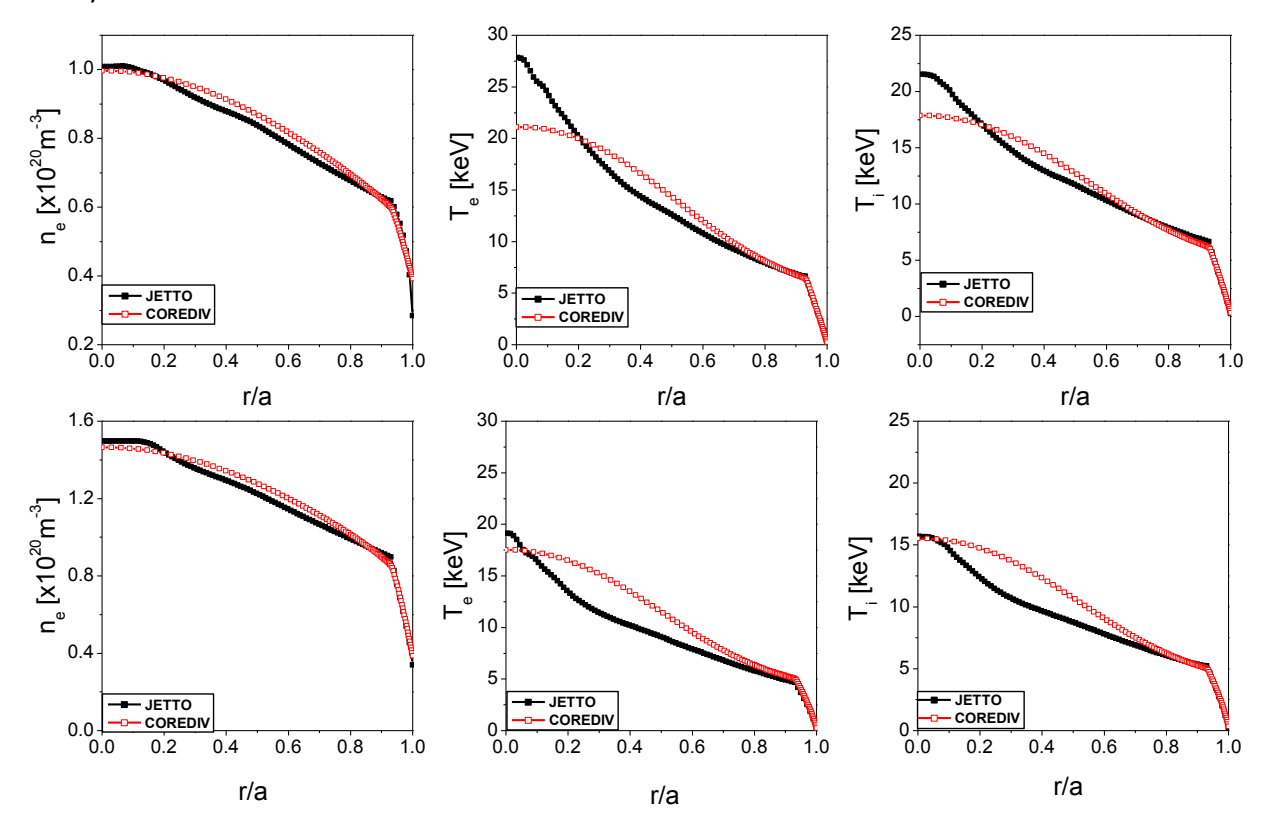


Fig. 2. Electron density (left column), electron temperature (middle column) and ion temperature (right column) obtained in JETTO simulations using the GLF23 transport model for medium (top) and high (bottom) density ITER H-mode (black symbols). The best match of these profiles with COREDIV using H_{98y} -based scaling model is show by red symbols.

Impurity modelling for JET (Be and W) with help of ETS. Comparison of simulated radiation profile with experiments.

The impurity module in the ETS workflow enables the simulation of the time evolution of the impurity density for an arbitrary number of impurities for all ionization states. Density sources for each ionization state include ionization, recombination and charge-exchange, where rate coefficients of the relevant process are obtained from the ADASdatabase using generic interfaces developed by the ITM-TF. Boundary conditions for individual impurity ionization states were given by the total impurity concentration at thelast closed magnetic surface, assuming a coronal distribution at the corresponding ion temperature.

The ETS was applied to simulate impurity transport for the conditions of JET discharge #82794 (ITER like wall), where is observed accumulation on the tungsten (Fig.3). We use the ETS workflow for simulate to radiation profile and comparison with experimental results (bolometric signal).

Prescribed profile of the electron density are prescribedfor bulk ions Bohm-Gyro-Bohm diffusion plus diffusion coefficient and pinch velocity for impurity are used the density for impurities at separatrix (tungsten (W), nikel (Ni) and beryllium (Be) and transport coefficient (diffusion and convection) are changed in order to reproduce radiation and Z_{eff} profiles

Accumulation phase ## Accumulation phase

Experimental data for ILW JET shot #82794

Fig. 3. Experimental data, radiation, Z_{EFF} , auxiliary heating, nickel density at shot 82794.

In the Table 1, the runs with different diffusion and convection for impurity., where W^{sep} , Be^{sep} , Ni^{sep} is tungsten, beryllium and nickel density on the separatix, respectively, D_{imp} is diffusion coefficient the same for all impurity and all different ionization state. V^W , V^{Be} and V^{Ni} is pinch velocity for tungsten, beryllium and nickel and P_{rad} is total radiation are presented.

We observe, that radiation and Z_{EFF} in centrum is dominated by tungsten. The beryllium and nickel have influence in the region closed to pedestal and separatrix. In the Fig. 4 we present theradiation and Zeff profiles for different runs: only tungsten, tungsten and beryllium, tungsten, beryllium and nickel. comparison the experimental and simulated profile.

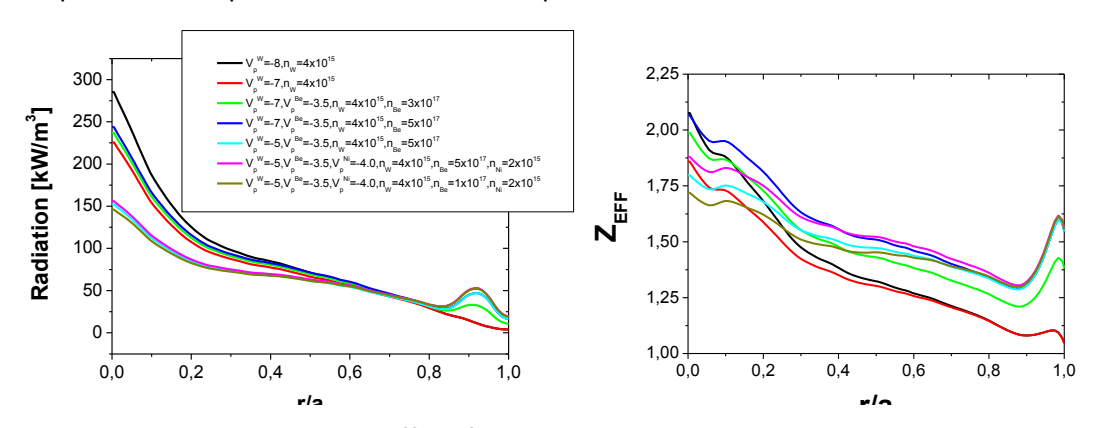


Fig.4. Simulated radiation and Zeff profiles.

Table 1. Input parameters used in simulation

shot	run	D _{imp}	P _{rad}	V ^W	W ^{sep}	V ^{Be}	Be ^{sep}	V ^{Ni}	Ni ^{sep}
		$[m/s^2]$	[MW]	[m/s]	[m ⁻³]	[m/s]	[m ⁻³]	[m/s]	[m ⁻³]
82794	18	2.5+2xBgB	4.13	-8	4 x10 ¹⁵	0	0	0	0
82794	19	2.5+2xBgB	3.81	-7	4 x10 ¹⁵	0	0	0	0
82794	20	2.5+2xBgB	4.52	-7	4 x10 ¹⁵	-3.5	3 x10 ¹⁷	0	0
82794	21	2.5+2xBgB	5	-7	4 x10 ¹⁵	-3.5	5 x10 ¹⁷	0	0
82794	22	2.5+2xBgB	4.398	-5	4 x10 ¹⁵	-3.5	5 x10 ¹⁷	0	0
82794	23	2.5+2xBgB	4.625	-5	4 x10 ¹⁵	-3.5	5 x10 ¹⁷	-4	2 x10 ¹⁵
82794	25	2.5+2xBgB	4.52	-5	4 x10 ¹⁵	-0.5	1 x10 ¹⁷	-4	2 x10 ¹⁵

In the Fig. 5 we present comparison of the experimental and simulated profiles: only for tungsten, tungsten and beryllium, tungsten, beryllium and nickel, comparison the experimental and simulated profile.

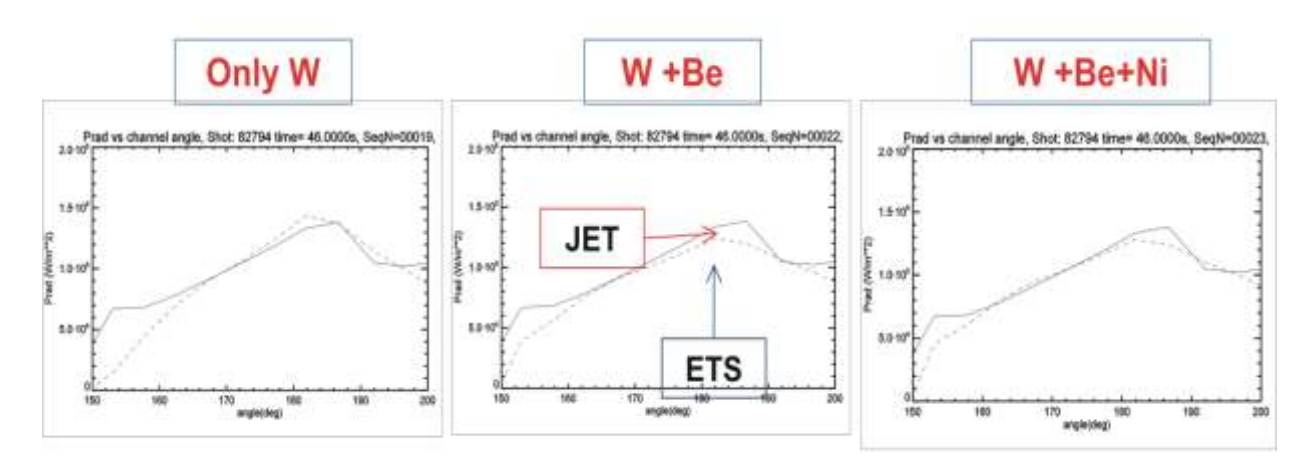


Fig. 5. Experimental and simulated profile on the radiation at #shot 82794, t=46s. It can be observed that taking into account all impurities the relatively good agreement can be achieved.

Works on stabilisation of numerical solver in ETS for stiff transport problem.

The anomalous transport based on first principle (e.g. GLF23 model) leads to diffusion coefficient depending strongly on gradient of the solution. In numerical integration of transport equation the standard procedure are stable only for very small time step unacceptable for practical use. The smaller time steps leads usually to oscillation both in space and time. The usual procedures used in this case are: 1) Newton iteration, 2) introduction of large extra diffusion term compensated by modification the vpinch velocity and (or) source term, 3) smoothing the solution and transport coefficient in every time step. The subroutine for testing the first two method has been developed which can be used as actor in Kepler workflow. The method can be described by the following equation:

$$\frac{aY^{n} - bY^{old}}{\Delta t} + \frac{\partial}{\partial \rho} \left[-(D^{I} + \overline{D}) \frac{\partial Y^{n}}{\partial \rho} + (E^{I} + \overline{E})Y^{N} \right] = S + \overline{S}$$

Index **N** stand for new solution index I values calculated from the solution from previous iteration. The extra source is defined by the formula The extra term denoted by are introduced to stabilize the numerical procedure used to solve the equation.

$$\overline{S} = \frac{\partial}{\partial \rho} \left[-\overline{D} \frac{\partial Y^I}{\partial \rho} + \overline{E} Y^I \right].$$

When the iteration converges the error introduced to the equation tends to zero. By choosing the term introduced to the equation the various iteration procedures can be defined. For example

$$\overline{E} = \overline{D} \, \frac{\partial Y^I / \partial \rho}{Y^I} \ \ \text{leads to} \ \ \overline{S} = 0 \ \ \text{and the Newton iteration is defined by choosing} \ \ \overline{D} = \frac{\partial D^I}{\partial Y^I / \partial \rho} \, \frac{\partial Y^I}{\partial \rho} \, .$$

The following steps necessary to modify the ETS Kepler workflow has been done. Modification in workflow necessary to have access to derivative of the solution in all places in workflow. Modification of files :allocate_deallocate.f90, convert.f90 fc2k_hyperdiff.f90 main_plasma.f90. type_plasma.f90. Preparation of fortran subroutine to perform the modification of transport equation described obove (Actor in kepler workflow).

Preparation of fortran subroutine to check stability of the scheme (Actor in Kepler workflows).

Conclusions

The core-pedestal-SOL modelling of ITER H-mode plasmas with intrinsic and seeded (Ne) impurities has been performed for two values of pedestal densities, n^{ped}_{e} = 6.12x10¹⁹m⁻³ (reference case) and 9.0x10¹⁹m⁻³ (artificially increased pedestal). JETTO and COREDIV transport codes have been used iteratively for this study, with the GLF23 computed thermal and particle transport for main species (JETTO) and similar transport coefficients for all impurities and main ions applied in COREDIV. Taking into account two essential constraints the H-mode has been found in case of medium density H-mode. No H-mode operation at high density has been found in JETTO/GLF23 simulations using the radiation power estimated with COREDIV. In stand-alone COREDIV simulations performed with more optimistic transport model the H-mode operational point has been found, but with the power to divertor exceeding the operational limit.

The results for simulation of JET discharge with help of ETS the good agreement between experimental and calculated profiles can be achieved. The Kepler workflow has been prepared for testing the ETS for stiff transport problem

Collaboration

Association EURATOM/OAW, Atominstitut, TU Wien, Vienna, Austria
Association EURATOM/CCFE Fusion Association, Culham, Abingdon, Oxon. OX14 3DB, UK
Department of Applied Physics, Ghent University, B-9000 Gent, Belgium
Association /IST, Lisboa, Portugal
EURATOM-IPP Association, Garching, Germany
ITM project team

References

- [1] Yu. F. Baranov, C. D. Challis, et al., 40th EPS Conf. on Plasma Phys., Espoo, 2013, pp.P5.142.
- [2] G. Cennacchi and A. Taroni, 1988 JET-IR(88) 03
- [3] R. Zagórski et al., Contrib. Plasma Phys. 48(1-3), 179 (2008).
- [4] R. E. Waltz, G. M. Staebler, et al, Phys. Plasmas 4, 2482 (1997).
- [5] W. A. Houlberg, K. C. Shaing at al., Phys. Plasmas 4, 3230 (1997).
- [6] P. B. Snyder et al., Nucl. Fusion 51, 103016 (2011).
- [7] Y. Martin et al., Journal of Physics: Conference Series 123, 012033 (2008).
- [8] R. Zagórski et al., Journal of Nuclear Materials.415, S483 (2011).

Ways to extend the operational window of high-Z PFCs ITER by external impurity seeding

Principal investigator:
I. Ivanova-Stanik; <u>irena.ivanova-stanik@ipplm.pl</u>
Collaborator from the Institute of Plasma Physics and Laser Microfusion:
R. Zagórski

Introduction

Recent JET experiments show that the plasma performance is strongly affected by tungsten impurity [1]. Here the influence of impurities on the performance of ITER H-mode plasmas (I_{pl} = 15 MA, B_{tor} = 5.3 T, P_{NBI} =33MW and P_{ECRH} =20 MW) is assessed via integrated core-SOL-divertor modeling performed with JETTO [2] and COREDIV [3] codes used iteratively. JETTO code provides the magnetic equilibrium, current diffusion, auxiliary heating and current drive and transport simulations for main ion species inside the sepatarix while the COREDIV code completes these simulations with impurity distribution and radiation, taking into account the core-SOL-divertor coupling. Such an approach allows one to combine a high level of complexity of core transport modelling with the impurity, SOL and divertor simulations needed for the self-consistent estimation of the core plasma performance, heat and particle fluxes to divertor and divertor sputtering. Here the simulations are performed for medium (n^{ped}_{e} = 6.12 × 10¹⁹m⁻³) and high $(n^{ped}_{e} = 9.0 \times 10^{19} \text{m}^{-3})$ pedestal density with a goal to compare the fusion performance in these two cases. The parameters obtained in JETTO simulations (H_{98} , factor, volume averaged density and auxiliary heating of electron and ions and pedestal location) are used as an input for COREDIV, where the transport coefficients (based on scaling low H_{98y} with parabolic profiles), deuterium(D) gas puff and D recycling coefficient are adjusted to match the temperatures and main ion density profiles obtained with JETTO (including separatrix density). Intrinsic Be and W impurities, Ne seeding (when applied) as well as helium ash are simulated with COREDIV assuming the same transport coefficients for all impurities and main ion species ($D_{imp} = D_D = 0.35 \chi_e$; $V_{imp} = V_D$). When a good match of n_e , T_e and T_i is achieved the impurity and radiation profiles are passed back to JETTO for simulations of main plasma species with GLF23 models. This procedure is repeated until the consistent solution is obtained.

Fusion performance of ITER H-mode plasmas in presence of intrinsic (He, Be and W) and seeded (Ne) impurities is investigated in self-consistent core-pedestal-SOL simulations for two values of pedestal density n^{ped}_{e} = $6.12 \times 10^{19} \mathrm{m}^{-3}$ (reference case) and n^{ped}_{e} = $9.0 \times 10^{19} \mathrm{m}^{-3}$ using the COREDIV and JETTO codes. The theory-based GLF23 transport model which predicts a relatively high density peaking ($n_{e0}/(n_{e})$ = $1.37 \div 1.39$) has been used for this study. For medium density case the H-mode operation with a power across the separatrix well above the L-H power threshold has been obtained, but the divertor heat loads exceed $10 \mathrm{MW/m^2}$. Neon gas puff strongly reduces the power to divertor plate in this scenario, increasing at the same time the tungsten sputtering by Ne that leads to even larger core radiation and dilution, than in the case without Ne. As a result, the medium density H-mode operation with Ne seeding and low divertor heat loads is barely above the L-H power threshold. This operational point is weakly sensitive to tungsten inward pinch due to a strong coupling between W transport, radiation and sputtering. At high density with much larger core radiation (90 MW), the possibility of H-mode operation strongly depends on the choice transport model, with the power through the separatrix well below the L-H power threshold in simulations with the GLF23 and above for (H98y scaling-based) transport model.

Modelling results

Ion and electron temperature and electron density obtained in JETTO and COREDIV simulations for medium and high density cases are shown on Fig. 1. While the density profiles are similar in two codes

it is difficult to match precisely the GLF23-computed temperature profiles with the parabolic H_{98y} -based transport coefficients. Nevertheless, a relatively good agreement between T_e and T_i computed with two codes is obtained at medium density, with 15% difference in alpha heating power (P^{IETTO} = 93.6MW; $P^{COREDIV}$ = 79MW). The W concentration is 5:16 × 10⁻³ % in this plasma, and core and edge radiation are 42 and 8.4 MW, correspondingly.

With such core radiation the power through separatrix (P_{loss}) exceeds the L-H power threshold (P_{LH}) estimated with Martin scaling by nearly 30%. However, the power to divertor is sufficiently high (70 MW). Provided that the divertor area is about $4m^2$ such power (even if it is distributed uniformly) strongly exceeds the divertor heat load limit $10MW/m^2$. The H-mode regime with high pedestal pressure is obtained in COREDIV by increasing the deuterium gas puff (from $9:1\times10^{21}1/s$ to $21:1\times10^{21}1/s$). The core ion temperature computed with GLF23 and scaling-based transport models (Fig. 1, right column) are roughly the same but the alpha-heating powers differ significantly. In COREDIV simulations 140 MW of alpha heating are obtained that leads to a higher power to divertor (85.3 MW), higher temperature and W sputtering as compared to medium density case.

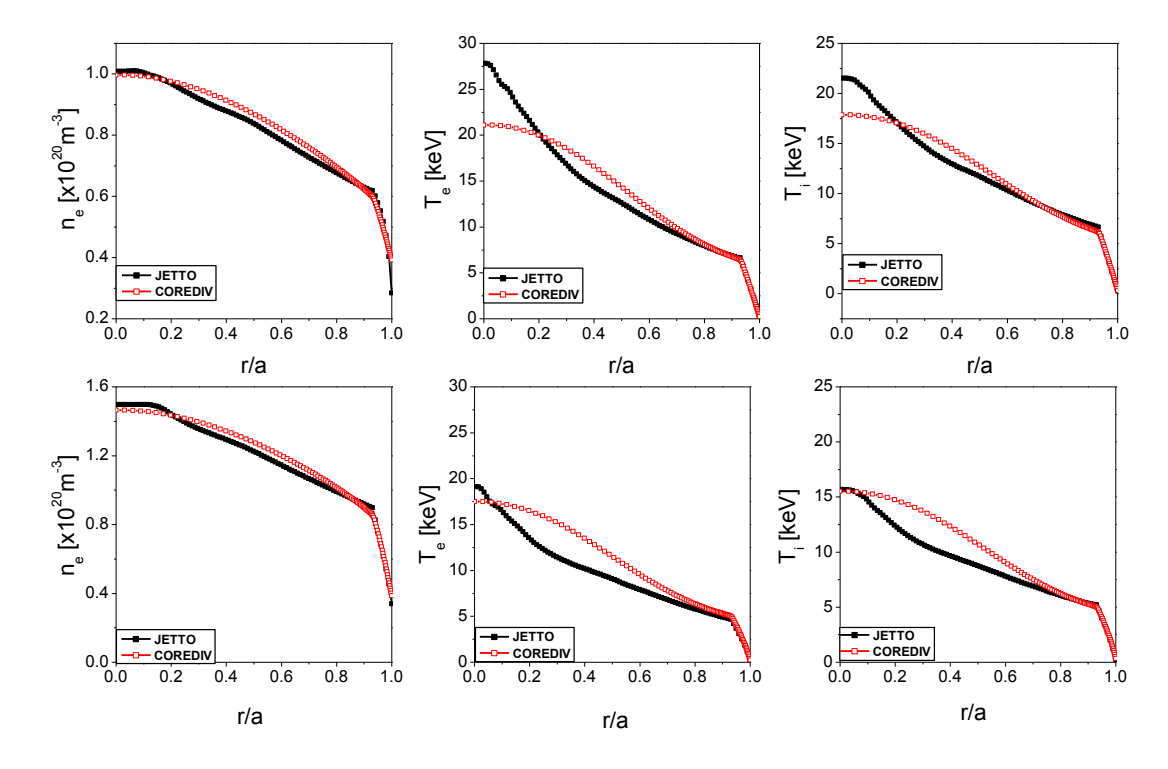


Fig. 1. Electron density (left column), electron temperature (middle column) and ion temperature (right column) obtained in JETTO simulations using the GLF23 transport model for medium (top) and high (bottom) density ITER H-mode (black symbols). The best match of these profiles with COREDIV using H_{98y} -based scaling model is shown by red symbols.

As a result, larger W concentration (6.16x10⁻³ %) and core radiation (90 MW) are obtained (Fig. 2). Such a high radiation losses are partly counteracted by increased alpha heating maintaining the plasma well above the L-H power threshold P_{LH} = 76.8 MW. However, in simulations with the GLF23 model a lower ion temperature and alpha heating (93 MW) are obtained and the power through separatrix is below the L-H power threshold. These simulations show that the high density H-mode performance is very sensitive to the choice of transport model.

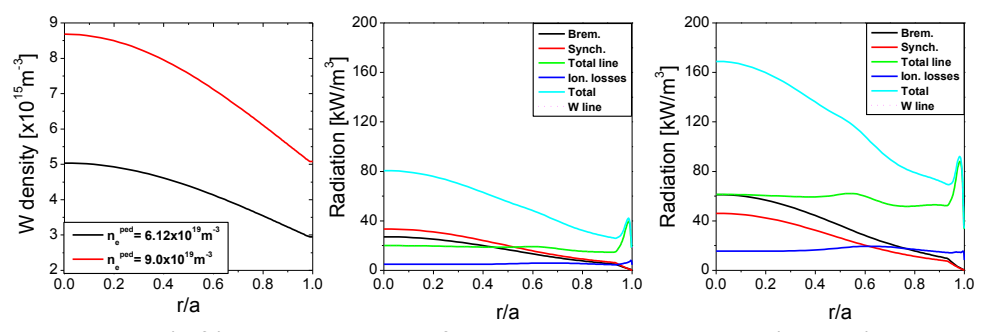


Fig. 2. Tungsten density (left) and radiation profiles obtained with medium (middle) and high (right) pedestal electron density

At the next step, we concentrate on the medium density H-mode regime and study the possibility to reduce the divertor heat loads using the Ne gas puff. As the Ne gas puff rate has been varied the different mechanism of COREDIV tungsten production at target plate play the role. In case without Ne the contribution to W sputtering are: self-sputtering (66%), deuterium sputtering (27%) and (7%)is sputtered by Be. At relatively low Ne gas puff (up to 10^{21} part/s) the tungsten self-sputtering reduces and W sputtering by deuterium vanishes. However, the W sputtering by Ne strongly increases raising the W concentration and core radiation (at Γ_{puff}^{Ne} = 4:15x10²¹1/s) 94% is sputtered by Ne and 6% is self-sputtered. The power to divertor plate reduces to 39 MW with Γ_{puff}^{Ne} = 1x10²¹1/s but the power through the separatrix also goes down due to large radiation (75 MW) approaching the L-H power threshold (Fig. 3b). The Ne seeding is accompanied by an increase of He concentration (Fig. 3c). He accumulation is caused mainly by the reduced He losses in SOL along the magnetic filed lines at lower plate temperature (i.e. lower parallel velocity), with a small contribution from increased He recycling (see Ref. [8] for COREDIV assumptions). Both Ne seeding and He accumulation contribute to dilution leading to reduction of alpha heating and fusion Q (Fig. 3d). With Ne gas puff above 1x10²¹/s the W sputtering reduces due to decrease of temperature at the divertor, and core radiation reduces.

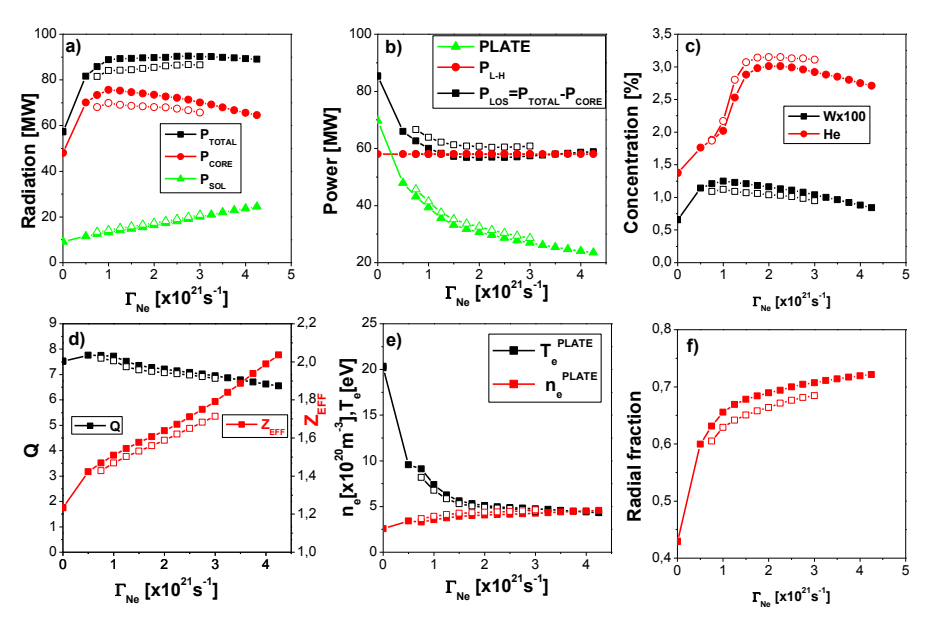


Fig. 3. Ne gas puff at medium density: total, core and SOL radiation (a), power to plate, L-H power threshold and power through the separatrix (b), W and He concentration (c), Z_{EFF} and fusion Q (d), temperature and density at the plate (e) and radiation fraction (f). Reference separatrix electron density is $n^{sep}_{e} = 3.25 \times 10^{19} m^{-3}$ (full symbols). Open symbols have been obtained with $n^{sep}_{e} = 3.5 \times 10^{19} m^{-3}$.

However, the total radiation remains the same due to increased SOL radiation with Ne puff (see Fig. 4 for Ne and W radiation profiles). Power to divertor reduces to 20 MW with $\Gamma_{puff}^{Ne} = 4:15 \times 10^{21} 1/s$ which may lead to acceptable heat loads (still more accurate divertor simulations are needed to determine the power distribution at the plates). However, since the W sputtering and core radiation with Ne seeding is larger than in the unseeded plasma the plasmas with Ne seeding will unlikely maintain the H-mode. The power through the sepatarix is close to the L-H power threshold with $\Gamma_{puff}^{Ne} > 1 \times 10^{21} part/s$. The attempt to find a more robust H-mode operational point with Ne seeding has been made by performing a scan in electron density at the separatrix determined by D recycling. When the sepratrix density n_{es} increases from $3:25 \times 10^{19} m^{-3}$ (ref. simulations shown by closed symbols on Fig. 3) to $3:5 \times 10^{19} m^{-3}$ (Fig. 3, open symbols) the temperature at the divertor reduces. As a result, the W sputtering and core radiation reduce and P_{loss} increases above L-H power threshold (Fig. 3b), but the effect of separatrix density on the power through the sepatarix is weak.

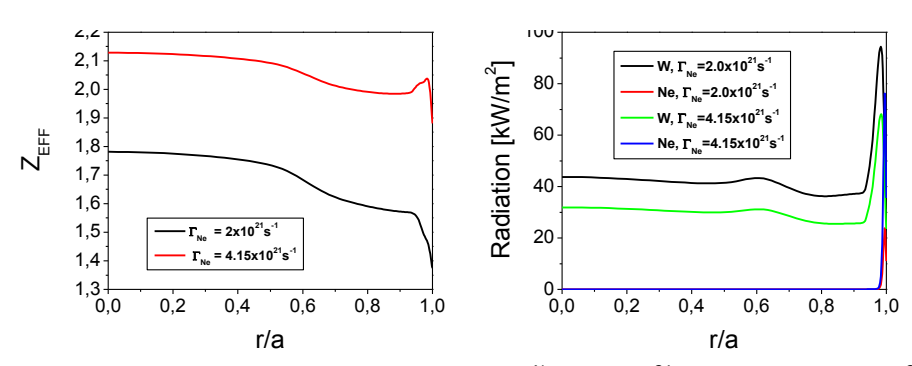


Fig. 4. Z_{EFF} (left) and W and Ne radiation (right) with Γ_{puff}^{Ne} = 2:0x10²¹ part/s and 4: 15x10²¹ part/s.

The sensitivity of W accumulation to inward tungsten pinch has been tested in simulations performed with $3.5 \times 10^{19} m^{-3}$ and $\Gamma_{puff}^{Ne} = 2.0 \times 10^{21} part/s$ by comparing the case with zero impurity pinch with the previously used assumptions of the same impurity pinch for W and deuterium (D pinch velocity required to reproduce the GLF23-computed density peaking is relatively large in these simulations ($V_{pinch}(r/a = 0.5) = 0.045 m/s$)). With zero inward pinch the W concentration and core radiation reduce only by 8.5% (see Fig. 5 left for W density profiles with and without inward pinch) and 2.4 MW correspondingly. The power to divertor increases heating the divertor plate and increasing the W production which in its turn compensates the effect of zero inward pinch. Such a strong coupling between the W accumulation, core radiation, power to divertor (34.8 MW) and W production prevents a large deviation from the reference operational point, leading to the H-mode operational point barely above the L-H power threshold ($P_{loss} = 63 MW$; $P_{LH} = 59:5 MW$). It should be mentioned also that the scan in the inward impurity pinch has been tested previously in the simulations of steady state ITER plasmas showing that the reduction of pinch velocity for all plasma species by factor 15 leads to the increases of fusion performance by 25%.

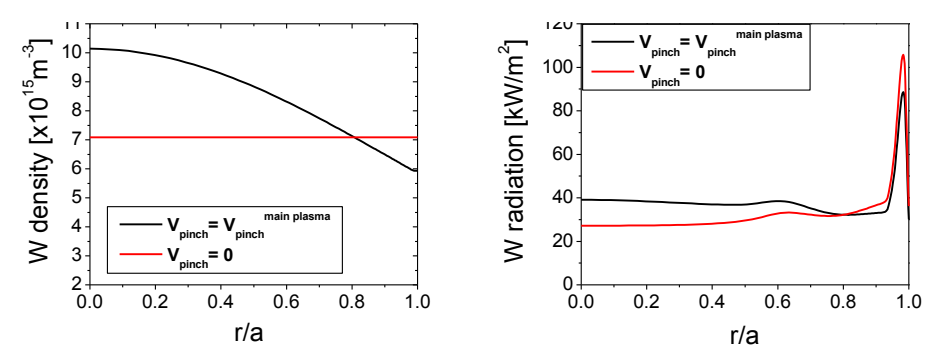


Fig. 5. Tungsten density (left) and radiation (right) obtained in simulations with $V_W = V_D$ (black) and $V_W = 0$ (red).

Conclusions

The core-pedestal-SOL modelling of ITER H-mode plasmas with intrinsic and seeded (Ne) impurities has been performed for two values of pedestal densities, n^{ped}_{e} = 6.12x10¹⁹m⁻³ (reference case) and 9.0x10¹⁹m⁻³ (artificially increased pedestal). JETTO and COREDIV transport codes have been used iteratively for this study, with the GLF23 computed thermal and particle transport for main species (JETTO) and similar transport coefficients for all impurities and main ions applied in COREDIV. Taking into account two essential constraints H-mode found that in case of medium density H-mode:

- Ne seeding is essential for reducing the power to plate below 40 MW
- W sputtering by Ne is important, it replaces the W self-sputtering leading to a larger W
 accumulation and core radiation than in the case without Ne seeding
- H-mode operational point with power to plate slightly below 40 MW is barely above the L-H
 power threshold in regimes with Ne seeding due to large W radiation. The H-mode operation is
 sensitive to the separatrix density and W inward pinch.

No H-mode operation at high density has been found in JETTO/GLF23 simulations using the radiation power estimated with COREDIV. In stand-alone COREDIV simulations performed with more optimistic transport model the H-mode operational point has been found, but with the power to divertor exceeding the operational limit (Ne seeding has not been applied in this case). It should be mentioned that the strong coupling between the W accumulation (or transport) and radiation, reducing the power to plate, divertor temperature and W production which in its turn affects the W accumulation leads to a stiff operational point and make it difficult to estimate in advance the trend with engineering parameters. More extensive parameter scans are needed to determine if the operational space for robust H-mode ITER performance with high fusion yield and acceptable level of divertor heat loads exist.

Collaboration

Association EURATOM/OAW, Atominstitut, TU Wien, Vienna, Austria
Association EURATOM/CCFE Fusion Association, Culham, Abingdon, Oxon. OX14 3DB, UK
Department of Applied Physics, Ghent University, B-9000 Gent, Belgium

References

- [1] Yu. F. Baranov, C. D. Challis, J. Hobirk, et al., 40th EPS conference on Plasma Physics, Espoo, Finland, 2013, pp.P5.142.
- [2] G. Cennacchi and A. Taroni, 1988 JET-IR(88) 03
- [3] R. Zagórski et al., Contrib. Plasma Phys. 48(1-3), 179 (2008).
- [4] R. E. Waltz, G. M. Staebler, et al, Phys. Plasmas 4, 2482 (1997).
- [5] W. A. Houlberg, K. C. Shaing at al., Phys. Plasmas 4, 3230 (1997).
- [6] P. B. Snyder et al., Nucl. Fusion 51, 103016 (2011).
- [7] Y. Martin et al., Journal of Physics: Conference Series 123, 012033 (2008).
- [8] R. Zagórski et al., Journal of Nuclear Materials.415, S483 (2011).

Numerical analyses of base line DEMO design concepts with the COREDIV code

Principal investigator:

R. Stankiewicz; <u>roman.stankiewicz@ipplm.pl</u>
Collaborators from the Institute of Plasma Physics and Laser Microfusion:
I. Ivanova-Stanik, W. Stępniewski, R. Zagórski

Introduction

New DEMO design concepts [1.2] has been analyzed with the help of COREDIV code [3], which describes self consistently the core and the scrape off layer with the divertor regions (SOL) of tokamak plasmas. The coupling between core and SOL is imposed by continuity condition at separatrix of values and fluxes of temperatures and densities. In the core the 1D transport equations for densities and temperatures are used. The EPIT code is used to analyze the SOL domain. The SOL is describe by 2D fluid equations developed by Braginskii [3]. In both domains it is assumed that all ions have the same temperature. All ionization states of impurity ions are considered separately in both domains. The sputtering processes of tungsten at target plate by all ions are taken into account.

The influence of pinch velocity on the parameter of the discharges has been analyzed. The transport model relies strongly on the concept of energy confinement time. More precisely the transport coefficients are defined by the relation:

$$\chi_e^{an} = \frac{C_e}{\tau_e} \left[0.25 + 0.75 \left(\frac{r}{a} \right)^4 \right] FSB(r)$$

$$\chi_i^{an} = \chi_e^{an}, \quad D_i^{an} = 0.35 \chi_e^{an}$$

$$V_j^{pinch} = -C_v \left(\frac{\tau_e}{2.8} \right)^2 D^{an} \frac{r}{a^2}$$

where au_E is the energy confinement time χ_e^{an} , χ_i^{an} are electron and ion anomalous conductivity, and D^{an} is the anomalous diffusion coefficient. The function FSB has been introduce to model the drop of the transport coefficients near the separatrix corresponding to transport barrier formation. The constant C_e is adjusted in calculation to fulfill the condition $\frac{W_E}{P_e}P = CP_h^{-0.7}$ according to scaling law.

The new DEMO design concepts has been analysed numerically with the help of Corediv code describing self consistently the core and the scrape of layer with divertor region. The consistency of the plasma parameter has been checked. The details of the discharge has been obtained. The possibility of reduction of the power load to divertor plate using seeded impurities has been investigated. The dependence of plasma parameters on pinch velocity, additional heating power has been analysed.

Analyses of DEMO1 concept.

The consistency of the basic Demo1[1] design prepared with the help of Process code has been check with the help of COREDIV code. The scan of the plasma parameter with respect of the concentration of argon as seeded impurities has been performed. The dependence of the parameters on the concentration of seeded impurities (argon) for pinch velocity defined by cv=0.1 are shown on Fig.1 and for c_v =0.5 on Fig.2. For c_v =0.1 it was demonstrated that the concentration of seeded impurity can be increase to the level that the energy to target plate is closed to zero and the sputtering processes are stopped at target plate. The alpha power is reduced with the increase of seeded impurity radiation and the confinement time increases. This leads to increase of concentration of helium and further decrease of the alpha power. For some value of Argon concentration zero energy flowing to target plate is obtained.. The basic plasma parameters are compared with reference value obtained in [1]

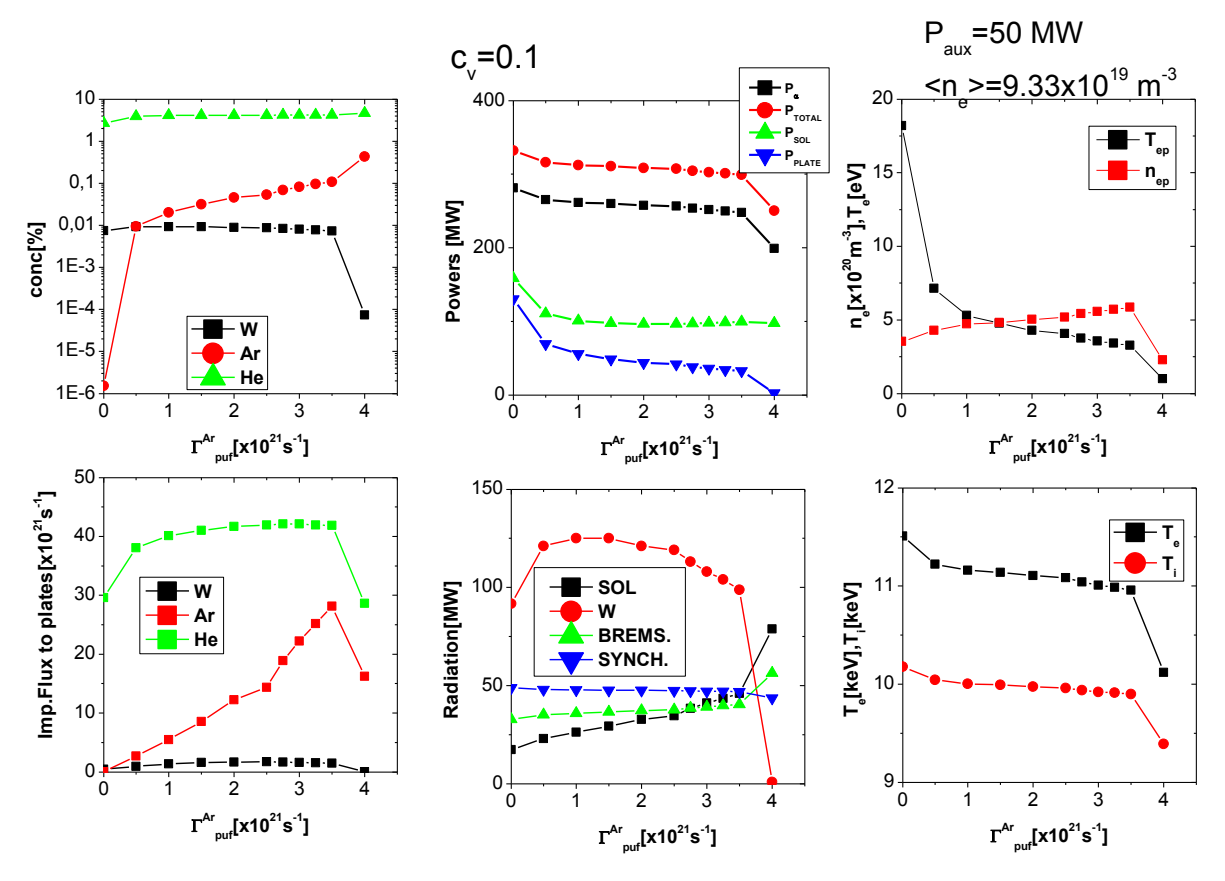


Fig. 1. The dependence of plasma parameter on gas puff intensity (argon) for pinch velocity defined by c_v =0.1.

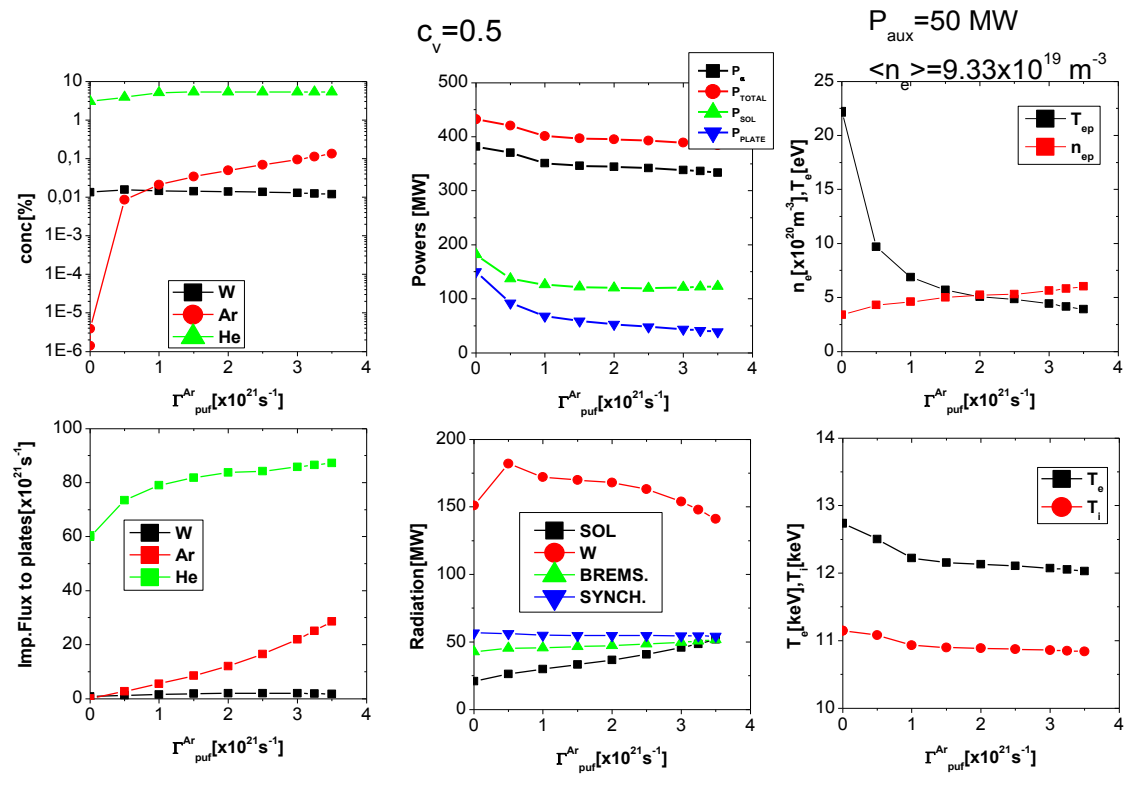


Fig. 2. The dependence of plasma parameters on gas puff intensity (argon) for pinch velocity defined by c_v =0.5.

Table 1. Comparison the results of COREDIV with the design parameter obtained by PROCESS (DEMO1)

PARAMETERS	PROCESS	COREDIV	COREDIV	COREDIV	COREDIV	COREDIV	COREDIV
Cp (pinch factor) – main ions		0.1	0.5	0.1	0.5	0.1	0.5
n _e (0)/ <n<sub>e></n<sub>	1.3	1.12	1.32	1.12	1.32	1.12	1.32
Impurity pinch		V imp =0 =0 17 -1	V imp =0	V imp =0 =0 21 -1	V =0 =0	V imp =0 pinch =21 -1	
Ar gas_puff (s ⁻¹)		1.0x10 ¹⁷ s	1.0x10 ¹⁷ s	1.5x10 ²¹ s			3.5x10 ²¹ s
R ₀ , a (m)	9.0, 2.489	9.0, 2.49	9.0, 2.49	9.0, 2.49	9.0, 2.49	9.0, 2.49	9.0, 2.49
Plasma current, I _P (MA)	16.789	16.79	16.79	16.79	16.79	16.79	16.79
Elongation, κ ₉₅	1.564	1.56	1.56	1.56	1.56	1.56	1.56
Temperature, <t<sub>e'vol> (keV)</t<sub>	12.87	11.51	12.74	11.14	12.16	10.96	12.03
Z _{eff}	2.684	1.28	1.48	1.44	1.64	1.62	1.82
Helium fraction	0.1	0.027	0.03	0.041	0.0526	0.0418	0.0533
Power to plate (MW)		131	150	48.8	122	32.6	123
Fusion power, P _{fus} (MW)	1793	1406	1906	1300	1732	1240	1667
Auxiliary heating, P _{inj} (MW)	50	50	50	50	50	50	50
P _{synch} (MW)	35.99	49	56.8	47.7	54.9	46.9	54.3
P _{brem} (MW)	102.1	32.8	42.68	36.6	46.5	40.4	51.7
P _{line} (MW)	122.7	71.9	118	101.1	136	86.1	119
Radiation fraction		0.575	0.63	0.78	0.776	0.82	0.814
H-mode thres., P _{L-H} (MW)	142±22.5.	97.94	101.4	98.06	101.8	98.14	102
Confinement time, τ_{E} (s)	3.894	3.54	2.98	3.72	3.19	3.84	3.27
H-factor	1.1	1.1	1.1	1.1	1.1	1.1	1.1
Power to divertor (MW)	148.7	158.4	182.2	97.6	122	99.6	123
T _e (0)/ <t<sub>e></t<sub>	2.0	2.45	2.32	2.66	2.36	2.61	2.4
Separatrix density (10 ²⁰ m ⁻³)	0.36	0.4	0.4	0.4	0.4	0.4	0.4

Analyses of DEMO2 concept

The analyses of influence of value of auxiliary heating on plasma parameters was analyzed numerically using COREDIV. The results are presented on Fig. 3-4. Similarly as case of DEMO1 there is the possibility of reduction of power load to divertor plate to zero for auxiliary heating of 200 MW. The mechanism is similar as for in case of DEMO1. The table2 contains the comparison of the reference plasma parameter parameters [2] and calculated using COREDIV.

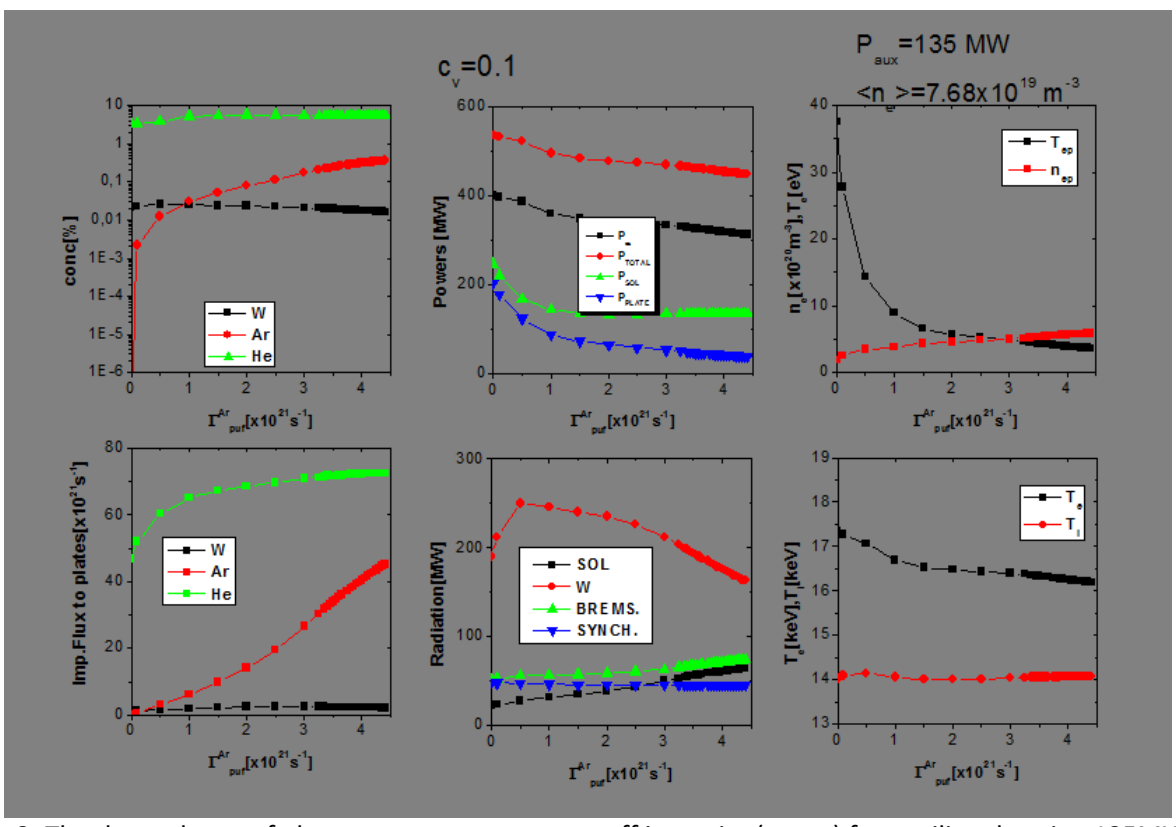


Fig. 3. The dependence of plasma parameter on gas puff intensity (argon) for auxiliary heating 135MW.

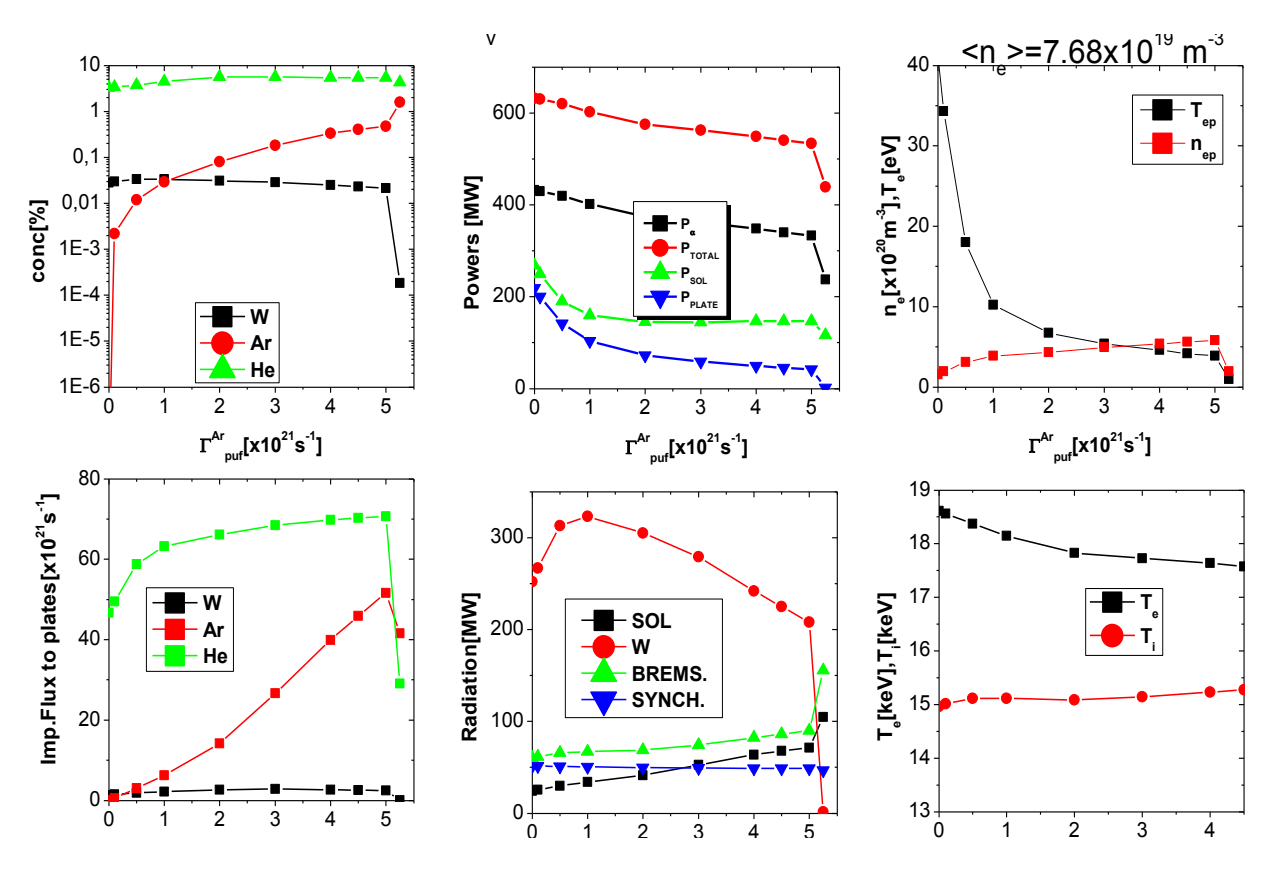


Fig. 4. The dependence of plasma parameter on gas puff intensity (argon) for auxiliary heating 200 MW.

Table 2. Comparison the results of COREDIV with the design parameter obtained by PROCESS (DEMO2)

	DEMO2							
PARAMETERS	PROCESS	COREDIV	COREDIV	COREDIV	COREDIV	COREDIV	COREDIV	
Cv (pinch factor) – main ions		0.1	0.1	0.1	0.1	0.1	0.1	
n _e (0)/ <n<sub>e></n<sub>	1.3	1.086	1.074	1.09		1.09	1.08	
Impurity pinch		V _{pinch} imp=0						
Ar gas_puff (s ⁻¹)		1.0x10 ¹⁷ s ⁻¹	1.0x10 ¹⁷ s ⁻¹	2.5x10 ²¹ s ⁻¹	3.0x10 ²¹ s ⁻¹	4.4x10 ²¹ s ⁻¹	5.25x10 ²¹ s ⁻¹	
R ₀ , a (m)	8.152,2.982	8.15,2.98	8.15,2.98	8.15,2.98	8.15,2.98	8.15,2.98	8.15,2.98	
Plasma current, I _P (MA)	19.849	19.85	19.85	19.85	19.85	19.85	19.85	
Elongation, κ ₉₅	1.614	1.61	1.61	1.61	1.61	1.61	1.61	
Temperature, <t<sub>e,vol> (keV)</t<sub>	15.453	17.34	18.61	16.43	17.73	16.19	17.51	
Z _{eff}	3.28	1.73	2.05	2.2	2.61	2.74	3.24	
Helium fraction		0.0328	0.0329	0.0581	0.0564	0.0567	0.0539	
Power to plate (MW)		204	218.72	58.52	58.9	39.4	42.04	
Fusion power, P _{fus} (MW)	2104	2000	2159	1645	1810	1563	1663	
Auxiliary heating, P _{inj} (MW)	135	135	200	135	200	135	200	
P _{synch} (MW)	34.18	48.2	51.6	45.9	49.3	45.24	48.7	
P _{brem} (MW)	170.5	50.6	60.34	60.63	74.2	73.94	155.5	
P _{line} (MW)	249.8	149.7	199	184.6	230.1	147.1	69.8	
Radiation fraction		0.58	0.615	0.81	0.838	0.84	0.86	
H-mode thres., P _{L-H} (MW)		73.8	73.7	74	73.8	74	73.8	
Confinement time, τ_E (s)	3.955	2.94	2.6	3.217	2.84	3.36	2.95	
H-factor	1.3	1.3	1.3	1.3	1.3	1.3	1.3	
Power to divertor (MW)	101	246.9	267.9	131.9	144	135.3	146.7	
$T_e(0)/$	2	2.48	2.56	2.68	2.72	2.6	2.8	
Separatrix density (10 ²⁰ m ⁻³)		3.8	3.8	3.8	3.8	3.8	3.8	

Numerical analyses of DEMO1 new working point (December 2013)

The calculation has been performed with velocity pinch factor Cv for main ions and zero velocity pinch for impurities. Beside the radial diffusion coefficient in SOL was decreased from 0.5 m²/s, used in other presented numerical test, to 0.25m²/s in order to get working point closer to proposed by Process. Basic plasma parameter are presented in Table 3 and on Fig. 5 and Fig. 6.

Table 3. Comparison the results of COREDIV with the design parameter obtained by PROCESS (DEMO1 new working point December 2013)

	Process	Corediv	Corediv	Corediv	Corediv	Corediv
Ar gas puff (s-1)		1.0x10 ¹⁷	1.0x10 ²⁰	2.5x10 ²⁰	3.0x10 ²⁰	3.5x10 ²⁰
C _v pinch main ions	0.5	0.5	0.5	0.5	0.5	0.5
Confinement time	4.161	3.54	2.98	3.72	3.19	3.84
<z<sub>eff></z<sub>	2.82	1.9280	1.9447	1.9713	1.9745	1.9801
POWERS (MW)						
Fusion power	2110	2069	2038	2119	1935	1910
Auxiliary power	50	50	50	50	50	50
Power to divertor	157	149	135	115.95	109.	103
RADIATION (MW)						
Bremsstrahlung	118	52.72	53.15	53.85	53.96	54.14
Synchrotron	54	69.37	68.97	68.06	67.65	67.29
Line	145	127.52	128.61	129.74	128.86	128.31
SOL radiation		21.28	22.18	23.45	24.12	24.61
Radiation fraction		0.657	0.671	0.697	0.705	0,713

IONS						
$n_e(0)/< n_e>$	1.3	1.12	1.32	1.12	1.32	1.12
$T_e(0)/$	2.0	2.13	2,13	2,13	2.13	2.11
Helium fraction		0.051	0.055	0.063	0.066	0.0695
Separatrix density (10 m)		0.487	0.487	0.486	4.867E+19	4.858E+19

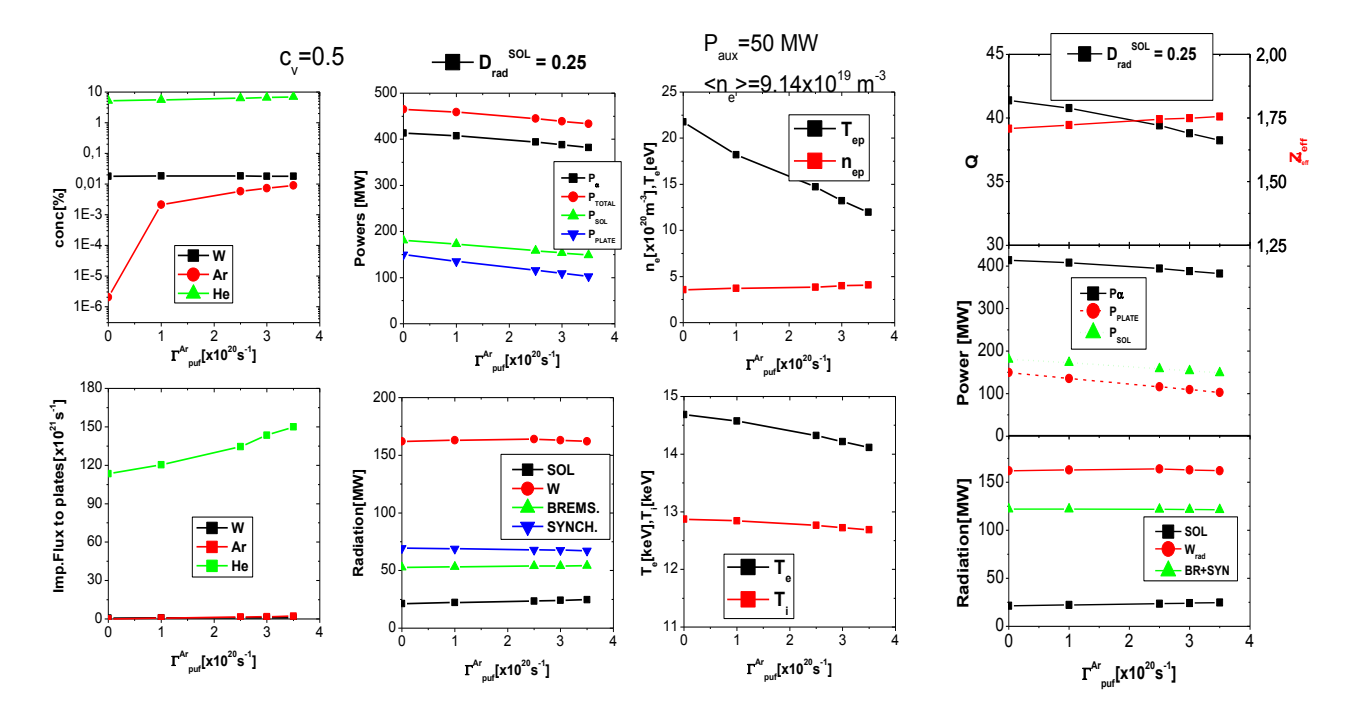


Fig. 5. The dependence of plasma parameter on gas puff intensity (argon) for DEMO1 new working point.

The calculation has been performed with velocity pinch factor C_{ν} for main ions and zero velocity pinch for impurities. Beside the radial diffusion coefficient in SOL was decreased from

Limit on impurities concentration.

In order to understand the mechanism increasing plasma contamination and leading to a termination of the solution the core and sol region were considered separately. As a starting point, the self-consistent solution for DEMO1 is taken into account. The basic parameter for considered DEMO concept are: large radius R=9m, small radius a=2.25m, plasma current Ip=7.2MA, toroidal magnetic field B_T =7.2T, elongation k_{95} =1.33, safety factor q_{95} =3, separatrx electron density n_{95} =3.5E19m⁻³, averaged electron density n_{95} =3.8e19m⁻³, scaling factor H=1, auxiliary heating n_{95} =3.

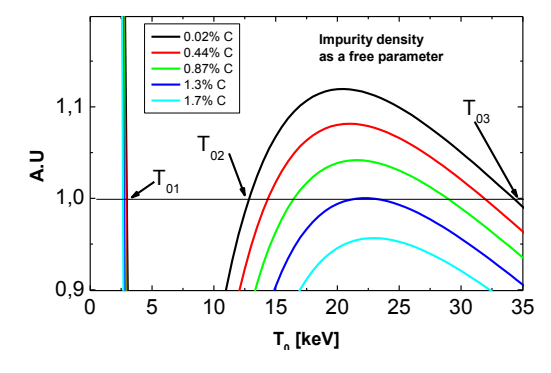


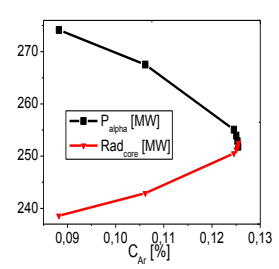
Fig. 6. The possible solution to transport equation.

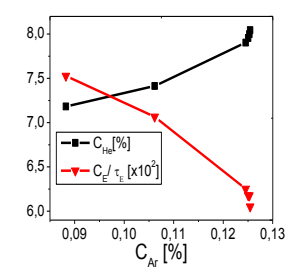
The uncoupled core problems are solved with the boundary condition on separatrix taken from the solution of coupled core-SOL problem for argon gas puff Γ^{Ar}_{puff} =2.0 x10²¹ s⁻¹. The concentration of impurities densities was modified be multiplying the boundary values at the separatrix by some value. The analyses of 0D problem shown that there is the limit on admissible impurity concentration [5]. The energy balance for 0D problem can be written in the form:

 $\frac{3 < nT >}{\tau_{o}} = P_{OH} + P_{\alpha} - P_{B} - f_{rad}P_{lin} = P_{core}$ where the quantity on right hand side are calculated from parabolic

profiles. The function $\frac{P_{core}\tau_e}{3.nT}$ is plotted on Fig.6

The plot shows clearly that solution that the solution does not exist for strong radiation. The plasma parameters calculated by Corediv are presented on Fig.6 as function of impurity concentration.





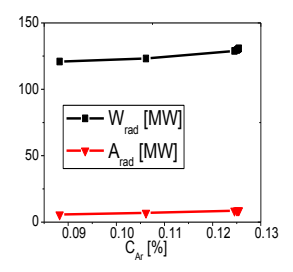
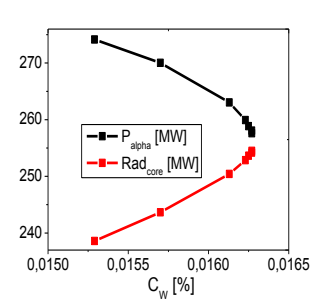
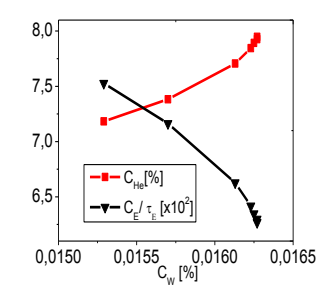


Fig. 7. The alpha power P_{alpha} , radiation losses in the core Rad_{Core} , concentration helium C_{He} , tungsten and argon radiation W_{rad} , A_{rad} as a function argon concentration C_{Ar}

The similar effect has been observed for increase of tungsten concentration as was shown on Fig.8





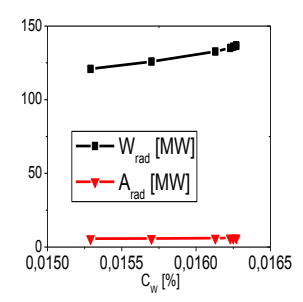


Fig. 8. The alpha power P_{alpha} , radiation losses in the core Rad_{Core} , concentration of helium C_{He} , tungsten and argon radiation W_{rad} , A_{rad} as a function tungsten concentration C_w .

The integration of the equations describing the evolution of ion and electron temperature over radial coordinate leads to the following equation:

$$\frac{dW}{dt} = P_h - P_{loss} - \frac{C_e}{\tau_e} \Gamma \tag{1}$$

where W is total thermal plasma energy, P_h and P_{loss} are total heating power and total losses. The last term correspond to energy flux on separatrix. The scaling of energy confinement time expressed approximately by formula $\tau_e = c P_h^{-0.69}$ and the definition of $\tau_e = W/P_h$ lead to the formula

$$W = cP^{0.31}$$

The graphs show that the plasma parameters change with increasing steepness for argon concentration approaching some critical value. Continuation of time evolution with small increase of impurity concentration (probably above critical point) leads to rapid decrease of the energy flux to the SOL and shortly the flux became negative in order to keep the thermal energy W defined by scaling law. Of course negative energy fluxes are unphysical. The nonlinear couplings leads to the situation that there exists the limit on impurities concentration and as a consequence the limit on energy flux to the SOL below each the physically reasonable solution does not exist, similarly as for simpler OD problem.

Conclusions

The obtained global parameters using COREDIV are closed to proposed by PROCESS but depend strongly on seeded impurities concentration and velocity pinch. There is the limit on admissible concentration of impurities above which the solution does not exist. The limit is defined by dilution of plasma (helium) and impurities radiation. There are two cases presented above where solutions exist for the power to plate reduced to zero. In this cases the sputtered impurity concentration is equal to zero. The seeded impurities can radiate in SOL the total power flowing to SOL.

The tests performed for uncoupled core problem show that even in this case the limit on impurities concentration exists. The numerical results follows in this case the tendencies predicted by simpler model (0D).

Collaboration

Euratom Assotiation CEA.
Consorzio RFX-Associazione EURATOM ENEA per la Fusione, I-35127 Padova, Italy EURATOM Association, Max-Planck-Institut für Plasma Physics CCFE, Culham Science Centre

References

- [1] Richard Kemp_, David Ward, WP12-SYS01-D11_DEMO1_final_report.pdf
- [2] Richard Kemp_, David Ward, WP12-SYS01-D12_DEMO2_final_report.pdf
- [3] R. Stankiewicz and R. Zagórski, J.Nucl.Mater. 337-339 (2005) 191
- [4] S.I. Braginskii, Rev. Plasma Phys. 1 (1965) 205
- [5] R. Zagórski, IFTR reports 5 (1998)
- [6] K. Borrass, 1991 Nucl. Fusion 31 (1991)1035

Benchmarking of MC tools on DEMO Monte-Carlo simulations of neutron distribution at DEMO

Principal investigator:

B. Bieńkowska; <u>barbara.bienkowska@pplm.pl</u>
Collaborators from the Institute of Plasma Physics and Laser Microfusion:
R. Prokopowicz

Introduction

Neutronic calculations for the DEMO tokamak were released during last two years. They were spread in two directions: neutron reactions with construction materials and development of the neutronic codes. Within the IPPLM tasks, neutron heating at the DEMO inboard divertor rail was studied [1] with the Monte Carlo method and a collaborative work was started for comparison of MC codes [2] being alternative to MCNP in the context of uncertainty of access to it in future. In that previous work (WP12-DTM-04-T11), some European MC codes were selected regarding their "fusion capability". The aim of this year's task (WP13-SYS-T10-01) was to conclude the work started.

A DEMO relevant benchmark between the selected candidates (TRIPOLI-4, SERPENT2 and FLUKA) is carried out. Three associations participate to this task: CEA (TRIPOLI-4 DEMO model and MCNP5

calculation), CCFE (SERPENT DEMO model) and IPPLM (FLUKA DEMO model). A work on Monte Carlo simulations of neutron distributions at DEMO was continued. The IPPLM contribution to task WP13-SYS-02-T10-01 is described in this report. The attempts have been done to convert geometry of DEMO from CAD to MCNP and FLUKA. Possibility of writing a special neutron source subroutine for FLUKA has been analysed. Possible future activities are proposed.

IPPLM contribution: FLUKA DEMO model and results

It was expected to perform DEMO-relevant benchmark exercise on the neutron transport simulation capabilities of FLUKA [3], [4]. Main issues were to evaluate potential and limitations in the preparation of a DEMO-relevant model, to model the neutron source and to verify neutron transport calculations (in comparison to the MCNP [5] calculations). The generic DEMO model has been prepared under task T05 and has became available together with the plasma neutron source as FORTRAN source subroutine. The model is in CAD available as a step file. It has been decided to use MCAM code [6] in order to import geometry from CAD to MCNP and FLUKA.

MCAM code

Two versions of interface code MCAM have been obtained from the FDS¹ team: MCAM 4.8.5.50 Standard Edition (for MCNP) and MCAM 5.2 The DEMO 22.5 deg step file read by both codes can be seen in Fig. 1. The geometry can be viewed interactively in 3D.

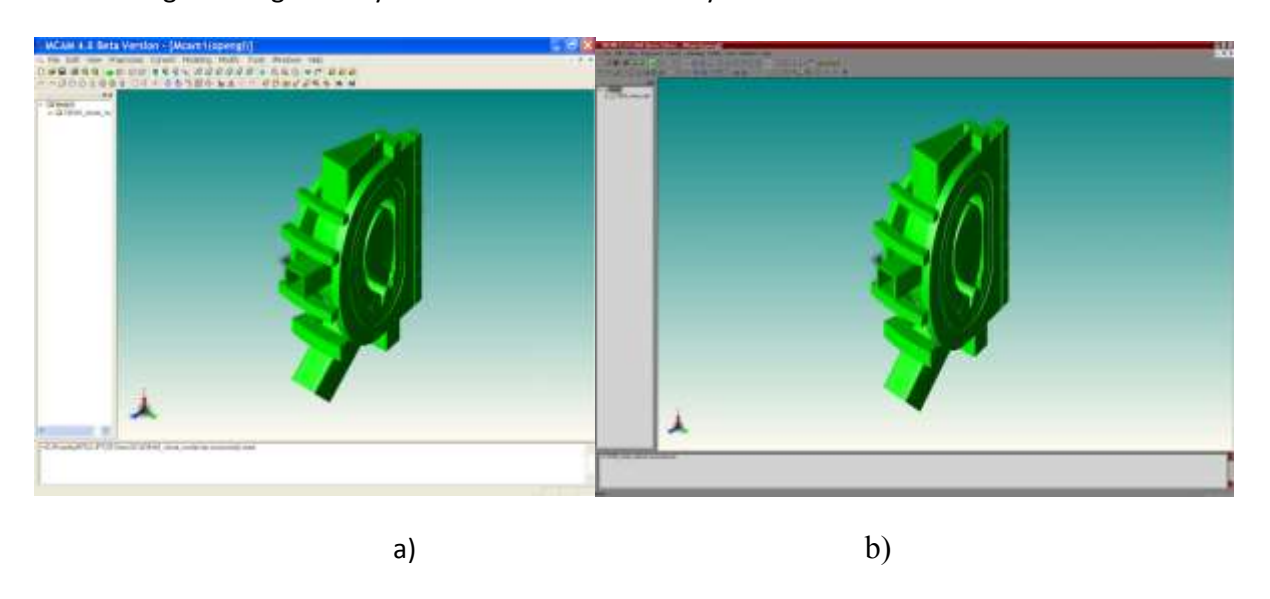


Fig. 1. DEMO 22.5 deg step file from: a) MCAM 4.8.5.50 Standard Edition, b) MCAM 5.2 FLUKA Demo Edition.

Transformation from CAD to MCNP

The MCNP geometry input generated by MCAM 4.8.5.50 Standard Edition has been read by VisEd program and can be seen in Fig. 2. Red lines indicate geometry errors. There are no materials specified in the input.

¹FDS – Professor Yican Wu, Institute of Plasma Physics, Chinese Academy of Sciences. Hefei, Anhui, China.

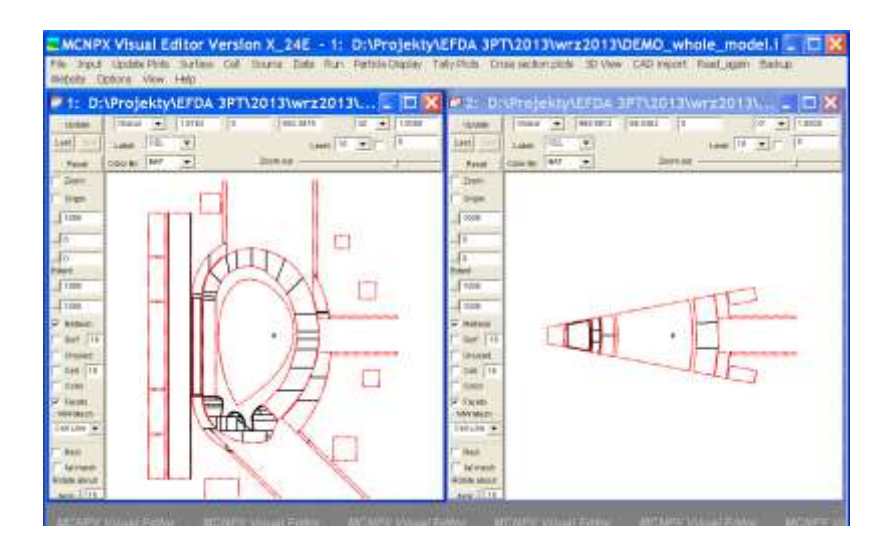


Fig. 2. MCNP geometry input generated by MCAM 4.8.5.50 Standard Edition from DEMO 22.5 deg step file.

Transformation from CAD to FLUKA

MCAM 5.2 FLUKA Demo Edition was used to convert the existing CAD models of DEMO in order to obtain the geometrical part of a FLUKA input. Since the program is under development, the beta version of MCAM allows to transform solely 50 cells at one run. Therefore, the conversion was carried out step by step for both 11.25 and 22.5 degrees DEMO models. Because the 11.25 deg model consists of 270 cells, six separate transformations were needed. In the latter case (411 cells) nine conversion were performed. Then the partial FLUKA inputs were merged into one large file that contained all modelled elements of DEMO. Since MCAM does not allow to convert the entire geometry in one run, vacuum has to be modelled manually because void cells created in separate transformations overlap, of course. Care was taken to numerate both FLUKA bodies and regions (cells) so that they were different for successive conversions. Unfortunately, attempt to convert the central region of DEMO (Fig. 3 and 4) failed for both 11.25 and 22.5 deg models. In the former case it comprises of 9 cells while for the full DEMO model it is only one cell. It appears this area must be modelled manually, just like void, unless a new version of MCAM is released.

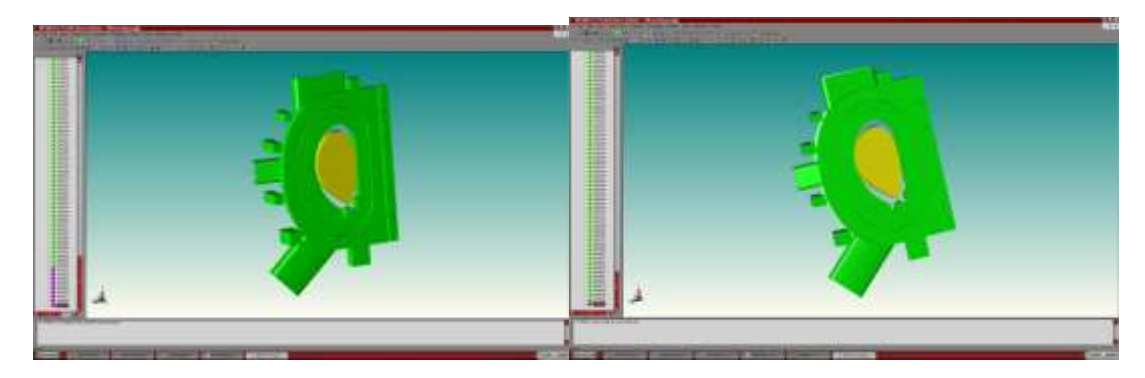


Fig. 3. The 11.25 deg model. The nonconvertible cells (261-269) are highlighted in yellow.

Fig. 4. The 22.5 deg model. The nonconvertible cell (411) is highlighted in yellow.

The geometry of DEMO 11.25 deg converted to FLUKA can be seen in Fig. 5. Program Flair has been used for visualization of the input. Red lines indicate geometry errors. There is no materials information in the input.

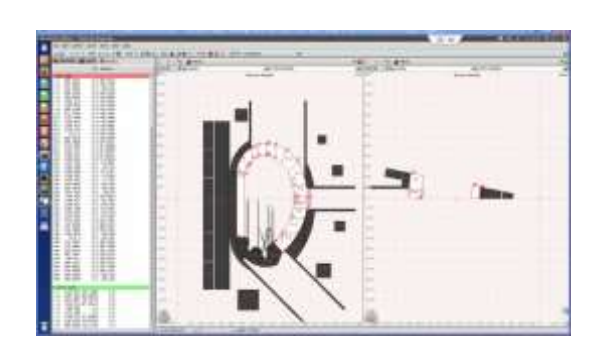


Fig. 5. FLUKA geometry input from by MCAM 5.2 FLUKA Demo Edition from DEMO 11.25 deg step file.

Neutron source subroutine for FLUKA

It is possible to write the neutron source subroutine for FLUKA based on the source subroutine for MCNP. Main effort would be devoted to implementation into FLUKA some features which are specific to MCNP. The subroutine should be precisely tested if it generates assumed source of neutrons.

Possible future activity

Correction of errors in geometrical inputs for MCNP and FLUKA is the primary goal for future activity. Then the full material definition has to be added to both inputs. Source subroutine for FLUKA should be written, tested and applied to the input. The last step would be a comparison of neutronic calculations made with MCNP and FLUKA.

Conclusions

The main activity for FLUKA was the CAD import testing. MCAM version 5.2 was employed. It is promising for FLUKA model generation but corrections are necessary. Thus, the FLUKA DEMO generic model has not been fully completed and it was impossible to achieve a final benchmark.

Collaboration

The Henryk Niewodniczański Institute of Nuclear Physics of the Polish Academy of Sciences, Kraków D. Dworak, G. Tracz

Association Euratom - CCFE

Association Euratom - CEA

References

- [1] G. Tracz, *Neutron heating at the DEMO inboard divertor rail*. Annual Report 2012 of the Assoc. EURATOM-IPPLM (2013), in CD 3.1.TM(9), 7pp.
- [2] K. Drozdowicz, B. Bieńkowska, D. Dworak, R. Prokopowicz, *Activities in support to DEMO design: Monte Carlo Codes Comparision*. Annual Report 2012 of the Assoc. EURATOM-IPPLM (2013), in CD 3.1.TM(10), 5pp.
- [3] G. Battistoni, S. Muraro, P.R. Sala, F. Cerutti, A. Ferrari, S. Roesler, A. Fassò, J. Ranft, "The FLUKA code: Description and benchmarking" Proceedings of the Hadronic Shower Simulation Workshop 2006, Fermilab 6 8 September 2006, M. Albrow, R. Raja eds., AIP Conf. Proc. 896, 31-49, (2007)
- [4] A. Ferrari, P.R. Sala, A. Fassò, and J. Ranft, "FLUKA: a multi-particle transport code" CERN-2005-10 (2005), INFN/TC 05/11, SLAC-R-773
- [5] X-5 Monte Carlo Team, MCNP, LANL report LA-UR-03-1987, 2003.
- [6] Y. Wu, FDS Team, CAD-based interface programs for fusion neutron transport simulation, Fusion Eng. Des., 84 (2009) 1987-1992.

2.2 Fusion Plasma Diagnostics

Development of soft X-ray triple GEM gas detector for energy resolved soft X-ray plasma diagnostics

Principal investigator:

M. Chernyshova; <u>maryna.chernyshova@ipplm.pl</u>
Collaborators from the Institute of Plasma Physics and Laser Microfusion:
T. Czarski, K. Jakubowska, J. Rzadkiewicz

Introduction

The high-resolution X-ray spectroscopy is a powerful tool for diagnostics of plasma state evolution in tokamak. X-ray spectra in tokamak plasma origin from continuum (bremsstrahlung)and characteristic atomic radiation. In particular at JET tokamak, besides the bremsstrahlung radiation, the intense characteristic radiation is emitted by highly ionized tungsten and nickel impurities wrested from the construction materials during plasma discharges. This characteristic radiation provides accurate information on the crucial plasma parameters such as impurity concentration, ion temperature, and the toroidal rotation velocity [1]-[2]. High-resolution X-ray diagnostics for magnetic confinement fusion devices is employed for regular monitoring of the X-ray radiation at specific ranges of photon energies. At JET two independent diagnostic channels, based on the Bragg crystal X-ray spectroscopy (with very high energy resolution, $E/\Delta E$ up to 20 000, comparable to the natural widths of the measured X-ray lines allowing very good selectivity), have been set for monitoring plasma emission spectra at specific photon energy windows what corresponds to specific diffraction orders. The first diagnostic channel (employing (1011) SiO2 crystal) is dedicated to monitor the radiation emitted by W⁴⁶⁺ at about 2.4 keV observed in the 1st diffraction order. This channel is able to register simultaneously the continuum radiation emitted at ~2.4 keV, ~4.8 keV and ~7.2 keV photon energy windows (defined by Bragg diffraction geometry), corresponding to the 1st, 2nd and 3rd diffraction orders, respectively. Radiation intensity measured in each order depends on the plasma electron temperature. Continuum radiation component forms flat and smooth distribution in the detection plane. Characteristic emission related to impurities appears as one-dimensional diffraction pattern. The second diagnostic channel (employing (220) Ge crystal) monitors the radiation emitted by Ni26+ at about 7.8 keV observed in the 2nd diffraction order as the diffraction pattern in the detection plane. This detection unit registers also the continuum radiation at photon energies of ~3.9 keV, ~7.8 keV and ~11.7 keV corresponding to the 1st, 2nd and 3rd diffraction orders, respectively, with the intensity defined by plasma electron temperature. Two independent detecting systems with high counting rate capability and very good spatial resolution in one dimension are required to register the characteristic emission lines of impurities and the continuum radiation background in a broad range of energy.

The ITER-oriented, especially ITER-Like Wall, tokamak research program brings a new important requirement for the X-ray diagnostics which is expected to monitor the impurity level of tungsten – the plasma-facing material. Therefore, for high-resolution X-ray measurements development of new detection techniques based on new generation GEM X-ray detectors is essential for efficient plasma monitoring. For the purpose of detecting X-ray lines intensities from the energy resolved diagnostics two gas detectors based on Triple-GEM technique [3]-[4] were developed. The gas amplification stage is followed by the strip readout electrode in order to measure diffraction pattern related to the specific soft X-ray energy range. In this report we present the studied capabilities of Triple-GEM detecting units developed and constructed to fulfil the requirements for soft X-ray monitoring in JET [2]-[5] tokamak.

Two Triple Gas Electron Multiplier (Triple-GEM) detectors were developed for high-resolution X-ray spectroscopy measurements for tokamak plasma to serve as plasma evolution monitoring in soft X-ray region (SXR). They provide energy resolved fast dynamic plasma radiation imaging in the SXR with 0.1 kHz frequency. Detectors were designed and constructed for continuous data-flow precise energy and position measurement of plasma radiation emitted by metal impurities. High counting rate capability of the detecting units has been achieved with good position resolution.

Detectors structure and electronics configuration

As was shown in the previous annual report the detector amplification structure consists of three GEM foils allowing high amplification of the primary charge produced in the detector sensitive volume by photon absorption. The internal structure of the GEM detector allows to separate the amplification and read-out stages. Thus, the shape of the flat readout electrode closing the detector does not influence the amplification process. This provides a large degree of freedom in construction of the readout structure that is optimal for the detection position resolution. In the studied structure we used the strip readout plate with 0.8 mm strip pitch. Since the low energy photons are suffered from high absorption even along 1 cm distance in air we designed and constructed also He buffer between the detector and spectrometer arm (Fig. 1)

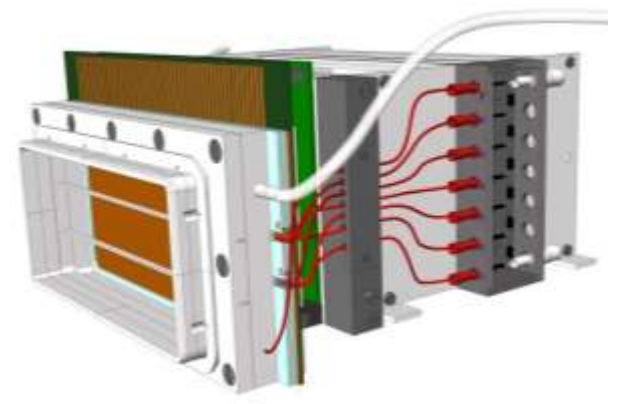


Fig. 1. Assembled final GEM detector with mounted He buffer frame.

Gas mixture and window materials were optimized for two energy regions in order to find the best gas mixture and the detector window material to obtain the maximum efficiency for detection of 2.4 keV (W⁴⁶⁺) and 7.8 keV (Ni²⁶⁺) photons. Conversion efficiency for detector filled with Ne+CO₂, Ar+CO₂ and Ar+CF₄ for 1.5 cm gas layer with different ratio of used gas with included 6 μm and 12 μm of Mylar foil metallized by 0.2 μm of Aluminium was calculated. The window of the detector serves also as a cathode in GEM detector system and for this purpose material of window is a thin metallized foil. The thickness is especially important in case of 2.4 keV photons, because they could be easily absorbed even in thin metallized foils. Here we present the results with the chosen working gas of ArCO2 (70:30) of 15 mm thickness of gas-mixture layer. In this case detection efficiency above 40% for 2.4 keV and around 20% for 7.8 keV may be achieved. Electronics for final detectors is dedicated to acquire, primarily process and prepare histograms of detector signals with high time resolution. Each detector's electronics consists of detector strip board with backplane, amplifiers and differential cable drivers board - 16 Analogue Front End boards (AFE), 16 FPGA Mezzanine Cards (FMC) digital boards, the carrier module with 16 FMC slots and high and low voltage power supply module (PSU). Each strip dedicated AFE channel consists of transimpedance amplifier with 20 kV/A gain, 15 MHz RC low-pass filter, cable driver and analogue-to-digital converter (ADC). Individual signal from each channel transferred through amplifier and filter is shaped within 200 ns window. The 15 MHz AFE channel bandwidth was chosen to match timing characteristics of the primary pulse. The shaped signal is then digitized by pipelined 10 bit ADCs at 77.7 MHz sampling rate. The detector electronics processing unit has 256 readout channels per each detector.

The hardware and functional concentration is implemented at three levels:

- 1. 16 analogue signals from the T-GEM detector are converted with frequency of 77.78 MHz to 10-bit digital signals and transmitted into the FPGA on a single FMC board. The trigger signals are generated independently for each channel [6] in a block TRIGGER CONTROL (Trigger Controller). The trigger signal provided to the channel n initiates the processes of charge identification [7] for <n-2, n+2> channels in a block CHARGE IDENTIFIER. Number of channels has been adjusted accordingly to the size of the charge generated in the T-GEM detector (common charge produced by a single photon is called cluster),
- 2. The charge values from 64 channels (from four FMC embedded) are received by a single CAR board. On the basis of coincidence in the time, position and the value of charge, it is possible to determine clusters [6] in the block CLUSTER IDENTIF. (Cluster Identifier). The values of clusters are stored for further histogramming process. The histogramming process is performed in real time for the input values range from 0 to 511 (9 bits of resolution) and for counting range from 0 to 65535 (16 bit resolution). An internal memory blocks of FPGA (BRAM) was used for histogramming process implementation to reduce the number of logic blocks usage [8]. A scaling operation (i.e. the adjustment of the clusters values range) is performed before histogramming process. The histogramming process was implemented independently for each FMC board (for 16 channels only) to increase total processing throughput. All histogramming blocks work in parallel for a common time period. A histogram data is read by CAR HISTOGRAMS INTEGRATOR block after the measurement time period and finally sent to the BAC board,
- 3. The histogramming data from four CAR boards are received by the BAC HISTOGRAMS INTEGRATOR block on BAC board. Then, the block creates one common vector of histograms data from 256 channels.

The histogram data is sent to an external DDR3 memory (256 MB) via DDR3 MEMORY INTERFACE block. A complete firmware for fast histogramming of charges of the T-GEM detector has been completed for 21 FPGAs. The firmware was prepared as a set of configurable components. Components have been written as VHDL behavioral descriptions form. Firmware has been implemented and running for Spartan-6 FPGA family (Xilinx). The histogramming process was tested by measuring the 5.9 keV photons emitted by 55Fe isotope. The most important histogramming process parameters are presented in the Table:

Parameter name	Unit	Count
Channel number	#	256
Analog signal probe frequency	MHz	77.78
Digital signal size	bits	10
Strip charge data size	bits	15
Cluster charge data size	bits	17
Histogramming data size	bits	9
Maximum histogramming charge levels	#	512
Histogramming counting size	bits	16
Minimum histogramming time	S	0.01
Maximum histogramming time	S	14000
Maximum histogram measures (for 512 charge levels)	#	2000
Maximum histogram measures (for 256 charge levels)	#	4000
Maximum histogram measures (for 128 charge levels)	#	8000

The fast histogramming of charges from the T-GEM detector was used both in the diagnosis of the T-GEM detector as well as measurements of soft X-ray radiation emitted by JET tokamak plasma [9] for 10 ms time resolution and for 20-40 s of total measurement time period.

Achieved results

During year 2013 the system interface, based on MATLAB package was carefully developed to accomplish control, communication, data processing and imaging results. This tool allows one to study properties of the detector, measuring system diagnostics, optimization of working conditions and system development. The measuring system interface is of fundamental importance for the interpretation of the survey data and their preparation for the KX1 diagnostics. MATLAB interface is an integrated module that provides software control of the measuring process and the acquisition and processing of data. Efficient use of these

possibilities requires a conscious attitude and knowledge of the complex structure of functions and its parameters available in the service control panel.

Within this interface it was prepared also the algorithm for precise different diffraction orders separation for the following offline analysis of the data, calibration procedure (Fig. 2) and other necessary functionalities for diagnostics of the electronics and detector parameters.

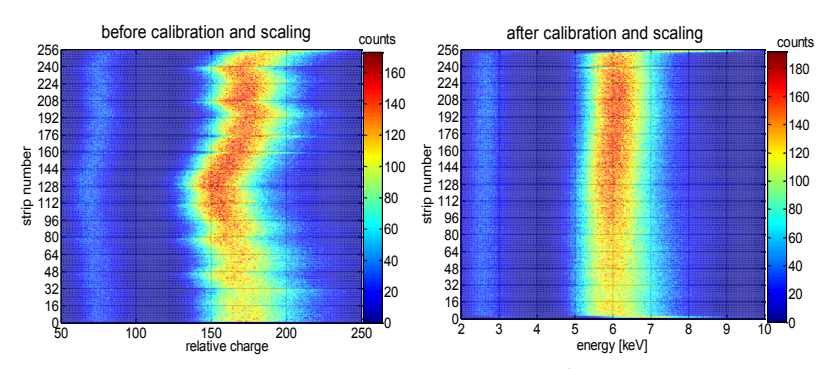


Fig. 2. Characteristics for 256 channels before and after calibration/scaling procedure. features of software for calibration and were prepared.

The recent tests of the system with high power plasma revealed the charge gain slewing and the response parameters inertia of the order of 100 ms due to the sudden elevated flux of X-rays. It had been verified that the issue was mostly related to the current limitation in the HV voltage divider and the power supply circuit. Optimization of the HV scheme was then essential to achieve stable energy resolution of the detectors. Good and rate independent energy resolution is crucial for the W⁴⁶⁺ system, as the first order of diffraction overlaps with the argon escape peak caused by the second order of diffraction. The long term measurements with the high time resolution detection system exposed to high X-ray fluxes was therefore an essential part of the activity. So, during the C31 campaign at JET together with the installation of the detectors the final HV divider was mounted considering protection against sparking. Final distribution of voltages was implemented after optimization of HV supply circuit in order to stabilize the gain dependence of the detectors under the high rate radiation and to enhance energy resolution of the detector. This distribution was obtained and verified in the laboratory using 12-channel HV supply. Currently, the divider distributes the applied HV (for the example 5575 V) between the detector elements as follows:

Detector elermens	Resistirs		
Induction gap	4.3 ΜΩ	HV1	985.7113
GEM 1	1.5 ΜΩ	HV2	343.8528
Transfer gap 1	3.3 ΜΩ	HV3	756.4762
GEM 2	1.65 ΜΩ	HV4	378.2381
Transfer gap 2	3.3 ΜΩ	HV5	756.4762
GEM 3	1.8 ΜΩ	HV6	412.6234
Drift gap	8.47 MΩ	HV8	1941.622
Total Resistanc	24.32 ΜΩ		
Total voltage		5575 V	

The main aim of the high-resolution X-ray detection system is to measure high-resolution X-ray spectra originating from the characteristic emission lines of impurities present in tokamak plasma and to provide monitoring of this characteristic radiation. The X-ray diffraction pattern of atomic emission is superimposed with the continuum X-rays distributions in the detection plane due to different diffraction orders of the crystal. The energy resolved imaging technique is necessary to extract the information about impurities' concentration with high sensitivity. Information from all spectral orders of diffraction (bremsstrahlung radiation) should allow better estimation of the plasma state.

In order to check the capability of the developed GEM detectors to measure higher energy photons a series of measurements was performed. Tests were done using the prototype detector at IPPLM with 96 available read-out channels. Mini-X with Ag target based on the Newton Scientific Inc. miniature X-ray source was used for these tests. The working voltage was up to 30 kV with 3 uA current with irradiating time of about 5 s. Before and after the main measurement with different secondary targets ⁵⁵Fe spectrum was taken for energy scaling. In Fig. 4 we present the results of measured fluorescence lines from Cu and Pb materials.

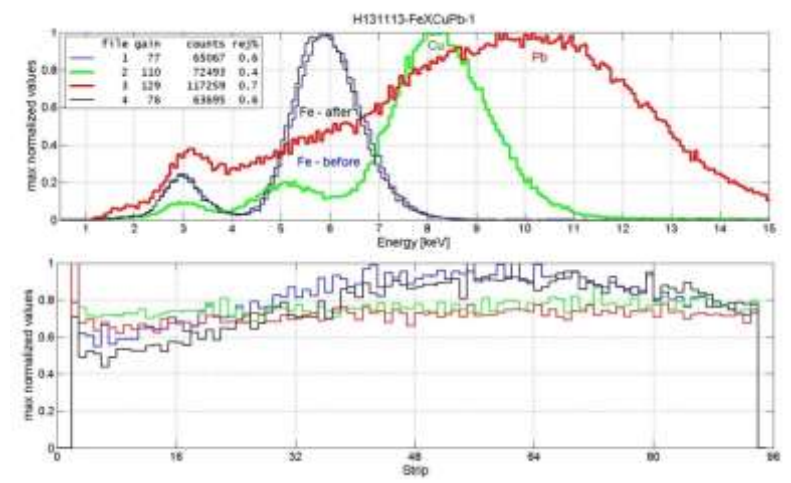


Fig. 4. Energy and position distribution of incoming photons intensity for ⁵⁵Fe source and Cu, Pb fluorescence lines.

It is clearly seen from the shown spectra that the GEM detectors designed and constructed in the frame of this project provide the measurement for photon energy much higher than the third diffraction order sufficient to measure the energies higher enough to detect the second and third diffraction orders of both crystals at JET X-ray spectrometer.

Conclusions

Two Triple-GEM detectors with 206x92 mm² detection area and 256 channels each were developed and constructed for high-resolution X-ray measurements of spectra originating from the mid- and high-Z impurities in tokamak plasmas. The electronics using the modern standards of signal processing and signal transmission based on the firmware configured FPGA technique allows an online measurement of energies and impact position of individual photons at high fluxes. Two detecting units provide energy resolved fast dynamic plasma radiation imaging in the SXR with 100 Hz frequency corresponding to 10 ms time of periodic exposures. Detectors were dedicated and optimized for continuous monitoring of plasma radiation emitted by highly ionized metal impurities present at JET tokamak, W46+ (at ~2.4 keV) and Ni²⁶⁺ (at ~7.8 keV) with good energy and position resolution. High counting rate capability of the detecting units has been achieved with good position resolution. The detection systems operate in the data flow mode providing energy and position measurement of incoming photons with sufficient precision - the energy resolution of about 23% and detection spatial resolution of 0.8 mm obtained at the typical operating conditions of the JET tokamak. Due to good energy resolution and high stability of operation at high radiation fluxes, the on-line separation of diffractive patterns corresponding to the first three spectral orders of the crystal diffraction was achieved. The capability of pipelined processing electronics unit assured efficient measurements of photon flux during the plasma discharges, photon position and energy, in time-slices as short as 10 ms within 20 s of total measurement time. The innovative and fast algorithm implemented in FPGAs circuit enables additional corrections of the detector gain during off-line analysis thus providing very accurate separation of diffraction lines, what improves the physical data quality.

Collaboration

Warsaw University of Technology, Institute of Electronic Systems, Warsaw, Poland;

K. Pozniak, G. Kasprowicz, W. Zabolotny

Warsaw University, Faculty of Physics, Institute of Experimental Physics, Warsaw, Poland;

W. Dominik

Institute of Nuclear Physics, Polish Academy of Sciences, Cracow, Poland

M. Scholz

Association EURATOM - CCFE, Culham, United Kingdom.

References

- [1] K.W. Hill et al., A spatially resolving x-ray crystal spectrometer for measurement of ion-temperature and rotation-velocity profiles on the Alcator C-Mod tokamak, Rev. Sci. Instrum. 79, 10E320 (2008).
- [2] K.-D. Zastrow et al., Deduction of central plasma parameters from line-of-sight averaged spectroscopic observations, J. Appl. Phys. 70, 6732 (1991).
- [3] F. Sauli, Development and applications of gas electron multiplier detectors, Nucl. Instr. and Meth. in Phys. Res. A 505, 195 (2003).
- [4] C. Altunbas et al., Construction, test and commissioning of the triple-gem tracking detector for compass, Nucl. Instr. and Meth. in Phys. Res. A 490, 177 (2002).
- [5] R. Bartiromo, F. Bombarda, R. Giannella, S. Mantovani, L. Panaccione, and G. Pizzicaroli, JET high resolution bent crystal spectrometer, Rev. Sci. Instrum. 60, 237 (1989).
- [6] Jakubowska K., et al., "Development of a 1D Triple GEM X-ray detector for a high-resolution X-ray diagnostics at JET" Proc. 38th European Physical Society Conference on Plasma Physics, P2.036 (2011).
- [7] Zabolotny W.M., et al, "Optimization of FPGA processing of GEM detector signal" Proc. SPIE 8008, 80080F (2011).
- [8] Pozniak K., "Modeling of synchronous data streams processing in the RPC muon trigger system of the CMS experiment" International Journal of Electronics and Telecommunications, 56 (4), 489-502 (2010).
- [9] Chernyshova M., et al., "Development of GEM gas detectors for X-ray crystal spectrometry" Proc. 3rd Conference on Micro-Pattern Gaseous Detectors, poster session (2013).

Development of new MHD diagnostic: GEM gas detector for Soft X-ray measurement

Principal investigator:

M. Chernyshova; <u>maryna.chernyshova@ipplm.pl</u>
Collaborators from the Institute of Plasma Physics and Laser Microfusion:
T. Czarski, K. Jakubowska, G. Kasprowicz, J. Rzadkiewicz, A. Ziółkowski

Introduction

Measuring Soft X-Ray (SXR) radiation of magnetic fusion plasmas is a very useful tool that provides valuable information on particle transport and magnetic configuration. For new generation tokamak one of the main operational difficulties in metallic interior wall and divertor is the interplay between particle transport and MHD activity which might lead to impurities accumulation and finally to

disruption [1]. Studying such phenomena requires a new SXR diagnostic that can provide energy dependent information on the SXR radiation intensity.

Here we present works concerning the development of the GEM SXR detection system based on the multi-channel measurements and essential data processing necessary for soft X-ray energy and position recognition. The tokamak SXR tomography with a new type of detection system that works in photon counting mode offers some unique advantages in comparison with system using so far: cheap, compact, good spatial and temporal resolution, energy discrimination capabilities and has the particularity to be neutron resilient. This makes it a potential good candidate for SXR measurement also in ITER or DEMO.

The 10x10 cm² GEM detector dedicated for direct tokamak plasma imaging has been constructed with the innovative FPGA data acquisition system. The acquisition system has been partially optimized by means of the preliminary laboratory tests. In addition a reduction of the gain in a high counting rate regime has been observed. So far, the constructed GEM detector is able to image the plasma without energetic thresholds with performances of ~10 ms time resolution and ~800 ②m space resolution, respectively. In order to implement the energetic thresholds in the imaging of the plasma a dependence between the gain and counts rates in GEM detector has been be studied.

A further development of the detection system has been planned for nearest years. The read-out system will be optimized in order to improve the data processing and the time resolution below 10 ms and space resolution below 800 2m. A new more powerful FPGA firmware will be implemented.

Experimental Results

In order to implement the energetic thresholds (discrimination) in the SXR diagnostic the crucial point is a knowledge of gain and counts rates dependence. Such dependence were studied in this project for x-ray GEM detectors. In these studies we used 55Fe radioactive source and x-ray tube. An example of such measurement is shown an Fig. 1 where one can see the energy (charge) and position distributions.

A dependence between the gain and counts rates in GEM detector have been studied in stable HV of detector and atmospheric pressure by increase the current (intensity of radiation) of the x-ray tube up to 100 uA. All operational conditions (HV applied to GEM detector, pressure and x-ray tube current) are presented in Fig. 2. Fig. 3. presents the energy (charge) distribution measured for X-ray tube at different counting rates. It was found a significant reduction of the gain in a high counting rate regime.

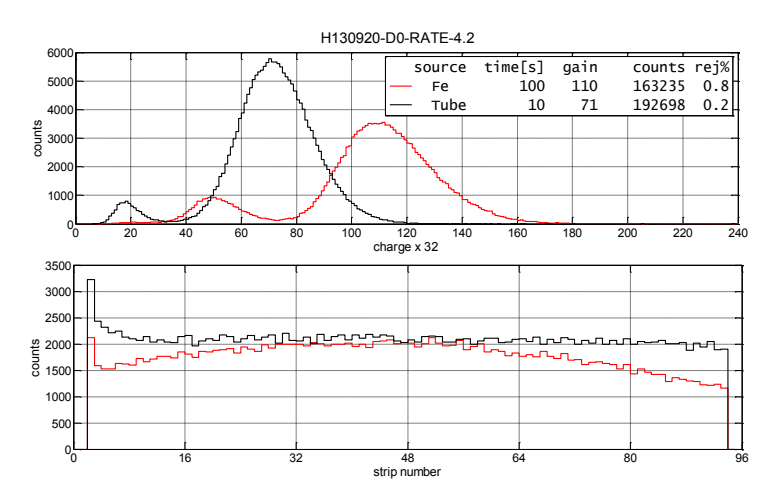


Fig. 1. The energy (charge) and position distribution measured for Fe & X-ray tube [4.2 kV, 1 uA].

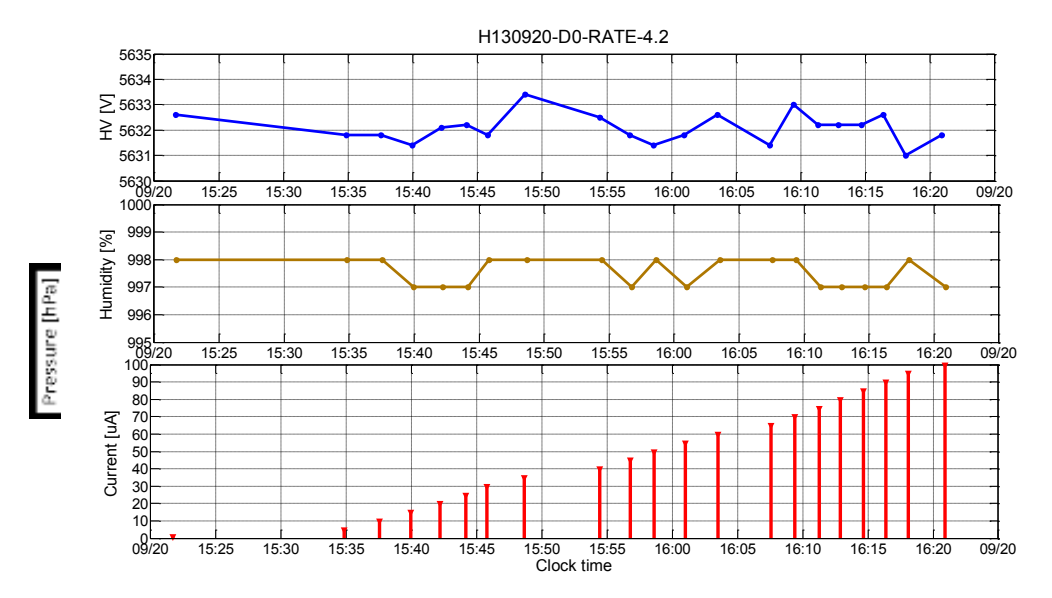


Fig. 2. Operational conditions (HV applied to GEM detector, pressure and x-ray tube current).

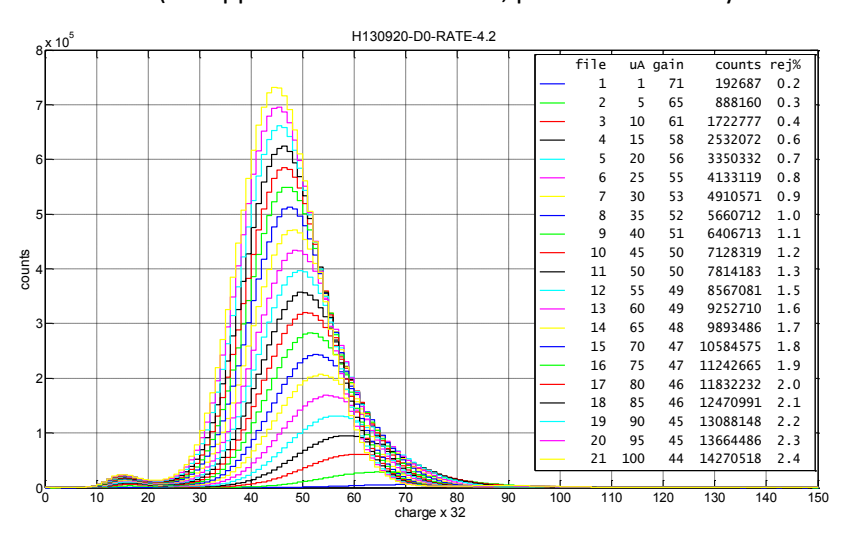


Fig. 3. The energy (charge) distribution measured for X-ray tube at different counting rates.

For the final prototype detector, the electronics processing unit with 128 readout channels was optimized in order to in order to mitigate this problem. In particular, the readout system that consists of FPGA circuits was optimized. The system controls AFE boards and analogue-to-digital converters (ADC), receive the data, preprocess them, detecting hits and estimating their energy and position, time-stamp the data using the external synchronization signal and store results in the DDR memory. During the prototype phase first establishments of electronic configuration were verified, tested and improved as required. A radiation source and PC with Matlab on board have been used for hardware verification and preliminary development of measurement algorithms to be implemented in the FPGA module. The AFE channel bandwidth was chosen to match timing characteristics of the primary pulse and 77.7 MHz sampling rate of digitization in the 10 bit ADCs was established. Dedicated algorithm of cluster identification and cluster charge integration were developed and implemented in the readout unit for precise energy reconstruction. In this way, the main aim of the project was achieved.

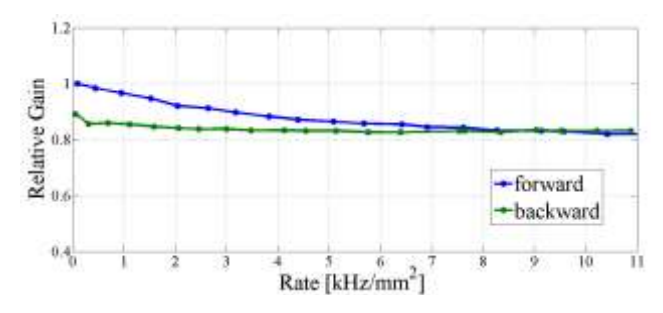


Fig. 4. Charge gain and rejected events vs. strip rates (taken from [2]).

After detector and electronics optimization the final prototype detector performances were determined (see Fig. 4). At this stage of the system development one can see that the charge gain sensitivity on the photo flux was reduced to about 10% for rates exceeding 10 kHz/mm2 in GEM detector. This capability should assure efficient measurements of high photon flux during the plasma discharges, photon position and energy, in time-slices as short as 10 ms within tens of seconds of total measurement time. The innovative and fast algorithm implemented in FPGAs circuit enables additional corrections of the detector gain during off-line analysis thus providing good separation of different x-ray energy ranges.

References

- [1] D. Mazon et al., Proc. 40th EPS Conf. on Plasma Physics (2013) P6.011.
- [2] M. Chernyshova et al., submitted to JINST.

Collaboration

Warsaw University of Technology, Institute of Electronic Systems, Warsaw, Poland;

K. Pozniak, G. Kasprowicz, W. Zabolotny

Warsaw University, Faculty of Physics, Institute of Experimental Physics, Warsaw, Poland;

W. Dominik

Institute of Nuclear Physics, Polish Academy of Sciences, Cracow, Poland

M. Scholz

Association EURATOM - CCFE, Culham, United Kingdom.

Feasibility studies of hard X-ray technique for the future HXR monitor - Characterization of Scintillation Materials for Tokamak Plasma Diagnostics

Principal investigator:

J. Rzadkiewicz; <u>jacek.rzadkiewicz@ipplm.pl</u>
Institute of Plasma Physics and Laser Microfusion
National Centre for Nuclear Research, Otwock-Świerk, 05-400 Poland
EURATOM/CCFE Association, Culham Science Centre, Abingdon, UK.

Introduction

The ideal detector for hard X- and γ -ray diagnostics of tokamak plasmas should be characterized by the fast response to the incident radiation, that is especially important for DT experiments with expected high counting rates up to a few MHz. Such fast response allows one to reduce the acquisition system

dead-time and record more pile-up free information. Another important parameter of the spectrometer is energy resolution, which depends on properties of the detector material connected with proportionality of the output signal to the absorbed incident radiation energy. The next decisive parameter is photon detection efficiency. Materials with high densities and high atomic numbers are preferable because the detection efficiency depends on density and atomic numbers of the detector material. In addition, all detector properties should be stable during operation in the harsh tokamak environment, at a high temperature and in a strong magnetic field (~2 T). And at last, the detectors should be highly resistant to intensive neutron fluxes.

Two types of scintillation detectors, the CsI:Tl and LaBr3:Ce, which are currently used on JET in hard X-ray/γ-ray diagnostic systems, were characterized in the first place [1] Finally, CeBr3, NaI:Tl and GAGG:Ce (gadolinium aluminum gallium garnet – structural notation of Gd3Al2Ga3O12:1%Ce) scintillators were studied. The following quantities for each tested scintillator were measured under the same experimental conditions: light output, energy resolution, non-proportionality of the light output as a function of x-ray energy, decay time of the light pulse, full energy peak detection efficiency of x-rays. On the basis of obtained results, a recommendation of scintillating material, suitable for the hard-X/gamma-ray tokamak diagnostics, will be given.

Experimental Details

A comparative study of all tested scintillator samples was done under the same experimental conditions. The crystals had the cuboid shape with a size of 10x10x5 mm3, comparable with those used at JET. Due to the hygroscopic nature the NaI:Tl, LaBr3:Ce and CeBr3 crystals were assembled by the manufacturers in the aluminum cans with glass windows, whereas non-encapsulated CsI:Tl and GAGG:Ce crystals were coated by Teflon tape to increase the amount of light collected by a photodetector. Each crystal was coupled to a photomultiplier (PMT) with silicone grease to improve the optical contact with the photodetector window. A Photonis XP5212 and a Hamamatsu R6231-100 photomultipliers (PMTs) were used to measure the scintillator properties. Due to the fact that the XP5212 PMT was precisely calibrated in terms of its quantum efficiency (QE) and we verified the correctness of a relation between response to single photoelectron and scintillation pulse, we used it for light output characterization to ensure high accuracy of measurements [2].

Results

For the light output measurements, a 137Cs encapsulated source emitting 661.7 keV $\ 2$ -rays, was used to irradiate scintillators. For each crystal the number of photoelectrons per energy unit was determined by comparing the measured 661.7 keV γ -ray absorption peak to the single photoelectron peak. The light output was measured for the optimal shaping time – i.e. the extending of the pulse integration time did not result in an increasing number of registered photoelectrons. It is requires to have a number of detected photoelectrons as high as possible because a photoelectron statistics is one of the crucial factors limiting the measured energy resolution.

The obtained light output values for LaBr3:Ce, CeBr3 and CsI:Tl are in a good agreement with previously measured data. For the GAGG:Ce scintillator, which after an annealing process, the measured light output is higher by about 50% in comparison with results presented in Refs. [3]. For the tested NaI:Tl sample an exceptionally high light output was also registered. This value is about 50% larger than that reported in Ref. 11. However, these results do not affect an improvement of the energy resolution for both GAGG:Ce and NaI:Tl scintillators. Tests of few other NaI:Tl crystals with different dimensions, performed in the same conditions, showed light outputs comparable to that reported in Ref. 11.

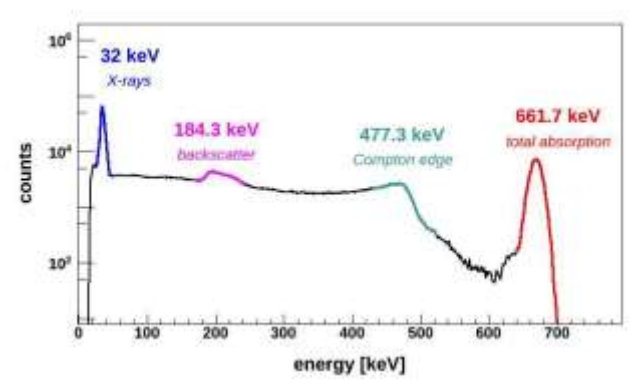


Fig. 1. Energy spectrum of 661.7 keV X rays from a 137Cs source measured with the LaBr3:Ce scintillator.

As an example, in FIG. 1 the 137Cs energy spectrum recorded with the LaBr3:Ce scintillator is shown. The full energy peak (total absorption peak) appears at 661.7 keV. If the photon is not absorbed, it deposits a part of its energy in a Compton continuum, with a Compton edge equal to 6 477.3 keV. Because γ -rays are scattered in a backward direction, the backscatter peak is also noticeable at 184.3 keV. In the low energy range we notice an absorption peak of 32 keV KX-rays emitted by the 137Cs source. The energy resolution was determined by fitting the absorption peak with Gaussian function to obtain its full-width-at-half-maximum (FWHM). The best performance offers the LaBr3:Ce scintillator with the energy resolution equal to 10.8 % at 59.5 keV and 2.9 % at 661.7 keV. This is the result of its high luminosity (light output), good matching of its emission spectrum with the PMT QE (high photoelectron yield) and good linearity of γ -ray response, which will be pointed out in the next subsection. In the low energy range, CsI:Tl and NaI:Tl show similar performance to LaBr3:Ce. This is also related to their non-proportionality characteristics, which is discussed in the next subsection.

Relaxation of the light emission in scintillators produced by incident photon is characterized by a decay time parameter. Usually, the scintillation decay time varies between nanoseconds and microseconds. Some scintillators show more than one decay mode - as rule for inorganic scintillators more than one decay mode is observed, e.g., for CsI:Tl and GAGG:Ce [3]. The pulse shapes of the tested scintillators are shown in FIG. 2, scaled at the time 9 stamp of zero. Each crystal was irradiated with the same 137Cs source. The fastest response is observed for LaBr3:Ce and CeBr3 scintillators. This fact promotes both materials as good candidates for high flux measurements in big tokamaks, especially in D-T experiments. The response of GAGG:Ce and NaI:Tl is one order of magnitude slower, however the decay time is still moderate. A long decay time for the CsI:Tl, with two intense slow components of 3100 ns and 13600 ns, makes this crystal less useful for tokamak plasma diagnostics, where high fluxes of X- and γ -rays are expected and large amount of pile-ups could occur.

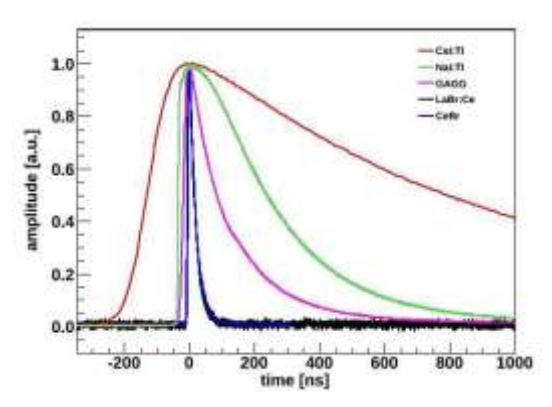


Fig. 2. Pulse shapes of the tested scintillators.

The efficiency of the full energy peak (total absorption peak) or photopeak (since the main contribution to the peak is provided by photoelectrons) was measured for $\ 2$ -rays with energies from 22 up to 1408 keV. In Fig. 3 the detection efficiency distributions are shown. To highlight the differences in the photopeak detection efficiency for higher energies, the dependence is also shown in the inset in a double logarithmic scale.

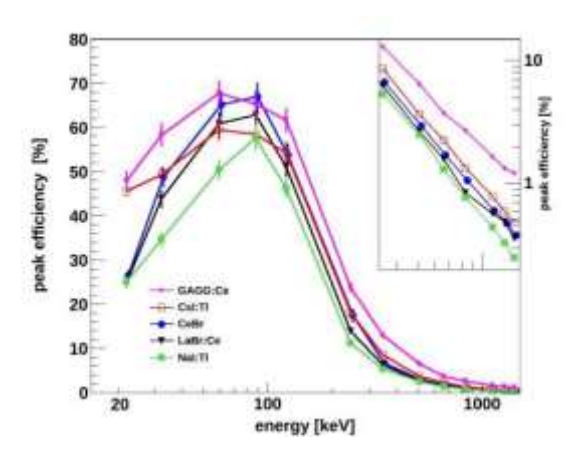


Fig. 3. The full energy peak efficiency measured for ①-ray with energies from 22 to 1408 keV. In the inset, the dependence for higher energies is shown in a double logarithmic scale. The GAGG:Ce sample has the highest detection efficiency from all tested scintillator crystals. At the highest measured energy equal to 1408 keV, the GAGG:Ce is almost one order of magnitude more efficient than NaI:Tl and about five times more efficient than LaBr3:Ce and CeBr3 scintillators of the same size. This is due to the higher density of GAGG:Ce in comparison with other tested materials.

Conclusions

A study of a light output, an energy resolution, a non-proportionality, a decay time and aphotopeak efficiency for 10×10×5 mm3 cuboid scintillators was performed. The properties of all tested scintillators are summarized as follows: The CsI:Tl is characterized by a high light output and a reasonable full energy peak efficiency. In case of CsI:Tl, three decay components were measured. The fastest and the most intense decay component is 780 ns, significantly longer than that observed in other scintillation materials. Definitely, such a long response time limits the detection capability in case of highrate tokamak measurements. The NaI:TI scintillator is significantly faster than CsI:TI with a similar light output. It is a relatively low-cost material, however, it shows the worst energy resolution and the lowest full energy peak efficiency from all investigated scintillators. Thus, the NaI:TI scintillator is not a good solution for y-ray monitoring in tokamaks. The GAGG:Ce has an energy resolution comparable to that obtained with CsI:Tl. Similarly, due to emission spectrum peaked at 550 nm, it has a low photoelectron yield when coupled to the PMT, resulting in worsening of the measured energy resolution. As the consequence of the highest non-proportionality, the poorest energy resolution in the low energy range was observed. The GAGG:Ce shows two components of decay time: the fast 12 one equal to 140 ns and the slow one of 570 ns, so it is faster than NaI:TI. It also shows the best full energy peak efficiency from all scintillators presented in this paper. The fastest decay time (~20 ns) was obtained for LaBr3:Ce and CeBr3 what favours these two materials. Both scintillators have a similar high light output. We also notice a progress concerning a development of the GAGG:Ce. This material performs significantly better when coupled to a Si-based photodetector17,18, taking advantage of a high quantum efficiency of the Si for green light. It is also important to emphasize that GAGG:Ce scintillator contains gadolinium and oxygen that requires a neutron shielding by an efficient moderator, like 6LiH, to reduce the neutron induced background. In addition, the gamma spectrum could be distorted due to the electron conversion in gadolinium19. Thus, further measurements should be done to consider the GAGG:Ce as a candidate for hard X-ray/γ-ray tokamak diagnostics.

Collaboration

National Centre for Nuclear Research, Otwock-Świerk, 05-400 Poland

- P. Sibczynski, A. Gójska, V.G. Kiptily, S. Korolczuk, M. Moszyński, A. Syntfeld-Każuch,
- L. Swiderski,

EURATOM/CCFE Association, Culham Science Centre, Abingdon, UK.

References

- [1] M. Nocente et al., IEEE Trans. Nucl. Sci. 60, 1408-1415 (2013).
- [2] M. Moszyński, et al., IEEE Trans. Nucl. Sci. 57, 2886-2896 (2010).
- [3] J.Iwanowska, et al., Nucl. Instrum. Meth. A712, 34-40 (2013).

Development of plasma imaging technology in X-ray range for the purposes of diagnostics monitoring impurities released from the walls of a fusion reactor

Principal investigator:

M. Chernyshova; <u>maryna.chernyshova@ipplm.pl</u>
Collaborators from the Institute of Plasma Physics and Laser Microfusion:
T. Czarski, S. Jabłoński

Introduction

Measuring Soft X-Ray (SXR) radiation (0.1-20 keV) of magnetic fusion plasmas is a standard way of accessing valuable information on particle transport and magnetic configuration. The proposed project refers to development of technology suitable for plasma imaging in the soft X-ray region devoted for monitoring of impurities radiation. Since recently the metallic walls have been installed on many machines and a new problem occurs with the impurities which are released from the wall (W in particular), it is highly desirable, then, to understand the impact of the plasma contamination and its effects on plasma scenarios. As such impurities could cause radiative collapses and often disruption one needs to develop a new diagnostic to be able to reconstruct the impurity distribution. For this purpose a SXR imaging diagnostic with energy discrimination is a very good candidate [1].

Methods and results of research

Under this subject GEM detector technology was chosen for constructing the model detector for plasma imaging, which provides measurements of SXR spectra by new generation energy-resolved micropattern gas detectors with 2D position reconstruction capability. The prototype detector has dimensions of the active window $10x10cm^2$. The detector consists of a three-stage cascade system of the GEM electrodes separated by 2 mm transfer gap. A dedicated sensitive working volume of the detector is enclosed on the one side by the 2 mm thick PCB plate with deposited anode plane of different structures. The results we present in this work concern the readout channels in the shape of hexagons with 3.9 mm leg.

In current tokamak systems where information of radiation from the impurities in plasma is required, such monitoring will need the on-line data analysis, when a large number of pixels, resulting from the need for good spatial resolution, leads to a large amount of the processed signals from the detector.

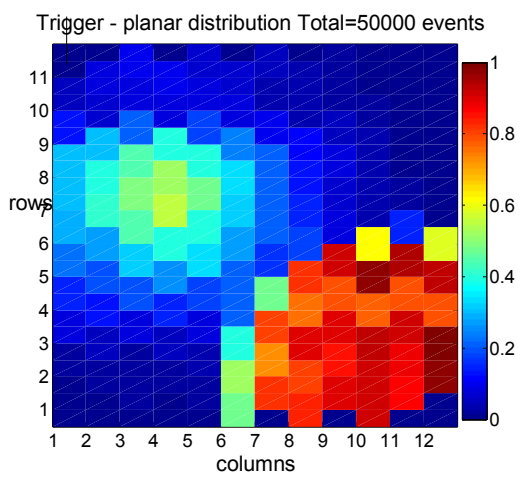


Fig. 1. Planar distribution of two SXR sources intensities (⁵⁵Fe placed near the detector window and X-ray generator at about 3keV irradiating detector surface 10 cm away from it through 7 cm collimator).

All these requirements put a very high level for standards of electronic part both hardware and data processing module handling signals from all channels - clustering, positioning and energy estimation. The main elements of the proposed state-of-art electronics, being under activation and verification at the present stage, are: Analogue Front End (AFE) boards carrying integrating charge amplifiers, calibrating blocks, analogue integrators and ADCs with 16 active channels; FPGA Backplane boards processing data from 4 AFE boards and communicating among themselves and controller by gigabit serial links with a transfer rate of 20Gbit/s; FMC module providing communication between FPGA backplane boards and controller module; the controller module based on PCIe Gen3 switch, FPGA module and series of links; dedicated 7-channel HV supply unit and 16-core DSP modules ensuring real time signals processing preliminarily handling in FPGA front-end modules.

Currently the simplicity of the hexagonal type of the readout architecture with the positioning accuracy of one pixel was chosen to establish a base for more complicated 2D readout structures. For this case, the majority of events (photon absorption) happen with one pixel cluster size, which allows introduction of simple algorithms for energy and position determination. In Fig. 1 we show planar distribution of two SXR sources intensities (⁵⁵Fe and X-ray generator at about 3keV) obtained by the planar distribution of trigger signals which reflects the intensity distribution of dominant cluster charge. It is a direct way to identify the position of the cluster and thus position of photon absorption.

Conclusion

Summarizing the laboratory tests it can be concluded that a simplified algorithm can be used for the tested hexagons structures with 3.9 mm leg length to identify the position and energy of the absorbed photon. Such a structure could find its application for tokamak plasma imaging in the field of X-ray radiation in online mode with high temporal resolution (1-10 ms) at the cost of less accurate estimation of energy and position of photons. The development of measurement tools for reading the first selected architecture formed the basis for the verification of the remaining designed and manufactured readout structures to select the appropriate architecture for final imaging the tokamak plasma.

Acknowledgements

The research was performed in the framework of task No5 of the research project realized under the contract No. SP/J/2/143234/11 between NCBiR and IFPiLM, Poland.

Collaboration

University of Warsaw, Warsaw, Poland.

W. Dominik.

Warsaw University of Technology, Warsaw, Poland.

K. Poźniak, G. Kasprowicz,

References

[1] F. Sauli, Nuclear Instruments and Methods in Phys. Res A 386 531 (1997).

The activation meaurements in support of the JET neutron calibration

Principal investigator:

R. Prokopowicz; <u>rafal.prokopowicz@ipplm.pl</u>

Collaborators from the Institute of Plasma Physics and Laser Microfusion:

B. Bieńkowska, S. Jednoróg,

Introduction

The JET neutron diagnostics calibration has been performed in April 2013. The neutron diagnostics need to be calibrated very carefully, because they are essential to proper determine fusion power and estimate dose rate from activated structure materials. The response function of each neutron detector depends on neutron energy spectrum and, accordingly, on source characteristics and surroundings. In case of JET calibration, the spontaneously-fissile californium source has been used instead of deuterium plasma source of 2.5 MeV neutrons. Therefore, neutron transport calculations strongly supported the calibration. In order to provide proper neutron spectrum at detectors the numerical simulations have been performed by means of the MCNP transport code based on the Monte Carlo method. It takes into account the real position, shape, energy spectrum of the calibration source and influences of its environment, such as the vacuum vessel details, MASCOT, boom etc. The neutron activation method has been used as a benchmark for the numerical calculations. The reactions induced in purpose-prepared activation samples by the neutrons from the calibration source enable to compare the results of the simulations with the results obtained using the activation system (KN2). The MCNP model verified during such procedure can be used to calibrate other neutron diagnostics, like the fission chambers (KN1).

Verification of the MCNP model of torus and calibration of the activation system enable to improve the accuracy of neutron calculations and measurements at JET. The calibrated KN2 system can be used to cross-calibrate the KN1 (neutron monitor), KN3 (neutron camera), etc. The neutronic issues relevant to licensing process need to be performed on ITER as well. The experiences acquired during JET neutron calibration will be useful for preparing such action on ITER.

The project is connected with the following present tasks: JW9-FT-5.32, JW10-FT-5.34, and with tasks in the frame of Neutronic Calculations supporting the JET Neutron Calibrations proposed by MHEST, VR and CCFE Associations.

The goal of the task was to perform the activation measurements in order to calibrate the KN2 system for a number of reactions and, therefore, verify the detailed MCNP model of JET. The aim of the task was to perform the multi-element activation measurements during JET neutron calibration. The measurements carried out by means of the KN2 system utilizing purpose-prepared activation samples allow to record a number of nuclear reactions induced by the neutrons coming from calibration source. A modern, pre-calibrated HPGe gamma-spectrometer belonging to IPPLM, has been used to estimate activity of irradiated samples. The experimental data collected in such way allow determination of the activation coefficients for recorded reactions. The measured coefficients will be compared with the coefficients calculated by the MCNP code.

Neutron calculation validation

The measured activity of products of reactions induced by neutrons from a well-known calibration source inside tokamak allow to obtain nuclear reaction rate \mathbb{Z}_m as follow

$$\alpha_m = \frac{A}{N_a \cdot \left(1 - e^{-\lambda \cdot t_r}\right)}$$

where A — measured activity of reaction product, t_r — irradiation time, \mathbb{Z} - reaction product decay constant, N_a — number of target nuclei.

It is possible to calculate the same reaction rate by means of neutron transport code (MCNP) by implementation of the calibration source inside tested model

$$\alpha_c = \int_0^\infty \sigma(E) \ \varphi(E) \ dE$$

where $\mathbb{Z}(E)$ — reaction microscopic cross-section, $\mathbb{Z}(E)$ — calculated neutron energy spectrum. If the measured (\mathbb{Z}_m) and the calculated (\mathbb{Z}_c) reaction rates agree, within the total combined uncertainties, then we can trust the numerical model.

Selection of activation reactions

The following materials have been selected for neutron activation measurements during the JET calibration by means of a Cf-252 source: In, Au, Mn, W, Ta, Sc, Fe, Ni, Al. Activation samples consisting of above mentioned materials have been prepared in KN2-standard size (18 mm in diameter): In, Au, W, Ta, Fe, Ni, Al, (2 mm thick), Mn (1 mm thick), Sc (1.25 mm thick). Appropriate MCNP calculations allow us to assess the activity of the activation samples after 3-hours irradiation by 5·10⁸-yield Cf-source, 30 cm below 3-Upper irradiation end of JET KN2 system. The relevant nuclear data are shown in see Tab. 1.

Table 1. Reactions recommended for Cf-252 neutrons measurement from [1] and activities of the samples (\emptyset 18 mm, 1 mm-thick) after 3-hours irradiation by $5\cdot10^8$ -yield Cf-source, 30 cm below 3U IE.

Reaction	Threshold [MeV]	T ½	Activity [Bq]	E2 [keV(%)]
Al-27 (n,p) Mg-27	4	9.5 m	2E+0	844 (72), 1014 (28)
Al-27 (n,a) Na-24	7	15 h	6E-2	1369(100), 2754(100)
Sc-45 (n,g) Sc-46	-	84 d	6E-2	889 (100), 1121 (100)
Ti-46 (n,p) Sc-46	4	84 d	5E-4	889 (100), 1121 (100)
Ti-47 (n,p) Sc-47	2	3.3 d	2E-2	159 (<i>68</i>)
Mn-55 (n,g) Mn-56	-	2.6 h	6E+1	847 (99), 1810 (27)
Fe-54 (n,p) Mn-54	2	312 d	1E-3	835 (100)
Fe-56 (n,p) Mn-56	5	2.6 h	5E-1	847 (99), 1810 (27)
Co-59 (n,g) Co-60	-	5.27 y	3E-2	1173 (100), 1332 (100)
Co-59 (n,p) Fe-59	4	44.5 d	2E-3	1099 (57), 1292 (43)

Ni-58 (n,p) Co-58	2	71 d	7E-2	811 (99)
Ni-60 (n,p) Co-60	5	5.27 y	2E-5	1173 (100), 1332 (100)
Ag-109 (n,g) Ag-110	-	250 d	4E-2	885 (<i>73</i>), 937 (<i>34</i>)
In-113 (n,n') In-113m	1	99 m	2E+0	392 (65)
In-115 (n,g) In-116	-	54 m	3E+3	1097 (59), 1294 (85)
In-115 (n,n') In-115m	0.5	4.5 h	2E+1	336 (<i>46</i>)
Ta-181 (n,g) Ta-182	-	114 d	2E-1	100 (14), 1121 (35)
W-186 (n,g) W-187	-	24 h	4E+1	480 (<i>27</i>), 686 (<i>33</i>)
Au-197 (n,g) Au-198	-	2.7 d	2E+2	412 (96)
U-238 (n,g) U-239	-	23.5 m	9E+2	75 (<i>49</i>)

Testing measurements on PF-1000

In order to test the measuring procedure of selected materials the irradiation on the PF-1000 DD fusion neutron source has been foreseen.

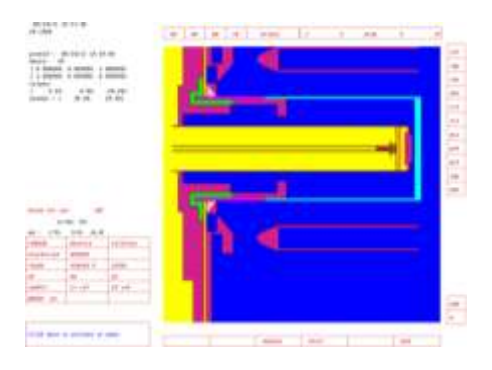


Fig. 1. The MCNP model of PF-1000 device with moderator and irradiated samples.

Prepared activation samples have been irradiated in the neutron field shaped in the following way. For the test irradiation on PF-1000 the following samples have been chosen: Sc, Ta, Mn, W, Au, In. Series of 7 plasma discharges within 2 hours have been performed, which yielded a total neutron production of 1.33E+11 (according to calibrated silver activation counters). The neutron fluence, however, was about 6 times less than expected during 3-hours irradiation by means of Cf-252 source at 30 cm-distance from 3U irradiation end. Besides of that, most of the expected radiative capture reactions have been recorded, unlike the threshold reactions, which mostly have not been recorded due to the difference in fast neutrons spectrum coming from d-d reactions and a Cf-252 source.

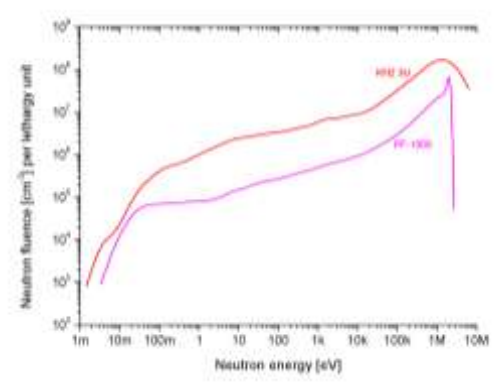


Fig. 2. Neutron energy spectrum from Cf-252 source in 3U IE (red) and in PF-1000 with 1 cm thick polyethylene (magenta). Different colours mark the source type on the curves.

A precalibrated gamma-spectrometer system has been used to determine the sample activities. The system consists of a HPGe Coaxial Detector System, Genie-2000 gamma analysis software, InSpector 2000 multichannel analyzer, Labsocs (Laboratory Efficiency Calibration Software), LabSocs characteristic of the HPGe detector, shielding system.

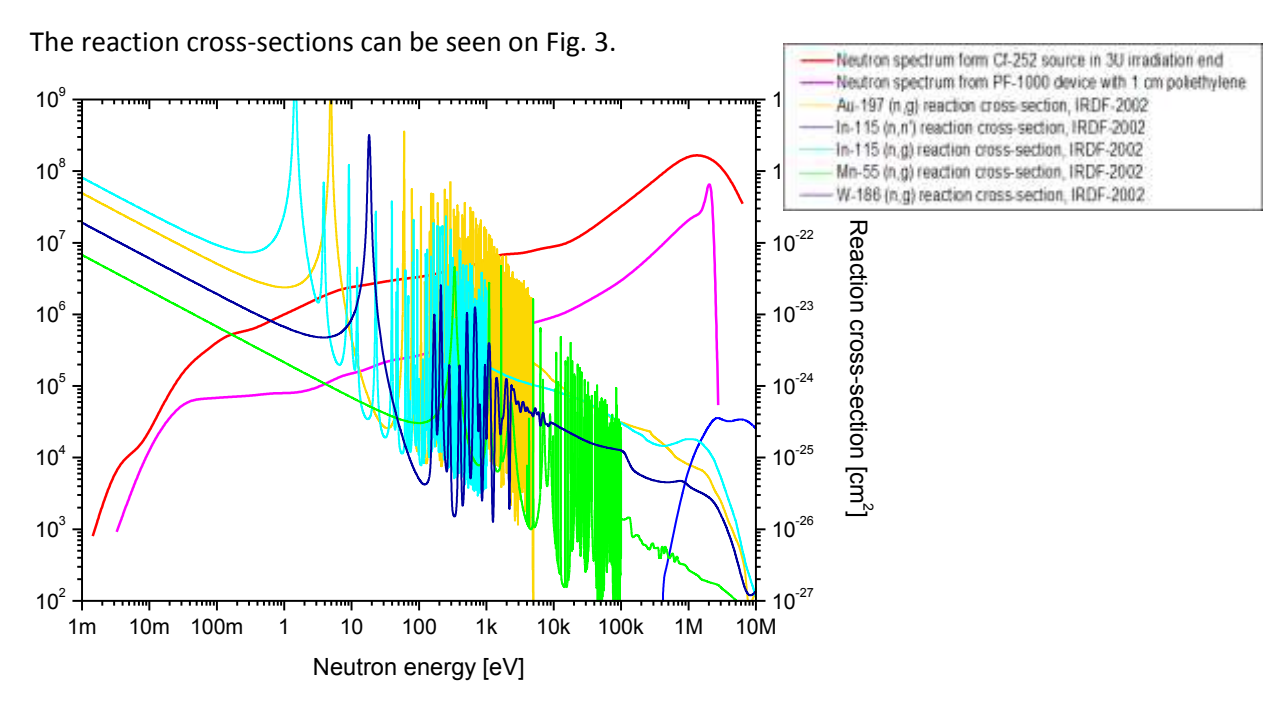


Fig. 3. Cross-section of reactions recorded during experiment on PF-1000 device.

The measured activities and reaction rates are listed in Tab. 2.

Table 2. Reactions recorded during experiment on PF-1000.

Reaction	T ½	Activity [Bq]	Reaction rate [s ⁻¹]
In-115 (n,g) In-116	54 m	62.15 ± 2.21	(10.53 ± 0.38)E-18
In-115 (n,n') In-115m	4.5 h	17.12 ± 1.02	(8.36 ± 0.50)E-18
Au-197 (n,g) Au-198	2.7 d	2.50 ± 0.12	(8.10 ± 0.40)E-18
W-186 (n,g) W-187	24 h	1.06 ± 0.07	(5.21 ± 0.34)E-18
Mn-55 (n,g) Mn-56	2.6 h	6.07 ± 0.51	(1.66 ± 0.14)E-18
In-113 (n,n') In-113m	99 m	0.38 ± 0.76	(1.96 ± 3.90)E-18
Ta-181 (n,g) Ta-182	114 d	<0.1	-
Sc-45 (n,g) Sc-46	84 d	<0.01	-

The values of reaction rates, averaged over 7 discharges, have been calculated in the following way:

$$\overline{\alpha} = \frac{A_0}{\lambda \cdot n_a \cdot \sum_{i=1}^n w_i \cdot e^{-\lambda \cdot t_i}}$$

where A_0 – initial activity, λ – decay constant, n_a – number of target nuclei, w_i – weight of i-th shot, t_i – time from i-th shot.

The activation coefficients calculated for recorded reactions, using the spectrum shown in Fig.2, allow for determining total neutron yield as well (see Tab. 3); the activation coefficient uncertainties refer to numerical uncertainties only; the neutron yield uncertainties come from both activation coefficient uncertainties and activity measurement uncertainties.

Reaction	Activation coefficient (MCNP)	Measured total neutron	
		yield	
In-115 (n,g) In-116	(7.21 ± 0.02)E-29	(1.46 ± 0.06)E11	
In-115 (n,n') In-115m	(1.53 ± 0.03)E-28	(0.55 ± 0.04)E11	
Au-197 (n,g) Au-198	(1.38 ± 0.02)E-28	(0.59 ± 0.04)E11	
W-186 (n,g) W-187	(1.24 ± 0.05)E-28	(0.42 ± 0.05)E11	
Mn-55 (n,g) Mn-56	(1.28 ± 0.03)E-29	(1.30 ± 0.14)E11	
In-113 (n,n') In-113m	(1.04 ± 0.01)E-28	(0.19 ± 0.37)E11	
Ta-181 (n,g) Ta-182	(8.61 ± 0.65)E-28	-	
Sc-45 (n,g) Sc-46	(7.57 ± 0.14)E-29	-	

Tab. 3. The neutron yield calculated based on the activation coefficients for recorded reactions.

Above mentioned results of neutron yield measurement need to be considered taking into account the appropriateness of applied MCNP model. The device geometry is reconstruct exactly. In spite of that, the plasma (thereby neutron source) geometry and position is reconstruct approximately only. The activation samples have been placed a few cm from plasma pinch. Plasma position uncertainty strongly influences, therefore, the activation coefficients and need further investigations. Anyway, the experiment on PF-1000 device proved that in neutron spectrum similar to target one, measurable activity can be recorded for most radiative capture reactions and threshold reaction (with threshold below 2.5 MeV); exception: Ta-181(n,g), Sc-45(n,g), Ni-58(n,p).

The measurements during JET neutron source calibration

Irradiation of two multi-foil sets has been performed during JET in-vessel Neutron Source Calibration (April 2013). The following samples have been irradiated (putting order from capsule bottom) in the first set: Au, In, Al, Fe, Ni, Mn, Au[Cd], In[Cd] and in the second set: Fe, Ti, Ni, Sc, Ta, W.

The first set included thin foils of Au (100 ½m) and In (127 ½m), 10 mm in diameter. Bare Au and In foils were put in the bottom of the capsule separated by ca. 10 mm thick polyurethane foam to decrease thermal neutron self-shielding. Each one of the other Au and In foils were put inside separate cadmium box with 0.8 mm thick walls. Such thickness allow to cut-off the neutrons with energy below 0.6 eV [2]. Comparison of the activity of Au-198 and In-116 induced in bare and shielded foils allow estimation the relative ratio of thermal to epithermal neutron flux density.

The activities of induced radioactive products of nuclear reactions in In, Au, W, Mn, and Fe samples have been measured immediately after irradiation, by means of modern, precalibrated HPGe gamma spectrometer equipped with LabSOCS software enable accurate determining the measuring efficiency for particular set-up geometry and photon energy.

The activities of Co-58, Sc-46 and Ta-182 have been determined one month after irradiation in a low-background gamma-spectrometry laboratory (IFJ PAN, Kraków, Poland) using low background HPGe gamma spectrometer (manufactured by Ortec, 30% rel. efficiency) shielded by 15 cm of 19th century steel and 3 mm thick layer of copper. Spectrometer was calibrated using purpose-prepared simplified calibration source. The source has a form of paper disc with the diameter as the samples, glued on metal plate. The paper was soaked with 50 μl of solution having certified activity concentration of ¹³⁷Cs (644±6 Bq), dried under IR lamp and again soaked with 50 μl of similar solution of ⁶⁰Co (556±5 Bq). In two nickel plates traces of Co-58 were found (in both) on the level of 59 mBq. Measurement of scandium plate reveal clear small peak at 889 keV leads to activity of 28±9 mBq. The second line of Sc-46 is strongly interfered by background peak of Bi-214 having energy of 1120 keV. However, the activity calculated from 1121 keV peak corrected for 1120 keV leads to a twice higher activity, namely 56±27 mBq. The tantalum plate reveals an order of magnitude higher activities – for four analyzed lines of ¹⁸²Ta the activity vary from 0.35±0.08 Bq to 0.47±0.08 Bq with average of 0.42 Bq.

(S.D.=0.04 Bq). No other products of neutron activation were observed. The rates of recorded nuclear reactions have been calculated based on measured activities (see Tab. 4).

Table 4. Reactions recorded during NSC, their activities and rates.

Reaction	T ½	Sample activity [Bq]	Reaction rate [s ⁻¹]
In-115 (n,☑) In-116	54 m	12 ± 1	(3.6 ± 0.2) E-20
In-115 (n,@) In-116 [Cd]	54 m	10 ± 1	(3.0 ± 0.2) E-20
In-115 (n,n') In-115m	4.5 h	1.2 ± 0.3	(9 ± 2) E-21
Au-197 (n,⊡) Au-198	2.7 d	0.6 ± 0.1	(4.0 ± 0.40) E-21
Au-197 (n,@) Au-198 [Cd]	2.7 d	0.6 ± 0.1	(4.0 ± 0.40) E-21
W-186 (n,@) W-187	24 h	4.4 ± 0.2	(1.2 ± 0.1) E-20
Mn-55 (n,🛭) Mn-56	2.6 h	21 ± 1	(1.7 ± 0.1)E-21
Fe-56 (n,p) Mn-56	2.6 h	0.4 ± 0.1	(4 ± 1)E-23
Ni-58 (n,p) Co-58	71 d	0.059 ± 0.009	(1.5 ± 0.3)E-22
Ni-58 (n,p) Co-58	71 d	0.059 ± 0.014	(1.5 ± 0.4)E-22
Sc-45 (n,2) Sc-46	84 d	0.031 ± 0.009	(2.4 ± 0.7)E-22
Ta-181 (n,☑) Ta-182	115 d	0.42 ± 0.04	(2.0 ± 0.2)E-20

It is interesting to point-out that no significant differences in induced activity have been observer in case of bare and cadmium shielded Au and In foils. Such result suggest very limited thermal neutron flux density in relation to epithermal one in considered measuring set-up. The measured reaction rates should be compared with suitable MNCP calculations for particular recorder reactions.

Collaboration

Institute of Nuclear Physics, PAS, Kraków, Poland

M. Scholz, J.W. Mietelski, P. Janowski, I. Lengar, S. Conroy

Culham Centre for Fusion Energy, United Kingdom

S. Popoviche², D.B. Syme

Josef Stefan Insitute, Ljubljana, Slovenia

I.Langa

VR Uppsala University, Sweden

S. Conroy

Association EURATOM - CCFE

Association EURATOM - VR

Association EURATOM - IJS.

References

- [1] Handbook on Nuclear Activation Data, IAEA Technical Report Series No 273
- [2] K.H. Beckurts, K. Wirtz, Neutron Physics, Springer Verlag, New York, 1964.

Neutron yield monitor as an indicator of fast particle confinement

Principal investigator:

R. Prokopowicz; rafal.prokopowicz@ipplm.pl

Collaborators from the Institute of Plasma Physics and Laser Microfusion:
B. Bieńkowska, M. Chernyshova, T. Czarski

Introduction

The fast particles confinement capability is crucial factor to sustain burning plasma ignition. The 1 MeV tritons produced in D-D fusion have slowing-down time close to those of 3.5 MeV alpha-particles emitted from D-T reactions, and therefore exhibit similar slowing-down, diffusion and confinement properties. In deuterium plasma the number of 2.5 MeV neutrons is equal to the number of produced tritons, whereas the number of 14 MeV neutrons indicate those tritons confinement properties. Study of the fusion produced tritons therefore permits investigation of the alpha-particles behaviour to be determined prior to the introduction of tritium into tokamak. The simultaneous measurements of 2.5 and 14 MeV neutron yields from deuterium plasma allow determining above mentioned alpha-particles behaviour. The comparison between the measured burn-up ratio and the theoretical one gives the possibility to test the classical burn-up model.

Work done under EFDA task WP13-IPH-A09-P2-01/IPPLM/PS is described. Simultaneous measurements of 2.5 and 14 MeV neutrons allow determining alpha particles behaviour. Thus 2 neutron detectors: one based on beryllium activation for 2.5 MeV neutrons measurement and second based on neon activation for 14 MeV neutrons measurement have been proposed.

The work described in this report has been done within EFDA task WP13-IPH-A09-P2-01/IPPLM/PS, which is the continuation of EFDA task WP12-IPH-A09-2-05/IPPLM.

Detectors

In the frame of the tasks, detection of the 2.5 MeV and the 14 MeV neutrons by activation method using threshold nuclear reactions resulting in charged particles emission has been considered. The following reactions suitable to convert 2.5 and 14 MeV neutrons into charged particles have been selected in case of both characteristic energies: ^9Be (n, α) ^6He , ^{20}Ne (n,p) ^{20}F . The reactions products decay by emitting β particles which will be recorded by means of gas detector.

For 2.5 MeV neutrons beryllium activation counter based on gas proportional detector was assembled in 2012. Calibration procedure with radioactive sources including Monte Carlo calculations has been established, performed and tested. Test measurements of 2.5 MeV neutron yield from DD reaction have been performed on PF-1000 device. The results are in agreement with standard neutron diagnostics operating with that device.

The prototype GEM detector for the 14 MeV-neutron monitor consists of 12 μ m mylar window with ~0.2 μ m aluminium layer on the inner surface, cascade of 3 GEM foils and readout plane with 0.8 mm strip pitch. Its capability for measuring β -particles is feasible due to selected activation reactions.

Monte Carlo calculations

Suitable Monte Carlo calculations of charged particles transport inside the detector have been performed by MCNP code [1]. Detailed geometry input of the whole GEM detector has been build for that purpose. 90 Sr/ 90 Y radioactive source of β particles has been modelled. Pulse height tally has been

then calculated for the energy deposited by β particles in the drift volume of the detector. The result is seen in Fig. 1.

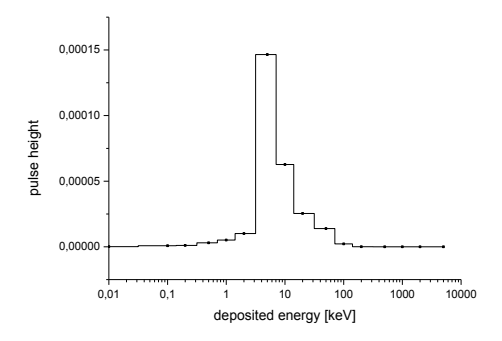


Fig. 1. MCNP calculations of energy deposited in the drift volume of GEM detector by electrons emitted from 90 Sr/ 90 Y radioactive source (normalized per one source electron).

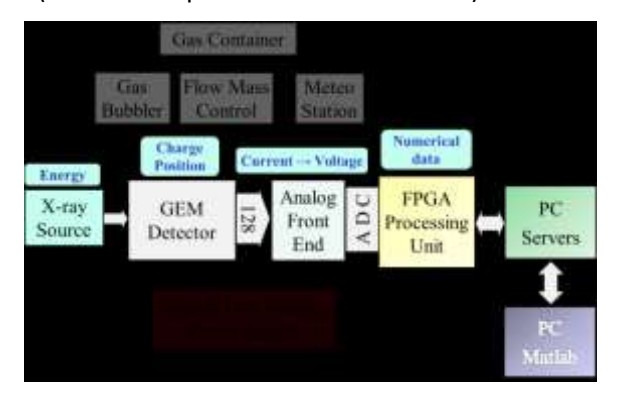


Fig. 2. Block diagram of the GEM detector measurement system.

The GEM detector system (Fig. 2) is a setup designed for estimation of the energy and position of an X-ray source. Pulse signals from 128 detector strips are shaped by 15 MHz filters and amplified by analogue front end boards – AFE. Analog signal is sampled with 77.7 MHz frequency and converted by analog-digital converter (ADC) with the 10 bit resolution. The FPGA based system performs the basic functions of data processing: the identification of charge clusters and the distributions of cluster charge and position for the current series of events. Selected data series are transferred to a PC for detailed analysis and visualization of results.

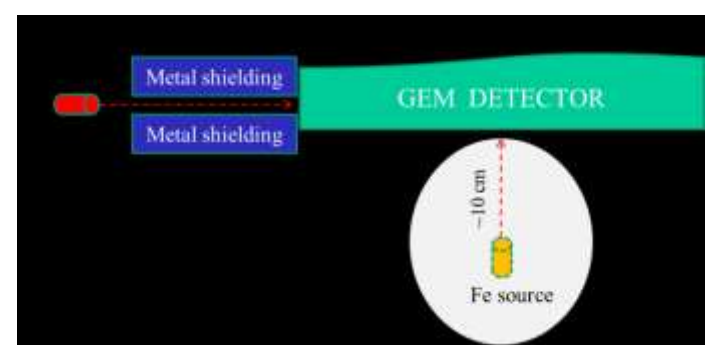


Fig. 3. The layout of the laboratory measurement for the lateral facing with β source and 55 Fe reference source.

The measurement tests with the β source have been performed with prototype GEM detector provided with 6 analog electronic boards of 96 channels in total. The detector was supplied with high voltage 5633 V, so the detector gain was established to cover the energy range up to 15 keV. The ⁵⁵Fe has been applied as the reference source with the main energy line \sim 6 keV. Several geometrical arrangements

have been considered, eg. the lateral and front facing. The layout of the laboratory measurement for the lateral facing is seen in Fig. 3. Figs. 4 and 5 show measurements results.

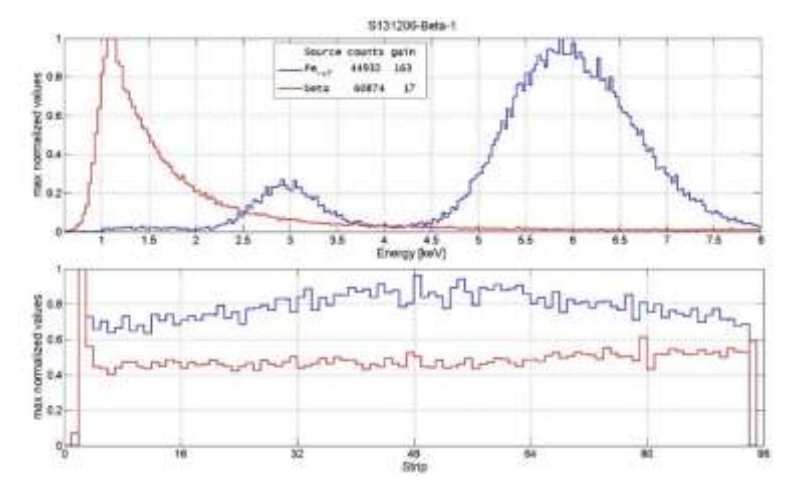


Fig. 4. Energy and position distribution for β source scaled in relation to ⁵⁵Fe reference source for the lateral facing.

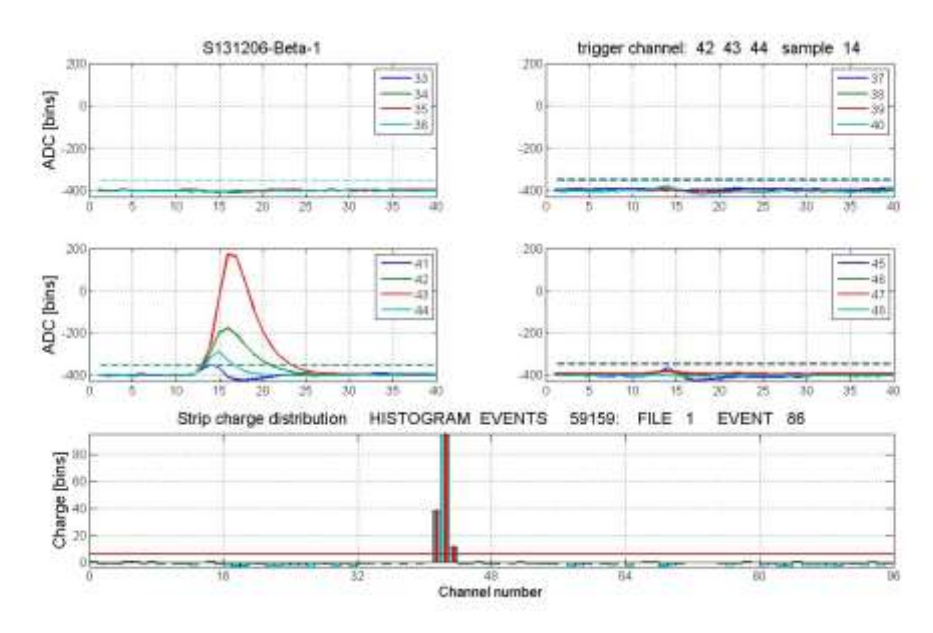


Fig. 5. Analog ADC signals and corresponding strip charges for selected β source event for the lateral facing.

Conclusions

To detect the fast electrons the T-GEM gaseous detector with 1D strip readout was constructed. Detection of fast electrons (β particles) by means of the detector has been proved. Obtained result for β -source is a typical spectrum corresponding to, so called, minimum ionizing particles, i.e. in this case, the electrons close to the relativistic energies. Despite of that, obtained spectrum does not restore exactly results of the performed simulations. Before test with the neutron source further investigations are, therefore, needed.

References

[1] X-5 Monte Carlo Team, MCNP, LANL report LA-UR-03-1987, 2003.

Development of the soft X-ray spectrometry systems for the stellarator W7-X

Principal investigator:

M. Kubkowska; monika.kubkowska@ipplm.pl

Collaborators from the Institute of Plasma Physics and Laser Microfusion:

A. Czarnecka, P. Gąsior, S. Jabłoński, J. Kaczmarczyk, L. Ryć

Introduction

The investigation of the X-ray emission from fusion plasmas has become a standard diagnostic tool used on many different fusion experiments [1]. The measurements of X-ray intensities by using Si-detectors, which are sensitive to the total radiation above a threshold energy determined by thin absorber foils in front of the diodes, yield an excellent spatial and temporal resolution. The determination of the X-ray energy spectrum using PHA systems requires sufficiently long acquisition times resulting in a poor temporal resolution. However, this method is particularly suited for long pulse operation envisaged for W7–X. The combination of spectral data obtained along a single line of sight with broadband radial X-ray intensity profiles will provide a good characterization of the impurity radiation in the plasma core. The measurements yield impurity survey spectra in the X-ray region above 0.5 keV allowing to identify the line radiation from all relevant impurities (with exception of elements lighter than nitrogen) and to determine their concentration in the hot plasma core. The slope of the hydrogen and low-Z continuum radiation is used to determine the central electron temperature. The intensity of the continuum radiation along with additional spectroscopic data allows to assess Z_{eff} values in the plasma center.

Computer simulations of soft X-ray emission from a tokamak plasma played important role in designing of each diagnostic systems. As a tool for checking the performance of the PHA and MFS spectrometry systems and optimizing filters and detectors, a special numerical code, named RayX [2] has been developed. Number of simulations have been done and the results allowed to determined the position of the diagnostics components. The super conducting stellarator W7-X will run pulse of up to 30 min duration with full heating power. Electron Cyclotron Resonance Heating (ECRH) is the main heating method for steady-state operation of the Wendelstein 7-X stellarator in the reactor relevant plasma parameters. In the first phase of working a heating power of 8-10 MW is planed to use. A wide spectrum of requirements has to be considered during the design and realization of the new X-ray diagnostics. Since ECRH auxiliary heating will be applied in W7-X, different heating scenarios, characterised by widely different electron temperature and density profiles have been taken into account [3].

Described two spectroscopic systems, PHA and MFS are being designed by IPPLM for measurement of soft X-ray emission from W7-X stellarator, which operation is foreseen in 2015. The proposed PHA diagnostic is intended to provide the spectral energy distribution with energy resolution not worse than 180 eV along a central line of sight. The system consisting of 3 single Silicon Drift Detectors (SDDs) operated with different filters will be installed on the horizontal port AEK50 on W7-X. Each detector will record an X-ray spectrum in three different energy ranges from 400 eV to 20 keV. In MFS system the recorded spectrum is determined by measurement of the total X-ray emission (as the effect from interaction of many quanta) in different ranges of energy, which are determined by the type and thickness of the filters and the thickness of the detectors (usually the ranges overlap). The MFS method is characterised by lower, in comparison with the PHA system, spectral resolution.

Pulse height analysis soft X-ray diagnostics for stellarator W7-X

In 2013 a vacuum chamber of the PHA system has been manufactured (see fig.1). All components of the system like piezo-slits and wobble sticks for filters have been mounted and preliminary tested. First laboratory tests of the SDD detectors intended for this diagnostic have been performed.

A calibration port has been mounted. It is equipped with 1mm Aluminum window which transmits photons of energy above 8 keV. A mini x-ray tube was used for fluorescence excitation (fig.2) of materials located inside the port. There are Ni, Fe, Cr, Cu and Al. In the future it is planned to add also Ti. A series of measurements have been performed in different experimental conditions (X-ray source operated at 30kV, 50μ A / 50kV, 30μ A). Acquisition time, by the means of SDD Amptek SSD detector, for each spectrum was about 20 minutes. Example of the registered spectrum is presented in fig.2b. Based on 9 identified lines (fluorescence and Fe⁵⁵) first calibration curve has been determined. The resolution of the registered spectra was about 140eV at 5.9 keV.





a)

Fig.1. (a) A photo of the PHA vacuum chamber with diagnostic port, (b) a photo of details of the PHA chamber with visible mounted set of piezo-slits.

b)

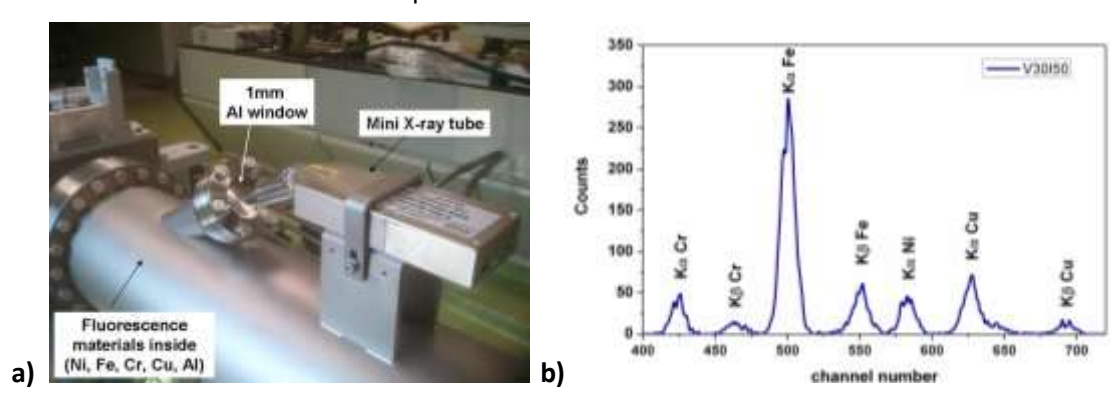


Fig. 2. A photo of the energy calibration port of the PHA system (a) with an example of the registered spectrum (b).

Multi-foil soft X-ray spectroscopy diagnostics for stellarator W7-X

In 2013 a new concept of the MFS system has been proposed. The MFS chamber will be directly mounted to the gate valve at the AEN20 port. There will be an isolation of the detector arrays with PEEK. Due to the fact that the distance between the plasma and detectors has been changed, localization of the particular components must be recalculated. New concept of the MFS system is presented in fig.3.

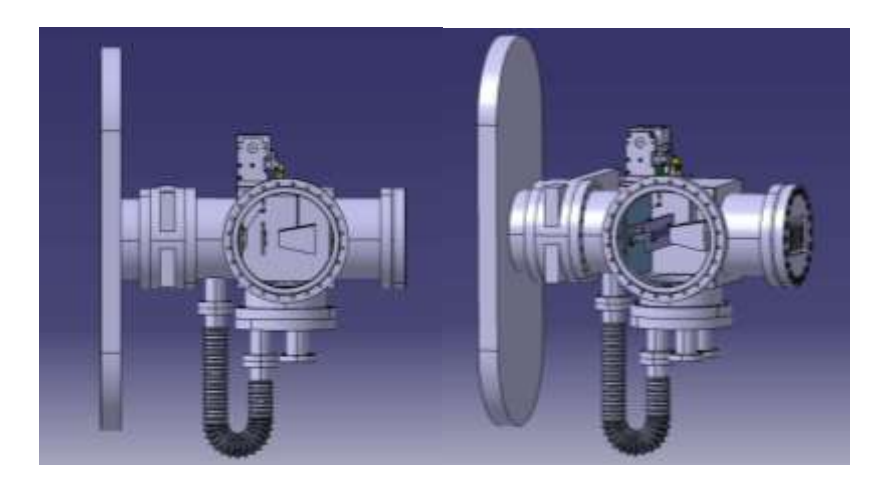


Fig.3. Modified concept of the MFS system for W7-X

Proposed modification does not required additional support. The system will be pump out by the movable turbomolecular pomp and after reach the required pressure the pump will be removed. In 2013 a calibration methods of the detectors have been also proposed.

Conclusions

In 2013 the PHA vacuum chamber has been manufactured and first tests of the piezo-slits and wobble stics have been performed. A calibration port of the PHA system has been mounted and first energy calibration curve has been determined based on 9 registered lines.

In 2013 the MFS system has been modified. The long pipe with the turbomolecular pump at the end has been removed in comparison with the previous version. It was decided that this diagnostic will have a movable pumping system.

Collaboration

Association EURATOM – Max-Planck Institute of Plasma Physics, Greifswald.

References

- [1] A. Weller, S. Mohr, C. Junghans, Review of Scientific Instruments 75, 3962 (2004)
- [2] S. Jabłoński, A. Czarnecka, W. Figacz, M. Kubkowska, J. Kaczmarczyk, L. Ryć, J. Wołowski, 1-D plasma X-ray radiation code as a first step for developing the fusion diagnostics, P2.048, 39th EPS Conference 2012, Stockholm, Sweden
- [3] A. Czarnecka, M. Kubkowska, W. Figacz, S. Jabłoński, J. Kaczmarczyk, J. Wołowski, C. Biedermann, R. Burhenn, R. König, A. Weller, Concept of pulse height analysis system (PHA) for Wendelstein 7-X, P1.052, 38th EPS Conference on Plasma Physics (2011).

Adapting the activation technique to applying on W7-X for determination of neutron yield from deuterium plasmas

Principal investigator:
S. Jednoróg; <u>slawomir.jednorog@ipplm.pl</u>
Institute of Plasma Physics and Laser Microfusion

Introduction

The plasma that is formed in large plasma experiments is characterized by vast numbers of parameters. All of them need to be monitored. A neutron activation method occupies a high position among others plasma diagnostic methods. The above method is off-line, remote, and time integrated method. It doesn't interfere and interrupt plasma parameters like temperature density and purity as well. The plasma with parameters enabling nuclear fusion reactions is always a strong source of neutrons that leave the reactions area and take along energy and important information on plasma properties.

Neutrons as a product of the fusion reaction easily escape from hot plasmas and they carry important information on plasma parameters and fusion reaction mechanisms. Therefore, the neutron diagnostics are essential in estimating these parameters and fusion power. Activation techniques are especially advantageous for the estimation of some characteristics of fast neutrons emitted from hot plasma discharges and have been used in many tokamak experiments [1]. These techniques were used to measure e.g. neutron fluence at chosen locations around the machine, even inside the vacuum vessel close to the vessel walls [2]. Supported by neutron transport calculations the activation technique can provide information on the total neutron yield and released fusion power.

In this report the Yttrium activation technique for neutron measurements is described. Preliminary measurements of the activity of natural yttrium induced by neutrons from DPF-1000U device have been carried out. Measured activity is compared with the total neutron yield measured by means of silver activation counters, which are used as a standard diagnostic on DPF-1000U. The linear relation has been found.

Activation materials

Silver as activated material is used as an effective way of neutrons measurement, especially when they are emitted in a form of short pulses like as it happens from the plasma produced in Dense Plasma-Focus devices. Other elements such as beryllium and yttrium are newly introduced and currently tested at the Institute of Plasma Physics and Laser Microfusion to use them as the suitable activation neutron detectors. This year particular emphasis was placed on yttrium activation technique.

Yttrium monitor for neutron emission yield.

Yttrium has only one naturally occurring stable isotope ⁸⁹Y. The following reaction is considered:

$$n + {}^{89}Y \rightarrow {}^{89m}Y (T_{12} = 15.663 \text{ s}) n' + \gamma$$
 ($E_{\gamma} = 908.96 \text{ keV}; I_{\gamma} = 99.16\%$)

Nuclear reaction of inelastic scattering of neutrons with yttrium nuclei has broad perspective to be implemented as the fusion neutron yttrium monitor (FNYM) in plasmas experiments. It is the threshold reaction (see Fig. 1.) that means it is mostly sensitive for primary fusion neutrons.

^{89m}Y is the relatively short lived radionuclide. FNYM does not need any neutron moderator to allow neutrons detection. Neutron monitoring is realized by simple counting of gammas emitted from activated meta state of yttrium isotope.

During conducted experiment the yttrium sample was put on the DPF-1000U surface before each discharge. Its position was situated on the 90 degree to the main axis of the DPF-1000U device and on the plain crossing the plasma focus. Yttrium was activated during discharge, then removed manually and put to the shielding house, standing close to the device, and measured after that. The removal of the sample took usually up to 20 s. The activity of ^{89m}Y (expressed in Bq) was estimated by the MCA software for the particular discharge time. The measurement of yttrium sample activity was performed with gamma spectrometry system equipped with HPGe detector. The efficiency calibration of the spectrometry system was done by the software (ISOCS/LABSOCS) attached to the system. After each measurement the yttrium sample was put again in the same position on the device wall. Using of this same sample was allowed because the repetition time of DPF-1000U is approximately 20 min. That means that all activated nuclei disintegrated and turns them self to the ground state.

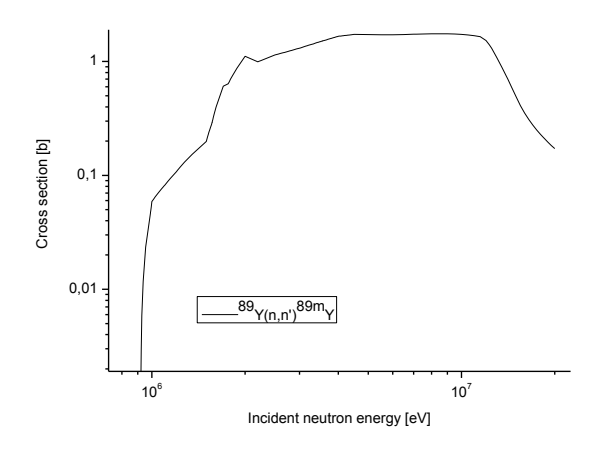


Fig. 1. Cross section for inelastic scattering of neutrons with ⁸⁹Y nuclei

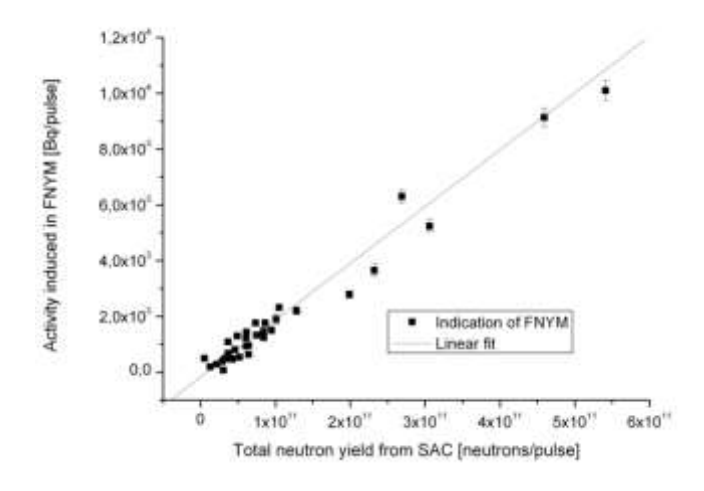


Fig. 2. Indication of the FNYM versus neutron strength expressed as indication of SAC observed during dozen of pulses performed at DPF-1000U device.

This experiment showed that activity induced in yttrium sample is directly proportional to the total neutron yield monitored by silver activation counters. The results of the measurements of activity

induced in FNYM as the function of neutron yield measured by silver activation counters is shown in Fig. 2.

Conclusions

The research that has been already performed shows that activity induced in yttrium sample is directly proportional to the total neutron yield monitored by method.

Promising result of the above experiment allows us to construct new generation FNYM, which will be a subject of the subsequent works.

References

- [1] Prokopowicz R., Scholz M., Szydłowski A., Popovichev S. and JET-EFDA Contributors (2007) Measurements of Neutron Yield from Deuterium Plasmas at JET by Activation Techniques, Plasma 2007, AIP Conference Proceedings Vol. 993: 251-254
- [2] Prokopowicz R, Bieńkowska B, Drozdowicz K, Jednoróg S, Kowalska-Strzęciwilk E, Murari A, Popovichev S, Pytel K, Scholz M, Szydłowski A, Syme B, Tracz G, JET-EFDA Contributorsd, (2011) Measurements of neutrons at JET by means of the activation methods. Nucl Instrum Meth A 637:119–127

Development of new hardware and firmware for GEM detector dedicated to neutron and soft x-ray position and energy measurement

Principal investigator:
T. Czarski; tomasz.czarski@ipplm.pl
Institute of Plasma Physics and Laser Microfusion

Introduction

The project started in 2013. The main goal of the project was a significant increase reliability of electronic system for plasma diagnostics. The work included three objectives:

- development of control and real-time monitoring to keep data transmission quality,
- achievement of high-speed data transmission links long-term stability to deliver high quality results of W-spectra data acquisition,
- monitoring of proper GEM detector calibration and DPU synchronisation is required to achieve high quality results of W-spectra measurement.

The project was divided on two parallel tasks:

- development of new parametrized and behavioural algorithms implemented in FPGA firmware for GEM detector dedicated to neutron and soft x-ray position and energy measurement
- development of new parametrized and behavioural algorithms implemented in FPGA firmware dedicated to calibration procedures for GEM detector DPU.

The project started in 2013. The main goal of the project was significant increase of electronic system reliability for plasma diagnostics. Development of new algorithms implemented in FPGA firmware for GEM detector dedicated to neutron and soft x-ray position/energy measurement and also calibration

procedures for GEM detector Data Processing Unit (DPU) were designed and implemented. The algorithms were written in VHDL language. A complete transmission-receiving fast link was realized in form of stand-alone parameterized components for 46 fast links implemented in 21 FPGA chips of GEM of plasma diagnostics system.

Firmware design for FPGAs of GEM detector DPU

The base of the synchronization algorithm for each fast data transmission link between two FPGA circuits (sender and receiver) is auto-synchronization of two identical pseudo-random generators located in the transmitter and receiver [1]. Synchronization status of both generators is derived by comparison of identical sequences produced by both circuits. New algorithms has been developed:

- to control and real-time monitoring of current transmissions quality: a pseudo-random generator,
 data transmitter, data receiver and pseudo-random data synchronizer were implemented in the FPGA
 circuits. A control data interface was realized also;
- to monitor data transmission quality in real-time: new procedures of control and data processing based on the Matlab environment were prepared. The procedures automatically configure each of 46 fast link transmission parameters. Quality of fast data transmission generated by pseudo-random generator was tested.

A parametrized and behavioural algorithms were written in VHDL language for 46 fast links implemented in 21 FPGA circuits. A functional simulation was performed to confirm algorithm behaviour, then timing simulation was performed to verify the correctness of compilation and FPGA resources placement and routing. Finally 21 FPGA circuits were programmed, then 46 fast links were configured and tested based on Matlab procedures.

Conclusions

A complete transmission-receiving fast link was realized in form of stand-alone parametrized components. The components were written in VHDL language in a form of behavioural description. The components were successfully used in different applications for several families of Altera circuits (Cyclone and Stratix), and for several families of Xilinx circuits (Spartan and Virtex). There was transmission established for several different values of user data width. Pseudo-random generator synchronization performance test has shown that usage of 8 bit data width gives reliable results. Finally, the components were successfully applied in large multichannel measurement system, build with the usage of numerous FPGA circuits for JET plasma diagnostics.

Collaboration

Warsaw University of Technology
Krzysztof Poźniak, Grzegorz Kasprowicz

References

[1] Krzysztof T. Pozniak: FPGA based fast synchronous serial multi-wire links synchronization. Photonics Applications in Astronomy, Communications, Industry, and High-Energy Physics Experiments, 27.05-2.06.2013, Wilga, Poland.

2.3 Emerging technologies

Erosion behaviour of W-containing steels. Laboratory measurements and impurity influx in tokamaks from eroded samples

Principal investigator:

M. Kubkowska; <u>monika.kubkowska@ipplm.pl</u>

Collaborators from the Institute of Plasma Physics and Laser Microfusion:

P. Gąsior, E. Kowalska-Strzęciwilk, M. Rosiński

Introduction

The use of a stainless steel wall in a reactor, at least partially in the main chamber, has been often proposed in the past. This was mainly due to a fact that W is expensive and the joining of W to the support structure like e.g. EUROFER is difficult. Pure W is brittle, and its material properties degrade due to neutron irradiation. The general objective of the realized task was to determine whether steel, EUROFER could be a suitable main chamber plasma facing components (PFC) material for DEMO. Presented studies were performed in frame of the WP13-PEX-03a-T03-01 task and were focused on laboratory experiments of laser or plasma streams interaction with tungsten (W) and stainless steal (316L) (SS) samples. There were also prepared an experiments with laser deposition of tungsten ions on SS substrate.

Experimental arrangement prepared for generation of tungsten ion streams using a repetitive pulse laser system

The experimental system for preparation of SS sample with thin W layer consisted of interaction chamber, a repetitive laser, movable target holder and ion collectors. The repetitive pulse Nd:YAG laser system of parameters: energy of about $0.5 \, \text{J}$ at $1063 \, \text{nm}$ in a $3.5 \, \text{ns}$ -pulse, with repetition rate up to $10 \, \text{Hz}$, intensity on the target of up to $10^{11} \, \text{W/cm}^2$, has been employed to produce tungsten ions emitted from irradiated a pure tungsten target. The laser beam was focused at an angle of 11° with respect to the target normal.

The stream of tungsten ions emitted along the target normal was implanted/deposited to pure Stainless Steel target located at the distance of 8 cm. The surface of the sample was deposited also by neutrals (atoms, debris, clusters) not recorded by the ion collector. The laser spots had diameters of D_f = 2 mm (corresponding laser intensity was: I_L = 10^{10} W/cm²). The typical ion collector signal recorded at the distance of 8 cm is presented in Fig. 1. The ion signal from this collector was used to determine an average value of energy of tungsten ions escaping from the tungsten plasma plume. This value of energy in maximum of the signal was estimated to be 900eV.

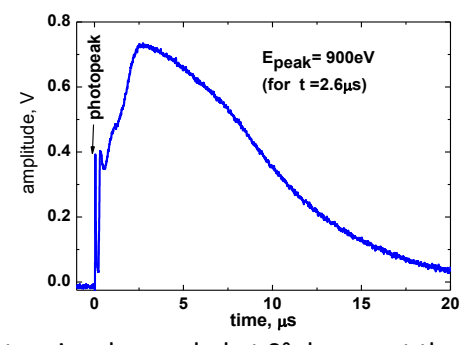


Fig. 1. An example of ion collector signal recorded at 0° degree at the distance of 8cm from the target.

Investigated samples

Two samples have been prepared. In first case, tungsten ions were deposited on the polished SS sample (sample1), in the second case ions were deposited on the roughened surface of SS substrate (sample2). Structural changes in target surfaces, before and after their irradiation with the laser pulses, were investigated by means of SEM, EDS and profilometer at Warsaw University of Technology. The aim of thestudy was to evaluate the effectiveness of removing layers using different exposure parameters.

Microscopic results of the samples

Microscopic analysis of sample2 on the polished side, did not reveal any defects of the tungsten layer like blistering or flaking. SEM images ofthe layer are shownin Figure 2.

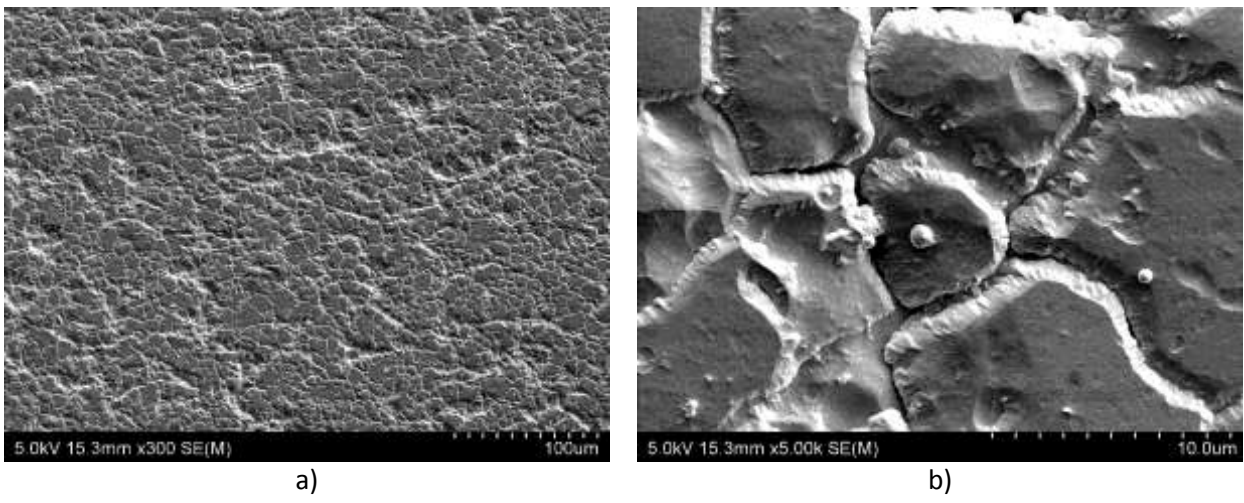


Fig. 2. SEM images of the tungsten layer deposited at the polished SS substrate (sample 2).

On the sample surface islands of tungsten are visible, while on the borders between the grains the empty place are visible, what could suggest that growing material has not fulfilled all the free spaces. Figure 3 presents a cross-section of the polished side of the sample2 made by FIB technique. The examinations revealed that its thickness is about $0.8 \, \mu m$.

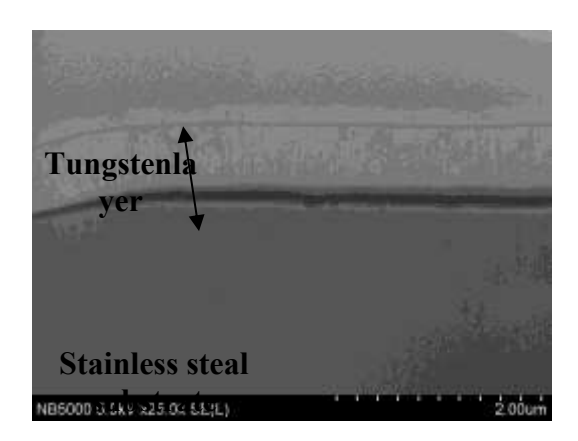
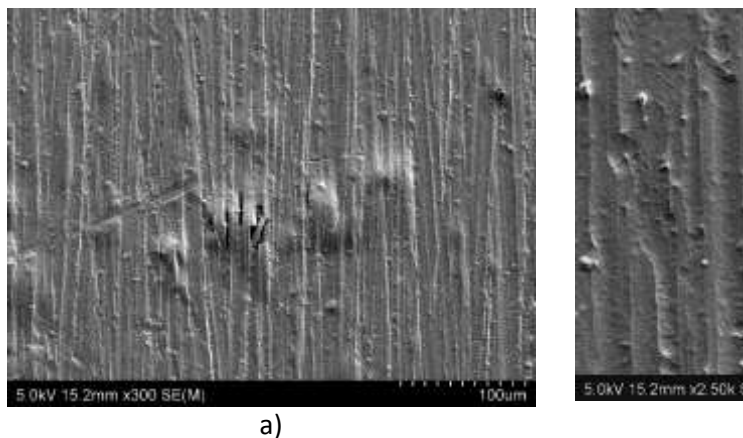


Fig.3. A cross-section of the tungsten layer, sample2, polished side

Microscopic analysis of sample2 on the roughened side, revealed a visible blistering and flaking. SEM images of the layer are shownin Figure 4. On the sample surface a long bands are visible resembling scratches after grinding. Besides, in many places blisters and cracks are visible. On the surface, also droplets of the material are visible.

A cross-section of the roughened side of the sample2 made by FIB technique revealed that the artificial deposit examinations has thickness about $0.85~\mu m$.



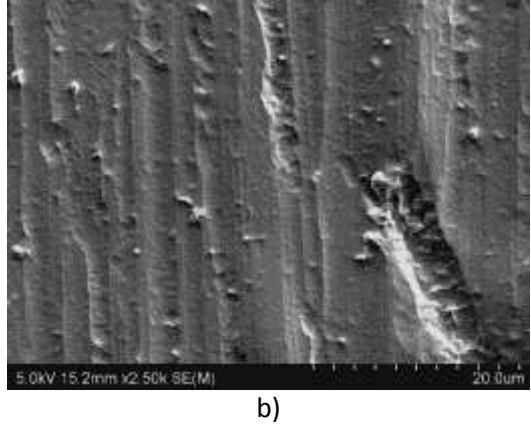


Fig. 4. SEM images of the tungsten layer deposited at the roughened SS substrate (sample2).

Laser interaction with the prepared sample

After the preparation of the sample, laser experiments have been performed. In this case a Nd:YAG laser delivering energy of 200mJ at first harmonic in 10ns was used with power density about few GW/cm². On the surface of sample1, three craters were made. First one was formed after 2 laser pulses, second after 4 and third after 10 laser pulses. Spectroscopic measurements made by Me5000 spectrometer equipped in iCCD camera, showed that the tungsten layer is removed after first two shots. An example of registered spectra is presented in fig.5.

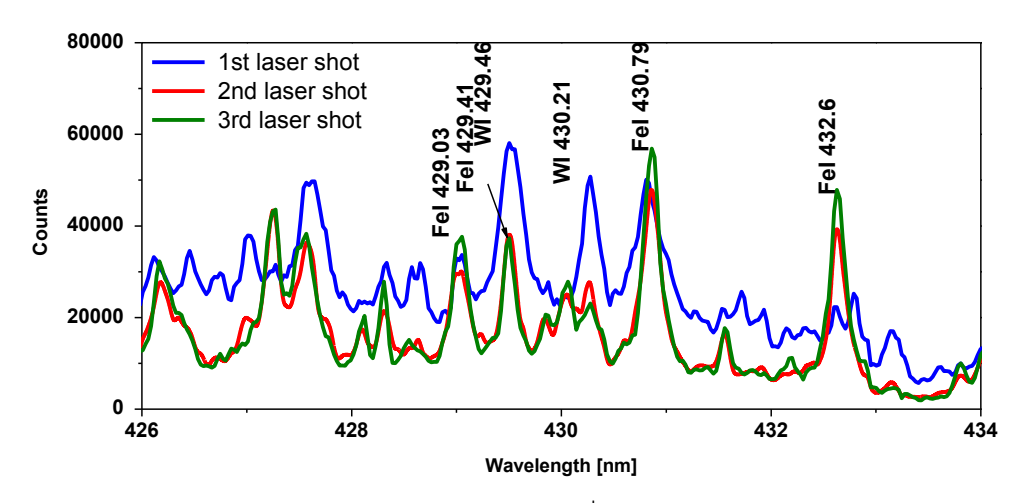


Fig. 5. Example of registered spectra from the sample1 (2nd crater) for the following experimental conditions: acquisition time was 500ns, delay between laser pulse and starting the acquisition was 1500ns. Experiment was performed in air condition.

Microscopic investigation of these craters confirm that the layer is removed after first shots. Detailed analysis of the first crater (formed after 2 laser shots) showed that large parts of the tungsten layer dropped off, revealed undamaged substrate. During the process of tungsten ions deposition part of the layer filled the empty spaces between the grains of the SS substrate.

In second crater microscopic investigation showed that the substrate has been uncovered. In the melted zone (2002m) a mixing of the materials (W and SS) occurred as well as evaporation of the material. The last crater which was formed after 10 laser pulses also has uncovered substrate with

melted zones. Additionally, on the boarder between melted material and uncovered substrate, characteristic bank is observed. In the centre of the crater, in re-melted zone a mixing of the materials (W and SS) occurred as well as evaporation of the material (similar like in case of 2nd crater).

Conclusions

Summarizing, the nature of the layer strongly dependent on the morphology of the substrate, however in presented cases the thickness of the layer is in both cases (polished and roughened) similar. We are planning to focus future work on plasma streams interaction with tungsten, stainless steal and stainless steal with tungsten layer samples with the use of plasma focus device. In 2013 samples of tungsten and 316L stainless steel were also exposed at PF-6 device with energy density of about 100 J/cm² but detailed analysis is still needed.

Collaboration

Warsaw University of Technology.

Study on fuel retention and removal in mixed material ITER-like layers

Principal investigator:
P. Gąsior; pawel.qasior@ipplm.pl
Collaborators from theInstitute of Plasma Physics and Laser Microfusion:
A. Czarnecka, W. Figacz, E. Kowalska-Strzęciwilk, M. Kubkowska,
R. Miklaszewski, L. Ryć

Introduction

The study on the topic was conducted in two subtasks included in EFDA program, namely, "Influence of mixed surface layers on fuel retention and release" and "Assessment of Fuel Removal Methods and Dust Generation". The first task was additionally divided into two sub-tasks "The experiments with the laser treatment of the hydrogenated/deuterized mixed material (WAIC) layers and bulk tungsten (reference) samples" and "The experiments with bulk tungsten and stainless steel samples subjected to interactions with plasma streams in the PF-6 device".

The experiments on fuel retention and removal in mixed material ITER-like layerswere carried on with the use of pulsed laser systems to irradiate mixed material deuterium/hydrogen containing samples as well with the use of PF-6 device to subject the samples with adequate heat loads. The process were investigated in real time with the use of spectroscopic diagnostics as well as post-mortem with the use of the techniques of material research.

Results and discussion

1. The experiments with the laser treatment of the hydrogenated/deuterized mixed material (WAIC) layers and bulk tungsten (reference) samples.

The laser treatment of the samples with the ~3.5 and ~10 ns laser pulses of energy of 50-600 mJ was oriented for the following goals:

i. comparison of the deuterium contents (by the LIBS – Laser Induced Breakdown Spectroscopy) in mixed material and bulk samples,

- ii. for the first time observation of the aging effects on the retention in the mixed material layers (previously reported for carbon-based materials),
- iii. for the first time demonstration of the application of the DP-LIBS (Dual Pulse LIBS) method for WAIC layers,
- iv. preparation of the samples for the material research analysis performed at WUT and IPP.CR.

Referring to (i), the experiments have shown that in the bulk substrate, both the concentration and the penetration depth of the hydrogen isotopes can be higher than in the case of retention in the WAIC layers produced by DIARC on tungsten substrates. Such a behaviour was indicated by the higher magnitude of the hydrogen line observed for the irradiation of bulk tungsten (99.99% W) in comparison to the magnitude of the deuterium/hydrogen line observed for both types of the DIARC WAIC samples (labeled as deuterium contents #1 and #3). The deuterium/hydrogen component in the spectrum was also maintained for a larger number of the laser pulses in the bulk tungsten than in the layer (which could also be caused by the lower ablation rate of bulk tungsten than that for the covered with the layer, at least at the initial stage of the removal process).

To verify how aging can influence the contents of the hydrogen isotopes retained in the WAIC layers (ii), the experiments have been reproduced at the IPPLM after approx. 8 months with the use of a standard - single pulse LIBS and DP-LIBS in a joint experiment with the ENEA Frascati team (iii). The experiments showed that application of the DP-LIBS can enhance the SNR of the acquired signals and moreover, it can be optimized for the detection of a given light-emitting element. The experiments on the measurements of the hydrogen isotopes contents in WAIC and bulk samples showed the decrease in the contents in the WAIC samples (the deuterium/hydrogen signal was very close to the noise) while for the bulk tungsten substrate the amplitude of the H signal was very similar to that obtained in the previous series of the experiment. It suggests that the WAIC layers, in terms of the hydrogen isotopes retention, behave differently than top surface of a bulk substrate in a way that it enhances of the gas release. It is also worth to notice, that it somehow 'protects' the top surface of the substrate layer from absorbing hydrogen isotopes, as the experiments showed that their contents on the uncovered surface is lower than on the surface of bulk tungsten without the layer.

It can be possibly explained in a way that the layer has a very weak susceptibility for the hydrogen isotopes retention which prevents the gases from penetrating it and reaching the substrate. Moreover – even if any gasses are released from the bulk to the layer (by the means of diffusion) it is more likely that it will be ultimately released than it returns to the bulk.

In the step (iii) which was conducted in a joint experiment with ENEA Frascati samples exposed to plasma operation in the COMPASS tokamak were also investigated. These samples were graphite substrates with thin tungsten/steel coatings deposited by the PVD and had some deuterium contents in their surface layer (100nm) due to contact with plasma in COMPASS. For these samples the deuterium was removed by a single laser pulses of the fluence of $^{\sim}25 \text{ J/cm}^2$ together with the metallic layer which was documented by LIBS. The material research on the WAIC samples prepared by DIARC which were conducted by WUT showed a very good stability of the layer. Even after the five laser pulses deposited onto one spot the layer was still not completely removed and the interaction area could have been divided into 4 zones with increasing impact of the laser produced damage. It is worth to be mentioned that in the zone with the lowest damage impact mainly dust particles have been removed from the surface. Application of the power density (which is in range of $10^8 - 10^9 \text{ W/cm}^2$) may lead to dust removal. This observation may be useful for techniques of dust removal from the mixed material surfaces without inflicting damage to the layer itself (It should be noted that the phenomena occurs like that not only for the power density level, but also the short pulse time is crucial).

In the areas of the higher power density (up to 30 GW/cm²) melting and cracking of the layer, especially after several laser pulses can be clearly seen. The WAIC layers prepared at the IETM and on the

COMPASS samples appeared to be significantly less stable and were removed by 3-5 laser pulses (IETM) and even after 1-2 laser pulses (COMPASS samples).

2. The experiments with bulk tungsten and stainless steel samples subjected to interactions with plasma streams in the PF-6 device

In the research the bulk tungsten samples have been subjected as the refeference for the further investigation of the samples of tungsten coated with the mixed material layers. The stainless steel samples were subjected in the heat loads in the same conditions to give the reference for the investigation by the material research means (at the IPP.CR) of the materials with a diverse chemical composition. Moreover, this type of samples was convenient from a point of view of the investigation of application of Stainless steel-based materials in further tokamak reactors and in presently being built Wendelstein 7X stellerator. The results of the investigation of the behaviour of the stainless steel gave an insight in the mechanisms governing plasma-wall interaction for this type of materials, especially formation of carbon-based morphology structures which are also present in the WAIC layers. For the samples exposed for the interactions with plasma streams in the PF-6 device the exposition parameters of the device operation were as follows: Charging voltage = 10 kV, Filing pressure= 5Torr, Anode-sample distance =8.5 cm. It allowed for the estimation of the power load deposited on the sample surface (per shot) for the plasma stream at ~10⁷ W/cm², and for the fast ion stream (mean energy ~100 keV) at 10¹⁰ W/cm². As the pulse duration was ~10 ns it meant that the energy load for the plasma stream was ~0.1 J/cm² and for fast ion stream (mean energy ~100 keV) ~100 J/cm².

In general, the research showed that the main mechanism of the material damage for both tungsten and stainless steel is melting; however; for the stainless steel, the morphology of the structure indicates that the material reached its boiling point and for the tungsten crack formation becomes equally important which leads to formation of the specific morphology structures in which melted zone boundaries are defined by the cracking network patterns.

3. Fuel Removal Methods and Dust Generation

Experiments of laser-removal of deuterium containing mixed material layers of tungsten, aluminum and carbon from tungsten substrate have been performed both in air and in a vacuum chamber. As a source for removal a Nd:YAG laser with fluences about 2, 14 and 25 J/cm² was used. The LIBS (Laser induced Breakdown Spectroscopy) method was applied for investigation of laser pulse-sample interaction. By means of LIBS it was possible to observe that for 25 J/cm² the mixed materials W:Al:C layer of about 3 means of the laser removed after 7 laser shots. For lower energy densities the W:Al:C layer has not been removed even after 10 laser shots while for deuterium, there were no difference observed depending on applied fluences and in all cases this layer was removed after 1-2 laser pulses. The research was focused on investigation of the effects of the laser irradiation on morphology and microstructure of deposits and substrates. The morphology of the sample before and after laser irradiation was characterized by scanning electron microscopy, scanning transmission electron microscopy, focus ion beam and energy-dispersive X-ray spectroscopy.

The detailed analysis of the craters showed that substrate had been uncovered only in the case of application of the energy density at level 25 J/cm² and after 7 laser shots. In that case in the central part of the crater, the W:Al:C layer has been totally removed and tungsten substrate has been uncovered. For the lower energy density, 14 J/cm² and2 J/cm², the tungsten substrate has not been uncovered and only the mixed material layer has been re-melted and partly removed. The morphology of deposits and substrates after interaction with laser pulses characterised by different microscopic methods was also confirmed by the registered spectra. In case of the energy density of 25J/cm² spectrum after 10 laser shots was dominated by tungsten lines while for lower fluences in the spectra recorded after 10 laser pulses, Al and C lines were clearly visible. In the spectra observed for the highest fluence, Al and C lines were also identified but their intensities were lower in comparison with the rest applied energy

densities. In the future, it is planned to analyse spectra and surface sample after many more laser pulses to find the conditions when only tungsten lines are observed.

On the surface of the investigated sample the deuterium presence was also observed. The process of removal of this element was investigated by observation of the D-alpha line using Me5000 spectrometer. In that case the experiments were performed in vacuum conditions to eliminate hydrogen line which might appear from the air. It was checked that deuterium has been totally removed after 1 or 2 laser pulses, in dependence of the location on the sample surface (content was not homogenous). It is worth noting that for three applied energy densities the deuterium was removed after the same number of laser pulses (1-2 laser shots). Results have been presented at the 11th ISFNT Conference - M. Kubkowska, et al. Study of laser-removal and structural changes of W:Al:C layer with Deuterium content.

Conclusion

Influence of mixed surface layers on fuel retention and release

The research has fruited in several interesting and important observations. The release of the hydrogen isotopes from the WAIC layers is a good message, the same as the low capability of this material to accumulate high amounts of deuterium. It should be noted, that the deuterium can be completely released from the layer (proved by LIBS) by the mechanisms of desorption/evaporation before the mixed layer is removed (proved by the material research). Hence, the consequences for the development of the methods of fuel removal are quite obvious. Incomplete removal of the WAIC layer may be used as a screening layer preventing the permanence of the hydrogen isotopes into the bulk, however, the optimization of this methods still need the research. This research is going to be conducted in the framework of the EuroFusion tasks. The material research techniques again proved to be very useful for the analysis of the plasma-solid and laser-solid interactions. In the research, a great opportunities can be offered by a tokamaks as COMPASS which not only provides the access to the tokamak-plasma-treated samples but also offers the possibility to treat the samples affected by the laser or PF-6 irradiation by the tokamak plasma. This possibility Is going to be extensively investigated in the upcoming EUROFUSION tasks.

Assessment of Fuel Removal Methods and Dust Generation

The preliminary research showed that standard q-switched Nd:YAG laser pulses (i.e. with an energy of a part of J and time duration of a few ns) can be used for fuel removal from the first wall together with the mixed materials layer (co-deposited layer). The comparison of behavior of the D-alpha line with the lines of mixed material components evidently proves that the physical mechanisms of removal of the gas and solid structures are different (namely, ablation for W, Al and C and evaporation for D). It also leads to a speculation that in this type of mixed layers D is present rather in form of trapped D_2 or HD particles and does not tend to form hydrocarbon bonds representative for thick TEXTOR-like codeposits described in [1-2]. The speculation originates from the assumption that if the D was trapped in hydrocarbon particles, it would be more resistant against the removal and D particles from deeper layers would not have been released until these layers had been exposed for the laser light. This conclusion is also in line with the results in [1] which did not show significant change in hydrogen removal from W:Al:C mixes with variable carbon contents. On the other hand it is questionable if the application of the Nd:YAG laser can be competitive with the fibre laser [3] especially when one is interested in fuel removal without the influence on the original surface.

Nevertheless, the results presented in this paper are valuable for confirmation that LIBS supported by pulsed Nd:YAG lasers can be applied for investigation of deposition on mixed material PFC without dramatic influence on their original surface.

Collaboration

Warsaw University of Technology
Lukasz Ciupinski, Elzbieta Fortuna-Zalesna
Association EURATOM/ IPP.CR, Institute of Plasma Physics, Czech Republic,
Association EURATOM/ ENEA Frascati, Italy.

References

- [1] P. Gąsior, et al., Journal of Nuclear Materials 390–391 (2009) 585–588
- [2] D. Ivanova, et al. Physica Scripta, T145 (2011) 014006
- [3] M. Kubkowska, et al., Journal of Nuclear Materials 438 (2013) S750–S753.

Feasibility study of the use of the JET EDGE LIDAR system for in-situ characterisation of layers

Principal investigator:
P. Gąsior; <u>pawel.gasior@ipplm.pl</u>
Institute of Plasma Physics and Laser Microfusion

Introduction

Unacceptable long term retention of the fuel (tritium) in the walls of fusion devices is one of the most critical issues, especially for ITER and for the development of a fusion reactor. This issue requires additional R&D in several directions, such as cleaning the inventory of a fusion device (ITER) from accumulated tritium, mitigating the retention by proper choice of wall materials and operational scenarios and also developing methods to quantify the amount and location of retained tritium inside the fusion device.

In preparation for ITER, JET has been upgraded with a new ITER-like Wall (ILW) [1], whereby the main plasma-facing components, previously made of carbon, have been replaced by beryllium (Be) in the main chamber and tungsten (W) in the divertor. The tritium inventory with such choices of facing materials is expected to be dominated by co-deposition with beryllium and the remaining carbon, with a minor contribution from T retention in the bulk of the W tiles [2]. The experiments during the last campaigns demonstrate that the long-term retention rate with the ITER-like Wall exhibits a significant decrease compared to the carbon wall references [3]. Nevertheless, further investigations of the longterm retention under different plasma scenarios are required. The material deposition determines not only the long term T retention by co-deposition but also the production of dust and flakes by disintegration of the deposited layers. Tritium might be transported to remote areas of ITER where actual removal techniques are not efficient. Thus, in situ characterisation of deposited layers (tritium quantity and surface distribution, thickness, composition) and deposition layer detritiation are of major importance for fusion device operation. Laser-based methods combined with optical spectroscopy during discharges and laser-induced breakdown spectroscopy (LIBS) between discharges could provide in situ data on the amount of material deposition and on fuel retention. A tile removal is unnecessary and the method is compatible with tritium, beryllium and neutron activation.

Laser-based methods have been under investigation for several years in EFDA tasks [4-13] to provide in situ data on material deposition and fuel retention using lasers which provide the light through a port-based system with windows. The possible installation on a port system allows a wider application of lasers systems and the analysis started therefore with a broader view to compare and qualify two laser techniques, such as Laser-Induced breakdown spectroscopy.

The main goal of the current task was to investigate the feasibility of measuring and monitoring in situ the hydrogenic retention and the local growth and composition of layers on first wall components by using the existing JET Edge Lidar combined with optical spectroscopy during discharges (LIAS) and laser-induced breakdown spectroscopy (LIBS) between discharges. Additionally, the aim was to demonstrate that LIBS and LIAS are reliable diagnostics for the absolute determination of hydrogen isotopes retention and deposited layer composition in the JET tokamak.

The task had a very broad range and was conducted in co-operation between FZJ (the task co-ordinator), IPPLM and TEKES. This report is based on the final report submitted to JET and is mainly concerned on the deliverables provided by the IPPLM, namely:

- Sensitivity study of the systems for the LIBS application (detection limits for H-isotopes absolute content),
- Description of the procedure and involved equipment.

Experimental arrangement

The experiments have been conducted in a set-up which was common for investigation of laser-solid interactions for the PWI research and is presented in figure 1.

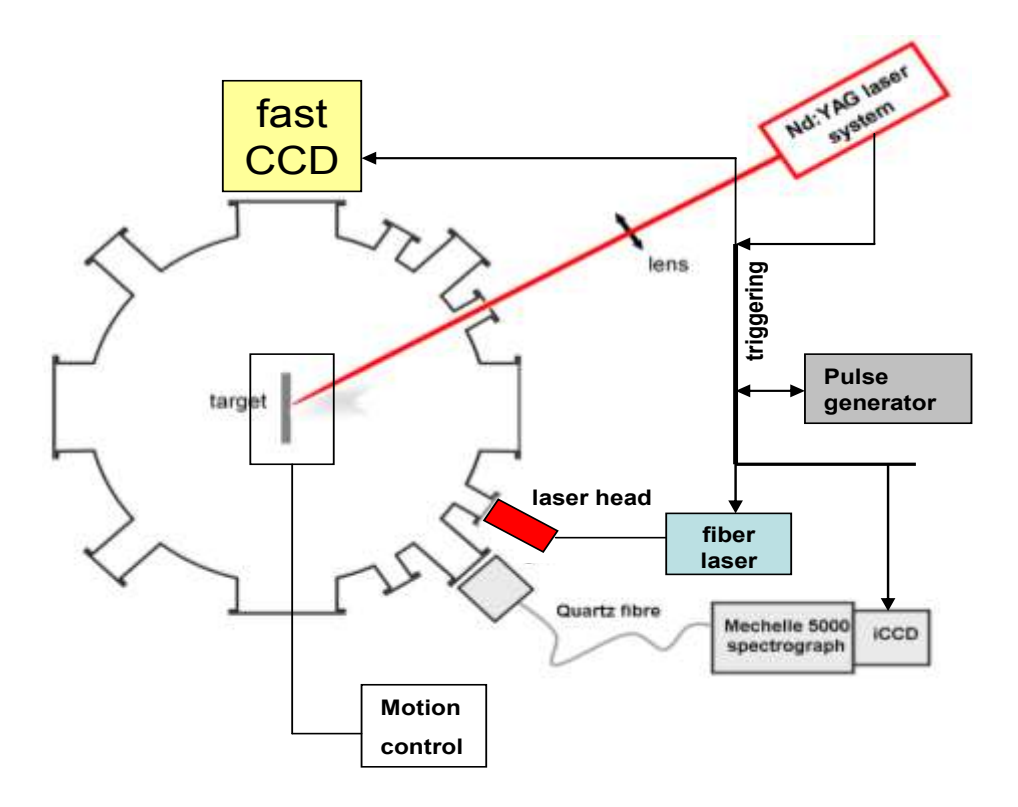


Fig. 1. Experimental set-up

Similar as in previous research, eg. [13] the samples were mounted in the vacuum chamber which was outpumped to $^{\sim}5x10^{-5}$ mbarr and subjected to single or double pulse laser irradiation with controlled power density of the beam delivered onto the target surface. The spectroscopic signal was collected by the collimating optics and provided to the MECHELLE 5000 spectrometer equipped with the IStar ICCD camera.

Results and discussion

The results can be grupped into 2 deliverables which were contributed to the IPPLM.

<u>Deliverable 7 "Report with description of the procedure and involved equipment"</u>

The study was based on the experimental works and analysis of the previously performed research.

The results of the previous experiments indicated that:

- the procedure should start with the measurements with calibration samples with fixed and different deuterium contents (however; these contents should not significantly different from the range of the contents foreseen for fuel retention),
- the optics should provide proper focussing of the laser beam to reach the power density in range of 109 up to 10^{10} W/cm2 as the results shown that in this range of the power density it is possible to obtain spectra which are intense enough and have sufficient SNR.
- the delay between the laser pulse and acquisition time should be properly set. Too short delay results in a low signal to background ratio. Thanks to the fact that hydrogen isotopes are released in relatively long-lasting thermal process, in spite of their high speed (of particles propagation), they can be observed still after relatively long time (in range of 100-200 ns delay),
 - the collecting optics should be carefully designed especially in the case of a large device.
- if investigation of the spectral lines of W, C, Be and H is under consideration the Echelle spectrometer equipped in an ICCD camera is the most convenient solution (however, the choice should be done carefully some of high-quality Echelle spectrometers have a gap in the range corresponding to the hydrogen alpha line). On the other hand, if only hydrogen/deuterium/tritium lines are under consideration an optical filter for the proper wavelength and the photomultiplier would be a reasonable and cheaper solution.

Another possible solution would be applications of two spectrometers with relatively narrow observation range as the lines of W, C, Be and H can be grouped into two wavelength windows of interest. The new experimental works allowed for finding the following conclusions:

- in order to minimize the damage which the laser beam induces to the surface of the target the energy delivered in a pulse should be minimized while the power density should be maintained. The research at the IPPLM showed that for $^{\sim}10$ ns pulses the pulse energy can go down to $^{\sim}50$ mJ with proper focusing.

From this point of view, lasers with short pulse and lower energy are promoted, additionally with assumption that in the tokamak application the power density should be high due to large observation distance.

- the system should be automated if scanning is foreseen. It is especially important if during the scanning of larg surface adequate to the tokamak divertor, the distance from the laser head and the target on the wall is variable. It can be obtained by involving a motion stage on which the focusing system is mounted. Its position should be controlled by the computer/microprocessor system based on

the "map" written in memory or based on the simultaneous distance measurement provided by another technique (e.g. a LIDAR system),

- double pulse laser operation has also been tested with various parameters of the deposited energy in a pulse, delay between the subsequent laser pulses and the delay between the pulses and the observation start. The preliminary tests have been performed in the atmospheric pressure conditions. However, in this conditions the correct observation of the deuterium contets as the signal from the atmospheric hydrogen (from the water vapour) is high enough to interfere, the high level of the hydrogen signal from the water vapour (which in the laboratory conditions takes less than a few percent of the air) is a good premise for finding the detection limits of its isotopes also in the vacuum conditions,
- the optimal separation of the ~10 ns, 50 mJ pulses has been assessed for ~100 ns for hydrogen detection while the observation time was in range of 300-500 ns and the delay after the pulses was in range of 1 μ s.

<u>Deliverable 6 - Report "Sensitivity study of the [Edge LIDAR] systems for the LIBS application"</u>

The study was based on the experimental works and analysis of the previously performed research. The application of the LIBS method have been previously tested at the IPPLM for the components of the thermonuclear reactors (TEXTOR, AUG) and calibrated samples; however; its performance has not been tested in terms of its sensitivity for small amounts of deuterium isotopes in mixed material layers. The preliminary study have been conducted for the TEXTOR limiter samples and indicated that the limit of detection was at the level of 10¹⁶; [13] however; the structure of the co-deposit in had a structure of a thick "sponge" and was not strictly relevant for the mixed material layers which tend to be significantly thinner and denser. Layers of this type have been also tested at the IPPLM and gave encouraging results in terms of the assessment of the determination of the contents of the W, Al and C components but the manufacturing process of the preparation of the samples did not include addition of the calibrated amount of hydrogenium/deuterium. Despites this, the experiments presented in [13] have shown that both retention and the LIBS sensitivity did not differ strongly in dependence of the ratios of W:Al:C in the mix which was an optimistic premise.

The possibility of the estimation of the detection limits was checked with the use of the DIARC samples with calibrated deuterium contents. In the experiments with these samples, both with DLC and mixed material layers, the deuterium at the level close to 10^{17} D/cm2 was easy to detect; however; it (deuterium) could persist only a few lasers shots and after that no traces were observed besides the tungsten substrate. In contrast to this, the signals obtained for pure bulk tungsten had hydrogen indicators for a significantly larger number of laser pulses. It can be possibly explained in a way that the layer has a very weak susceptibility for the hydrogen isotopes retention which prevents the gases from penetrating it and reaching the substrate. Moreover – even if any gasses are released from the bulk to the layer (by the means of diffusion) it is more likely that it will be ultimately released than it returns to the bulk. On the other hand a "smooth" dependence of the amplitude of the hydrogen line for subsequent laser pulses onto the bulk indicates a good sensitivity of the method, as in fact the gas is being released gradually. Unfortunately this dependence cannot be expressed by numbers as the changes of the deuterium concentration vs the laser beam penetration depth are not known.

Based on the calibrated contents of deuterium in WAIC layers the limit of detection of hydrogen isotopes has been estimated at least as good as $^{\sim}10^{17}$ D/cm2 based on the SNR ratio for the signals obtained for the layers of deuterium concentration at the level of 10^{18} D/cm2. This results is consistent with the results previously obtained in [13] and suggests that the limits of detection do not suffer strongly due to the matrix effects. It can be explained by the mechanisms of the gaseous release which;

however; occurs due to desorption in the case of mixed layers and bond breaking + desorption in thick TEXTOR-like co-deposites, nevertheless both mechanisms are effective enough to release all fuel particles from laser-treated volumes.

To verify how aging can influence the contents of the hydrogen isotopes retained in the WAIC layers, the experiments have been reproduced at the IPPLM after approx. 8 months with the use of a standard - single pulse LIBS and DP-LIBS in a joint experiment with the ENEA Frascati team (iii). The experiments showed that application of the DP-LIBS can enhance the SNR of the acquired signals and moreover, it can be optimized for the detection of a given light-emitting element.

The experiments on the measurements of the hydrogen isotopes contents in WAIC and bulk samples showed the decrease in the contents in the WAIC samples (the deuterium/hydrogen signal was very close to the noise) while for the bulk tungsten substrate the amplitude of the H signal was very similar to that obtained in the previous series of the experiment. It suggests that the WAIC layers, in terms of the hydrogen isotopes retention, behave differently than top surface of a bulk substrate in a way that it enhances of the gas release. It is also worth to notice, that it somehow 'protects' the top surface of the substrate layer from absorbing hydrogen isotopes, as the experiments showed that their contents on the uncovered surface is lower than on the surface of bulk tungsten without the layer.

The experiments in the dual pulse configuration shown that in this operation regime the SNR can be better in the standard operation and the delay time and frame may be adjusted for observation of given species.

Conclusion and summary

The reported works were a part of a significant programme which proved that LIBS is an efficient technique for the layer characterization for the next-step tokamak reactors. In the particular project it was shown that the LIBS technique is flexible enough to be adopted on the basis of the existing LIDAR system on JET. This output is a very optimistic prognostic for the further performance of the LIBS technique on the next-step ITER-like reactots,

References

- [1] G.F. Matthews et al., Phys. Scr. T145 (2011) 014001.
- [2] Roth J et al 2008 Plasma Phys. Control. Fusion 50 103001
- [3] S. Brezinsek et al., Fuel Retention Studies with the ITER-like Wall in JET, EX/4-1, 24th IAEA Fusion Energy Conference, 2012, San Diego, USA
- [4] A.Huber, B. Schweer, V. Philipps, N. Gierse, M. Zlobinski, S. Brezinsek, W. Biel, V. Kotov, R. Leyte-Gonzales, Ph. Mertens, U. Samm Development of laser-based diagnostics for surface characterisation of wall components in fusion devices, Fusion Engineering and Design Volume 86, Issues 6–8, October 2011, Pages 1336–1340, doi:10.1016/j.fusengdes.2011.01.090
- [5] M. Zlobinski, V. Philipps, B. Schweer, A. Huber, H. Stoschus, S. Brezinsek, U. Samm and the TEXTOR-Team, PFMC-Konferenz, "In situ Measurements of Fuel Retention by Laser Induced Desorption Spectroscopy (LIDS) in TEXTOR", Phys. Scr. T145 (2011) 014027
- [6] A. Huber, B. Schweer, V.Philipps, R. Leyte-Gonzales, N. Gierse, M. Zlobinski, S. Bre-zinsek, V. Kotov, Ph. Mertens, U. Samm, G. Sergienko, PFMC-Konferenz, "Feasibility study of Laser-Induced Breakdown Spectroscopy for in-situ Characterisation of Deposited Layers in Fusion Devices", Phys. Scr. T145 (2011) 014028 (5pp)
- [7] C. Grisolia, et al., J. Nucl. Mater. 363–365 (2007) 1138.
- [8] N. Gierse, S. Brezinsek, T. F. Giesen, A. Huber, M. Laengner, S. Möller, R. Leyte-Gonzales, L. Marot, E. Meyer, M. Naiim-Habib, V. Philipps, A. Pospieszczyk, G. Sergienko, B. Schweer, M. Zlobinski,

- U. Samm and the TEXTOR Team, "Characterisation of hy-drocarbon and mixed layers in TEXTOR by Laser Induced Ablation Spectroscopy," Phys. Scr. T145 (2011) 014026 (4pp)
- [9] B. Schweer et al., "Laser techniques implementation for wall surface characterisation and conditioning," Phys. Scr. T138 (2009) 014008 (7pp)
- [10] B. Schweer et al, Journal of Nuclear Materials 390–391 (2009) 576–580
- [11] M. Zlobinski et al., "Laser Induced Desorption on plasma generated wall coatings", 9th Carolus Magnus Summer School on Plasma and Fusion Energy Physics, Herbeumont-sur-Semois, Belgium, 31/08/2009-11/09/2009
- [12] G. Sergienko et al., 31st EPS Conference on Plasma Phys. London, 28 June 2 July 2004 ECA Vol.28G, P-1.116 (2004)
- [13] P. Gąsior et al, Fusion Engineering and Design, Vol. 86, (2011),1239–1242

2.4 JET and ASDEX UG activities

High Power ICRH operation with metallic plasma facing components

Principal investigator:
A. Czarnecka; <u>agata.czarnecka@ipplm.pl</u>
Institute of Plasma Physics and Laser Microfusion

Introduction

The high-Z impurities need to be controlled within tolerable limits, to ensure they do not significantly affect the performance of the plasma. This requires the mitigation of impurity generation by ICRF heating, improving the understanding of RF sheaths effect. This include acting on sheaths by appropriate edge plasma / neutral gas pressure modifications, e.g. by gas injection. During the ICRF operation in high-Z machines, such as the full tungsten (W) ASDEX Upgrade (AUG) the impurities released from the wall contributes to radiation losses from the plasma. Experimental data from AUG allowed characterization of the processes participating in the ICRF specific plasma wall interaction, which need to be understood in order to maximize ICRF power in ITER.

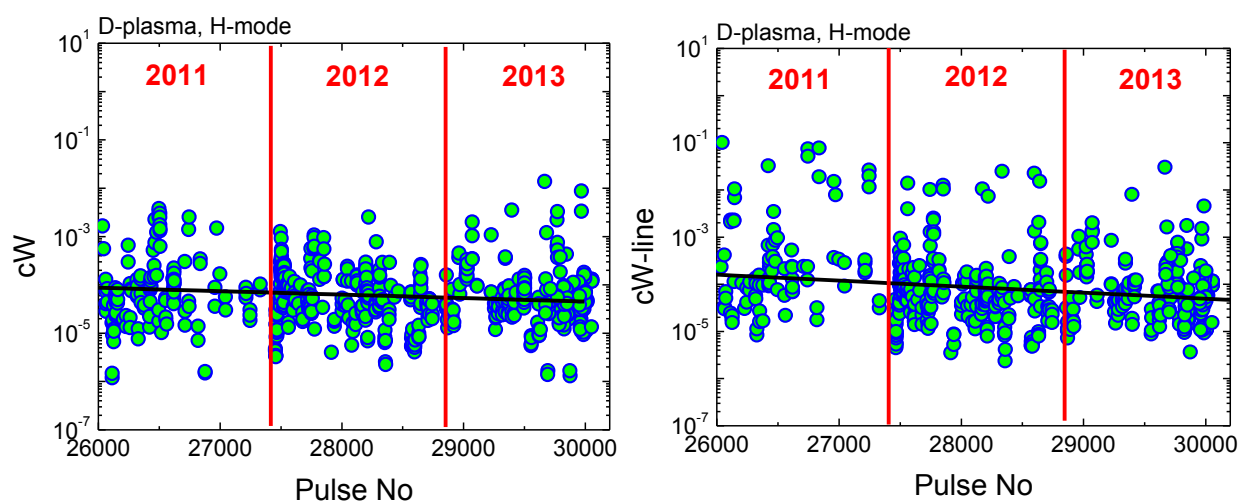
Experimental arrangement

ASDEX-Upgrade is a divertor tokamak with a full-tungsten first wall with $R_{maj} \sim 1.65$ m, $R_{min} \sim 0.5$ m, $B_T < 3.1$ T, $I_p < 1.6$ MA and pulse duration < 10 s. AUG has an ICRH system with four antennas, known as antenna a1, a2, a3, and a4. Each antenna comprises two straps which are normally configured with a (0 p) strap phasing. From the experimental campaign in 2012, the side limiters of a1 and a2 antenna were coated by a 50 2m thick layer of boron. Both antennas a1 and a2 with the boron-coated limiters were connected as a pair within the 3dB hybrid connection scheme, whereas a3 and a4 were connected as the other pair. This allowed a discrete operation of the antennas with the boron-coated limiters and of the antennas with the W-coated limiters. It was previously observed that the implementation of boron coatings on the ICRF antenna limiters reduced W release during ICRF [1-2].

Tungsten content was diagnosed by passive spectroscopy in the vacuum ultraviolet (VUV) range. Analysis based on the spectroscopic observations of W quasi-continuum and lines radiation. The quasi-continuous spectral features of tungsten around $\mathbb{Z}=5$ nm (W²⁷⁺ – W³⁵⁺) and line radiation emitted by ionization stages up to W⁴⁵⁺ is used routinely in AUG for tungsten concentration measurements [2]. For all analyzed discharges effective tungsten yield (Y_{eff}), defined by ratio of W and deuterium influxes was calculated. Tungsten influx was monitored by measuring WI line radiation at 400.8 nm, whereas the deuterium influx by the Balmer- \mathbb{Z} transition at 410.1 nm. The measured photon fluxes were transformed into ion fluxes using the number of ionisations per emitted photon, i. e. the (S/XB) value. The evaluation of the tungsten influx depended on the ratio of ionization rate to excitation rate times the branching ratio (S/XB). For tungsten (S/XB) = 20 was used. For deuterium, the atomic value (S/XB) = 3.3 · 10³ was multiplied by a factor of 1.5 as a rough estimate for the molecular flux contribution. The Y_{eff} was measured at a3 and a4 ICRF antennas.

Experimental Results

To complete long-term observation of W concentration in H-mode deuterium plasmas produced in tokamak AU concentration was calculated for the discharges with ICRF heating in use in experiments carried out in 2013. Figure 1 and 2 are showing behaviour of W concentration calculated from the



quasi-continuum and lines radiation, respectively for all ICRH discharges since campaign in 2011.

Fig. 1. Tungsten concentration in H-mode deuterium plasma in AUG, determined from the quasi-continuum radiation vs. pulse No. with ICRF in 2011-2013 experimental campaign.

Fig. 2. Tungsten concentration in H-mode deuterium plasma in AUG, determined from the line radiation vs. pulse No. with ICRF in 2011-2013 experimental campaign.

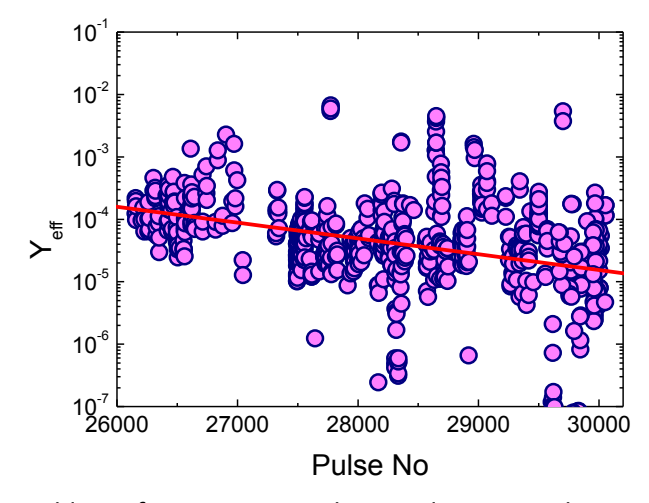


Fig. 3. Effective tungsten yield as a function AUG pulse No. during ICRF heating.

Long-term observation of W in AUG plasma during ICRF heating showed small reduction of the C_W and the Y_{eff} as is presented in Fig. 3. Most of the pulses were with ICRH power 2 or 4 MW. Although there is a considerable scatter in the data. This is attributed to the several additional parameters that also play a role when relating the level of W in the plasma to the ICRF operation. In the second step, the effect of different gas injection on W release during ICRF has been investigated. It turned out that the effect of gas injection have beneficial effect on the ICRF plasma performance. The stress was put mainly on the selected pulses with the injection of deuterium (D_2) gas, D_2 with nitrogen (N_2), argon (Ar) and krypton (Kr). Figure 4 is showing W concentration as a function of deuterium injection rate for ICRH and NBI discharges. W concentration decreased strongly with increasing deuterium gas puff, but higher level was found in ICRH than in NBI heated discharges. However, effective W yield was the same in both cases (Fig.5), suggesting stronger effect of ICRF heating on core W contamination. Y_{eff} in was measured at non-powered ICRF antennas.

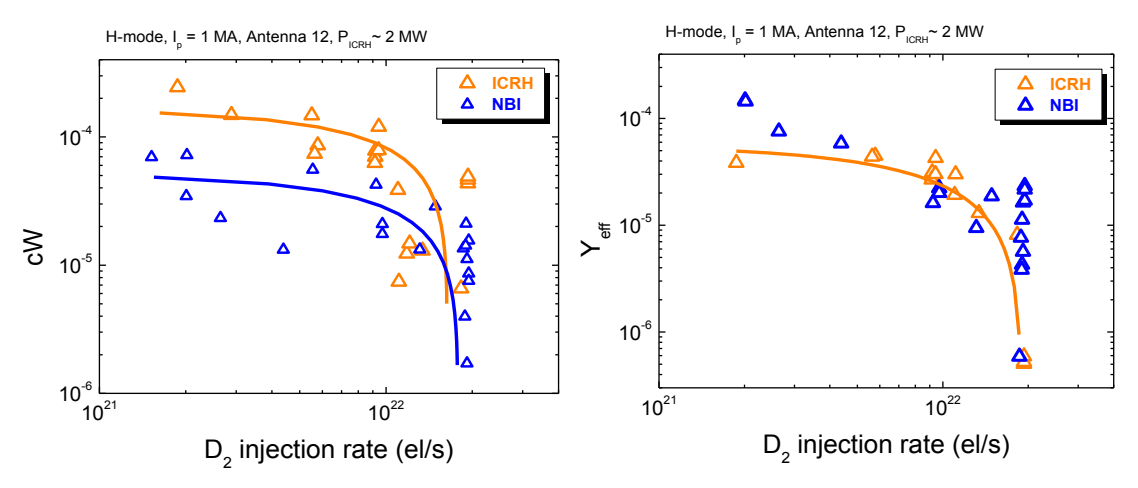


Fig. 4. Influence of D_2 injection rate on W concentration determined from the quasi-continuum radiation during ICRF and NBI heating.

Fig. 5. Influence of D_2 injection rate oneffective W yield during ICRF and NBI heating.

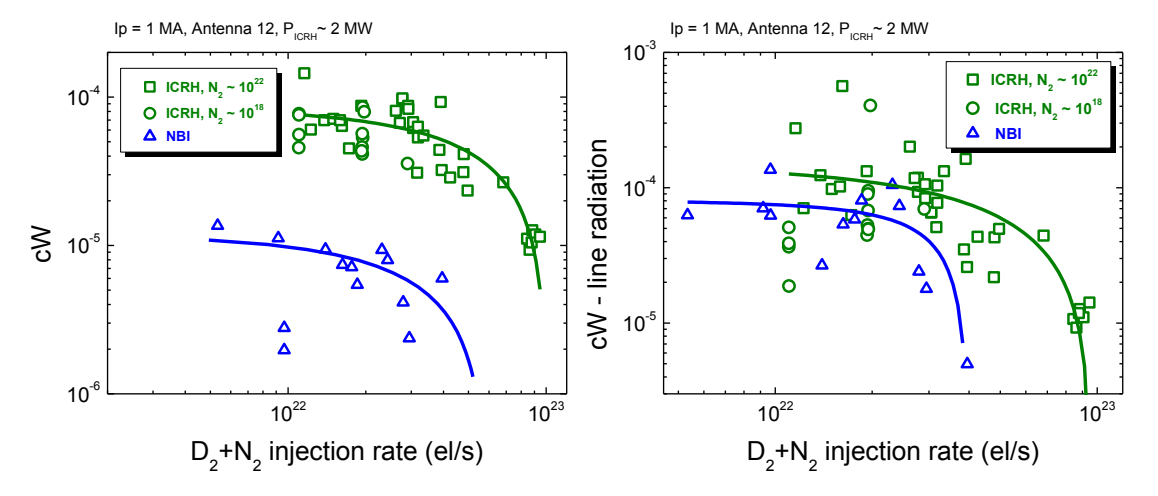


Fig. 6. Tungsten concentration determined from the quasi-continuum radiation vs. total D_2 and N_2 injection rate for ICRF and NBI heated plasmas.

Fig. 7. Tungsten concentration determined from the line radiation vs. total D_2 and N_2 injection rate for ICRF and NBI heated plasmas.

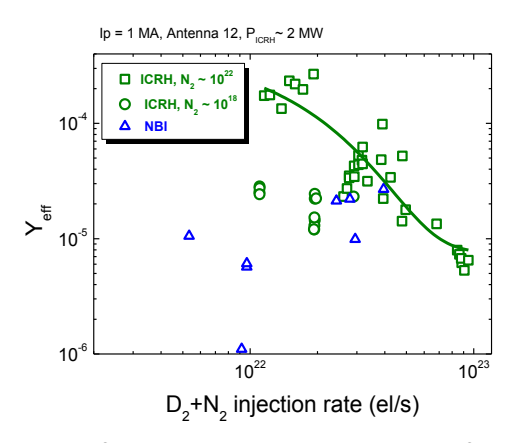
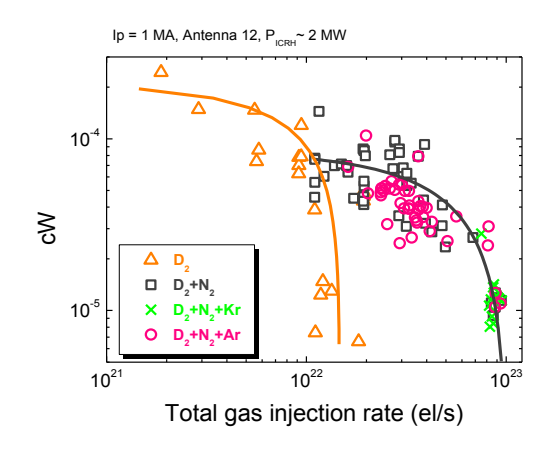


Fig. 8. Effective W yield as a finction of total D₂ and N₂ injection rate for ICRF and NBI heated plasmas.

When beside deuterium also nitrogen was introduced to plasma, W concentration decreased with the total gas injection rate. It was observed that NBI-heated plasmas were characterized by lower W

content as is presented in Fig. 6 and 7. Figure 8 shows sputtering yield vs. sum of D_2 and N_2 injection rate for ICRH and NBI discharges. It was observed that during NBI, the W effective yield was smaller. Similar effect has been observed with additional Ar and Kr gas puff as is presented in figures 9-11. However, minimum of W concentration was obtained for different gas injection level that for discharges with pure deuterium. The same effect has been observed for NBI-heated plasma (Fig. 12).



Ip = 1 MA, Antenna 12, P_{ICRN} 2 MW

10³

10⁴

D₂

D₂+N₂+Kr

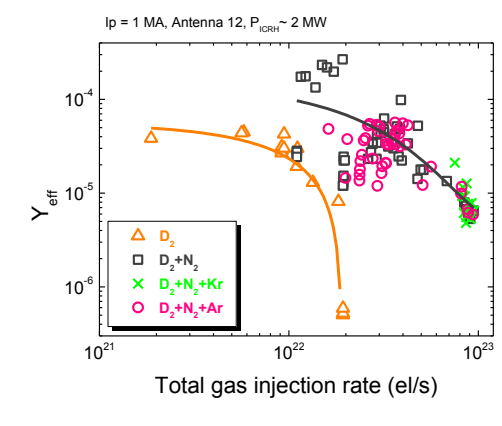
O D₂+N₂+Ar

10²¹

Total gas injection rate (el/s)

Fig. 9. Tungsten concentration determined from the quasi-continuum radiation vs. different mixture of gases injected to plasma with ICRF.

Fig. 10. Tungsten concentration determined from the line radiation vs. different mixture of gases injected to plasma with ICRF.



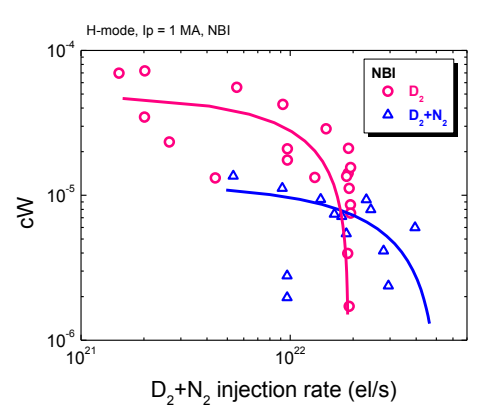


Fig. 11. Effective W yield vs. different mixture of gases injected to plasma with ICRF.

Fig. 12. Tungsten concentration determined from the line radiation vs. D_2 and mixture of D_2 and N_2 injection rate for NBI heated plasmas.

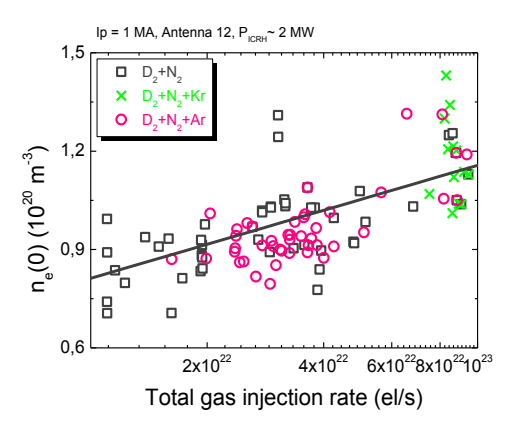


Fig. 13. Impact of injection diffrent gases to plasma on core electron density.

Reduction of central W impurity concentration with different gas puffs during additional heating is corellated with modification of plasma density. Figure 13 is showing core electron density as a function different gas mixture injection. Electron density is incereasing with gas puff. It was also observed that during ICRH, W effective yield increased when percentage contrubution of N_2 , Ar and Kr to deuterium increased (see Fig. 14). Figure 15 is presenting W content for the percentage contrubution of diffrent gases. Higher contribution of N_2 did not incerease core W concentration.

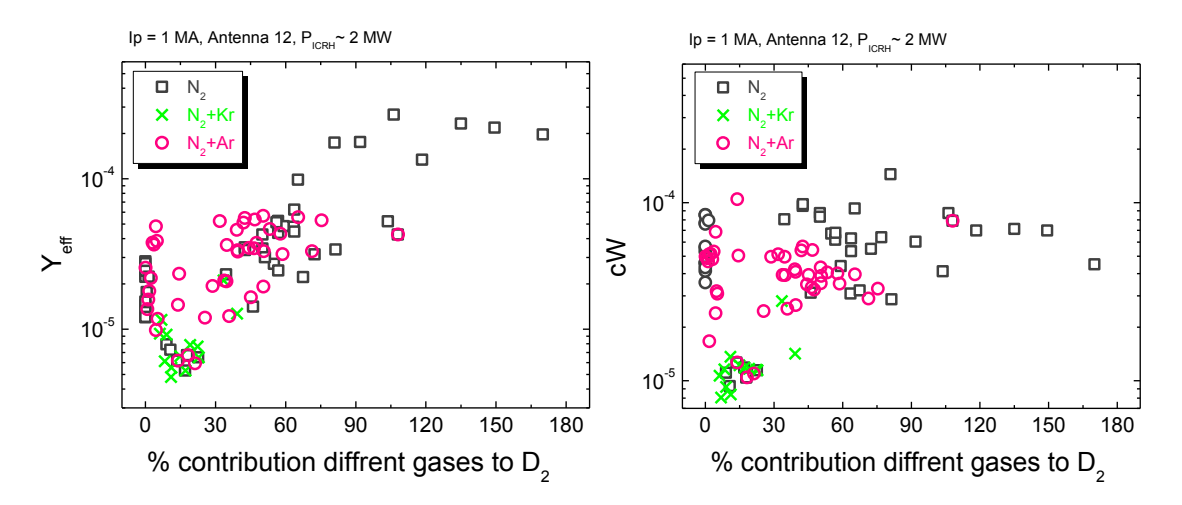


Fig.14. Effective W yield vs. percentage contribution of different gases to D₂.

Fig.15. Influence of percentage contribution of different gases to D_2 on W concentration determined from the quasi-continuum radiation.

Conclusions

The conducted research allows to state that operation of ICRF antennas in magnetic fusion experiments is often accompanied by enhanced plasma-surface interactions. Long term spectroscopic observations indicated slow reduction of the core W concentration in the AUG plasma during ICRH operation. The effect of gas injection seems to have beneficial effect on the ICRF plasma performance. The C_W decreased with the increasing of D_2 injection rate. Higher level was found in ICRF than in NBI heated discharges. Regardless of the type of the gas mix, the C_W decreased with the total gas injection rate, which was also correlated with the increasing of core electron density. Addition of N_2 , Ar and Kr had impact on $Y_{\rm eff}$ increase, wherein the core W content was lower. Similarly, in this cases lower level of C_W was found in NBI heated discharges. Firstly the reduction of W impurity realize to plasma core was the implementation of boron coatings on the ICRF antenna limiters.

Minimisation of heavy impurity sputtering and local heat loads by optimisation of plasma edge and reduction of ICRF sheaths operation needs to be investigated. Gas puff technique to maximise ICRF power in H-mode with reduced W source need to be developed. The influence of the location of the gas inlets and edge plasma modification on W sputtering during ICRF operation needs to be investigated. For AUG are planned experiments with a new antenna with the aim to minimize the antenna near fields for a reduction of the W sources. Minimisation of ICRF sheaths effects by modifications ICRF antenna parameters can be achieved.

Collaboration

Association EURATOM –Max-Planck-Institut für Plasmaphysik, D-85748 Garching, Germany

References

[1] V. Bobkov et al., Nucl. Fusion 53 (2013) 093018 (9pp)

- [2] V. Bobkov, R. Bilato, L. Colas, A. Czarnecka, R. Dux, H. Faugel, P. Jacquet, A. Kallenbach, I. Monakhov, H. W. Mueller, J-M. Noterdaeme, S. Potzel, Th. Puetterich, I. Stepanov, W. Suttrop, ASDEX Upgrade team, "Influence of Gas Injection Location and Magnetic Perturbations on ICRF Antenna Performance in ASDEX Upgrade", 20th Topical Conference on Radio Frequency Power in Plasmas, Sorrento, Italy, 25-28 June 2013
- [3] T. Pütterich et al., Plasma Phys. Control. Fusion 50 (2008) 085016.

Algorithm development of Ni and W data processing

Principal investigator:

K. Jakubowska; <u>katarzyna.jakubowska@ipplm.pl</u>
Collaborators from the Institute of Plasma Physics and Laser Microfusion:
M. Chernyshova, A. Czarnecka, M. Kubkowska, J. Rzadkiewicz, R. Zagórski

Introduction

The investigation of X-ray emission from fusion plasmas has become a standard diagnostic tool used in many different fusion experiments. The measurements of X-ray emission performed with KX1 diagnostic at JET delivers information on plasma core properties (the ion temperature or density) and dynamic (the rotational velocity). Recently the KX1 spectrometer at JET was upgraded with two new generation Gas Electron Multiplier (GEM) detectors that register radiation in soft X-ray range. One of the detectors provides high sensitivity for detection of the nickel radiation around 7.8 keV (Ni²⁶⁺) second one is collecting the data related to the tungsten radiation around 2.4 keV (W⁴⁶⁺). Both detectors were delivered by the IPPLM institute. Development of the algorithm leading to Ni and W data processing was leading to determination of the intensity, FWHM (Full Width at Half Maximum) and wavelength in maximum of the peak of the detected radiation.

Algorithm description

During the C30-C32 campaigns at JET the X-ray spectra around 2.4 keV and 7.8 keV were measured across the whole accessible range of the wavelengths for KX1 spectrometer. Performed action was supposed to prove availability of spectral lines in the vicinity of 2.4 keV and let to define optimum settings of the spectrometer for which covered wavelength range is the most rich in characteristic radiation of interest (for spectra around 2.4 and 7.8 keV).

Technical problem related to usage of several carriers caused deformation of the signal at the beginning and at the end of each carrier's. As a first step of the code correction of acquired data was performed by averaging signal of the second and 15th channel for each carrier. The line of sight of registered radiation crosses tokamak a few cm below equatorial plane. The size of the detector (~10x20cm²) and its position leads to the measurement in which part of the measured radiation passes the vacuum vessel only once and the rest of the radiation passes the vacuum vessel twice. It was taken into account in the data analysis via linear approximation of the vignetting curve (representing signal without characteristic radiation). The wavelength range of the measurement was defined by the crystal settings, which together with spectrometer settings were provided as an input parameters for the code. As a next step Gaussian fit of each peak was performed and from the Gaussian fit of each peak the intensity, FWHM and wavelength were obtained.

Conclusions

Comparison of the data acquired with GEM detector sensitive for tungsten radiation with the data provided by SXR diagnostic at JET shows the same trend (Fig. 1).

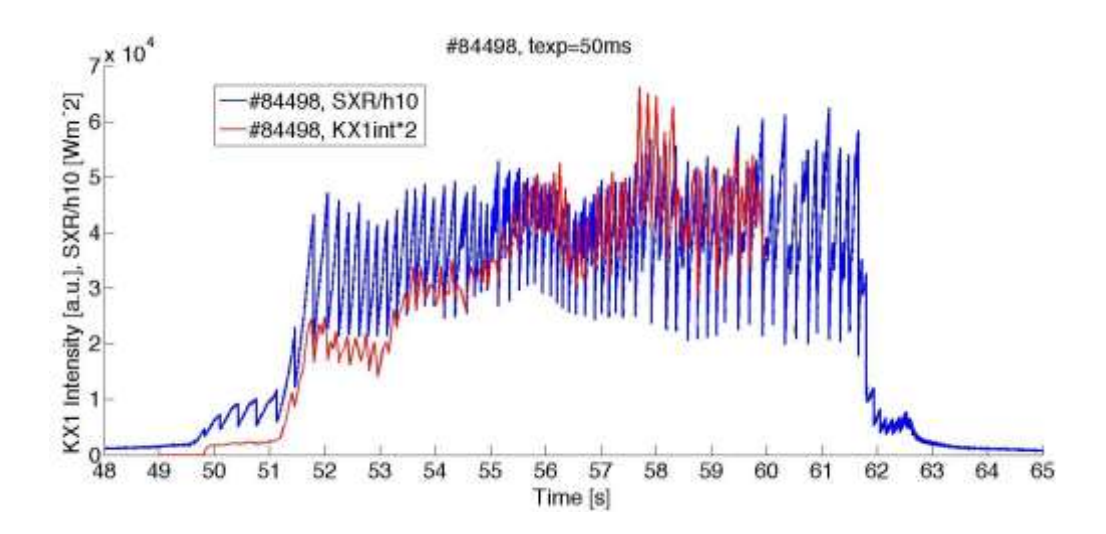


Fig. 1. Comparison of the data acquired with GEM detector sensitive for tungsten radiation with the data provided by SXR diagnostic at JET.

Collaboration

Association EURATOM – JET, Culham, UK.

Calibration of the JET KT2 spectrometer

Principal investigator:
A. Czarnecka; <u>agata.czarnecka@ipplm.pl</u>
Institute of Plasma Physics and Laser Microfusion
I. Książek
Institute of Physics, Opole University

Introduction

Spectroscopy is a key diagnostic for identification and monitoring of impurities in fusion plasmas. Impurity ions with different charge states are monitored by means of a Princeton Instruments SPRED [1] spectrometer, known in JET as KT2 diagnostic [2]. The spectrometer typically registers VUV spectra in the wavelength range of 100–1100 Å with a spectral resolution of ~5 Å. The detector consists of a microchannel plate coated with CuI and a phosphor coupled by a fibre optic bundle to a 2048 photodiode array. The instrument is situated outside the torus hall, at a distance of 22 m from the plasma (see Fig.1a). The line of sight (see Fig. 1b), is along the vessel midplane via a spherical mirror (Au coating) with an angle of incidence of 75°.

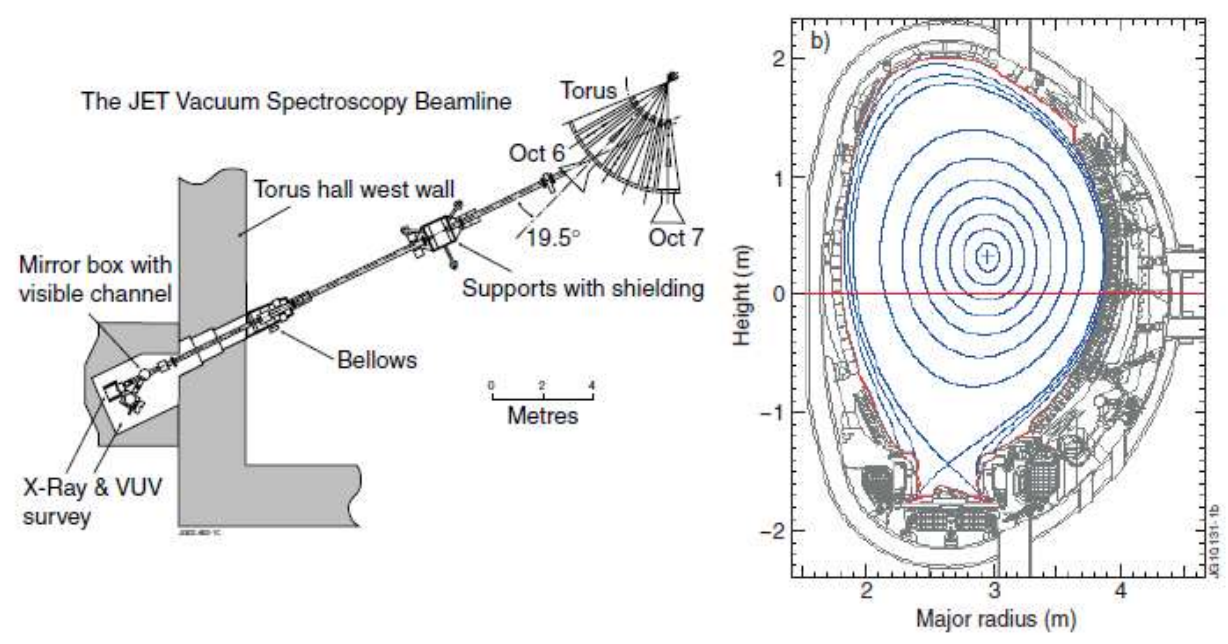


Fig. 1. (a) JET installation of the KT2 VUV spectrometer, (b) I-o-s of the diagnostic [3].

With the former carbon plasma-facing components (PFCs) the VUV spectrum was dominated by different mid-Z metallic impurities like Ni, Fe, Cr, Cu. Note that with the new ITER-like wall (ILW) that consists of a full W divertor, beryllium (Be) main chamber (PFCs), and a small fraction of W-coated CFC protection tiles in recessed areas, the spectrum also contained intense W features. For diagnostics such as KT2, used routinely on JET machines, which have long periods of operations with little intervention possible, it is necessary to monitor the stability of the sensitivity throughout the periods of operations. In order to fully exploit the line intensity measurements for pulses with ILW, recalibration of KT2 spectrometer was performed. As shown by Lawson et al. [4], for this instrument it is possible to derive accurate sensitivity calibrations using in situ methods and these are adopted here. They involve the use of line ratios to obtain a relative sensitivity curve and branching ratios from a calibrated visible spectrum to obtain the absolute calibration.

The calibration method of KT2 VUV spectrometer in experiments with ITER-like wall is presented. The relative calibration at short wavelengths was performed using a number of Na- and Li-like metal doublets. At longer wavelengths, the Li-like doublets of Ar and Ne have been used. The stability of the KT2 relative calibration curve is discussed. The absolute sensitivity was being calculated from branching ratios to an absolutely calibrated visible spectrometer. However, it was associated with some presented difficulties.

Relative calibration of KT2 spectrometer

The Na- and Li-like doublets of a number of intrinsic metallic impurities can dominate the short wavelength of the VUV spectrum. The doublets correspond to the $2p^63s\ 2S_{1/2} - 2p^63p\ 2P_{1/2,3/2}$ and $1s^22s\ 2S_{1/2} - 1s^22p\ 2P_{1/2,3/2}$ transitions. As was mentioned earlier, spectrum detected by KT2 diagnostic shows intense Ni, Fe, Cu, and Cr lines. An elements such as Zr and Mo can be introduced into the plasma by laser ablation and the noble gases N, Ne, Ar by gas puffing. A careful selection of the available data was necessary in order to give reliable measurements. Therefore, in the first step IDL program for searching list of pulses with possible calibration data was developed. The code is using the position of the Be IV line in limiter phase, as a reference position for 2048 pixels in detector. Searching of data was done for Ni XVIII, Ni XXVI, Fe XVI, Fe XXIV, Cu XIX, Cu XXVII, Ar XVI, Al XI, Ne VIII in the range of JET Pulse No's 80632-83750, covering all available ILW data. To obtain measurements of the line intensity, a simple and reliable line integration technique was used, in which Simpson's rule is applied to the area defined by a certain number of pixels on either side of the line centre, these pixels also defining the background to be subtracted. With 2048 pixels,

an integration range covering ±5 pixels from the line centre was regarded as the best compromise between minimizing blending and using a sufficient proportion of the line profile to ensure reliable measurements. For the selected pulses, experimental ratios of Li- and Na-like doublets were calculated. In the next step a comparison of a measured spectral line intensity ratio with the theoretical result from the collisional-radiative population model was made. This allows the sensitivity at two wavelengths to be related. By comparing the measurements with the modelled line intensity ratio, a ratio of the sensitivities at the doublet wavelengths was derived. Most of the wavelength intervals covered by the doublets overlap. Where the ratios overlap, the sensitivity of the intermediate wavelength is found by interpolating the logarithm of the sensitivity, this allowing the calibration to be extended to lower or higher wavelengths. Table 1 give comparisons for the Na- and Li-like doublet lines of the modeled and measured intensity ratios, together with the derived inverse sensitivity ratios. The derived relative inverse sensitivity curve (S1 at 312.4Å = 1) is presented in Fig.2.

Table 1. Na- and Li-like line intensity ratios used in the derivation of the sensitivity calibration for KT2.

lon	Wavelenght [A]	Modelled intensity ratio	Measured Intensity ratio - CFC	Measured Intensity ratio – ILW	Inverse sensitivity ratio-CFC	Inverse sensitivity ratio-ILW
FeXVI	335.4 / 360.8	1.95	1.99±2.1%	2.07±8%	0.978	0.942
NiXVIII	292.0 / 320.6	1.94	1.96±4.1%	1.94±3%	0.989	1.000
ArXVI	353.9 / 389.1	1.97	2.68±8.1%	2.089±7.5%	0.736	0.943
FeXXIV	192.0 / 255.1	1.91	2.17±2.3%	2.09±7.8%	0.881	0.914
NiXXVI	165.4 / 234.1	1.88	2.00±5.7%	0.99±18.2%	0.942	1.95
CuXXVII	153.5 / 224.7	1.87	1.99±3.2%	1.03±12.5%	0.940	1.82
AIXI	550.03/568.15	2.01	no data	1.99±6.4%	no data	1.010
Mo XXII	127.9/176.6	1.82	1.78 ±2.2%	0.51	1.021	3.56
Zr XXX	142.9 / 189.6	1.84	1.91 ±3.0%	0.52	0.965	3.53
NeVIII	740.4/780.3	2.02	2.18±4.6%	2.025±2.2%	0.928	0.997

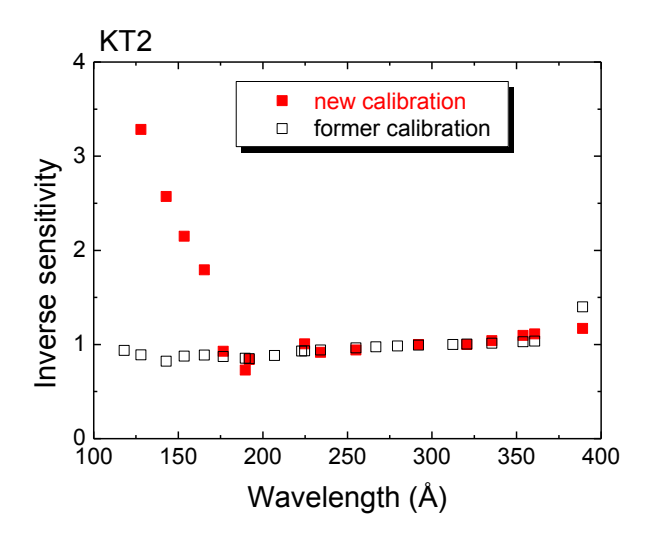


Fig. 1 The relative inverse sensitivity calibration at short wavelengths derived from Na- and Li-like doublet ratios (S-1 at 312.4Å = 1).

Absolute calibration of KT2 spectrometer

The absolute sensitivity calibration was being calculated in-situ, by using C branching ratios to crosscalibrate with an absolutely calibrated visible spectrometer (KS3H) with a horizontal line of sight along the same beamline used by the SPRED instrument. Transitions considered for branching ratio measurement are presented in table 2.

Table 2. Transitions used in the C IV branching ratio measurement.

Wavelength (Å)	Transition	Transition probability
312.42	$1s2s^2S_{1/2} - 1s3p^2P_{3/2}$	4.63·10 ⁹
312.45	1s2s ² S _{1/2} – 1s3p ² P _{1/2}	4.63·10 ⁹
5801.31	1s3s ² S _{1/2} – 1s3p ² P _{3/2}	3.17·10 ⁷
5811.97	$1s3s^{2}S_{1/2} - 1s3p^{2}P_{1/2}$	3.16·10 ⁷

It turned out that the calibration accuracy of the KS3H visible spectrometer which was used for the branching ratio calibration of KT2, has also been in question. This prevented completion of the task. After the introduction of the ILW into JET, KS3H was calibrated using an in-vessel light source. However, before any suitable pulses for a calibration were obtained the spectrometer setup was changed meaning that there was again uncertainty about the KS3H calibration. Later on a smaller CCD chip was used in the KSRA spectrometer, which is used to derive the KS3H signals. This restricted the spectral range and meant that the C IV lines at 5801Å and 5812Å, which had routinely been used to calibrate KT2, were no longer observed. The reduction in the C levels in the JET-ILW plasmas also impacted on the ease with which a branching ratio calibration could be carried out from the C IV branching ratio. The visible C IV lines at 5801Å and 5812Å were only occasionally observed and then always in transient events. This led to an investigation of other possible branching ratios. Work on the calibration are in progress.

Conclusions

A sensitivity calibration for the JET KT2 spectrometer has been presented. The relative calibration at short wavelengths has been derived by comparing measured and modeled Na- and Li-like metal line intensity ratios. It was observed that the KT2 spectrometer loss it sensitivity in short wavelength range. Work on absolute calibration are continued.

Collaboration

Institute of Physics, Opole University, Opole

I. Książek

EFDA - JET, Culham Science Centre, United Kingdom Association EURATOM – CCFE, Culham, United Kingdom

References

- [1] Fonck R J et al 1982 Appl. Opt. 21 2115
- [2] Coffey I H et al 2004 Rev. Sci. Instrum. **75** 3737
- [3] Czarnecka A et al 2011 Plasma Phys. Control. Fusion 53 035009
- [4] Lawson K D et al 2009 JINST 4 P04013

2.5 Inertial fusion energy "keep-in-touch" activity

The interferometric studies of the pre-plasma influence on the laser energy transfer to the shock wave with the use two-layers planar targets

Principal investigator:
T. Pisarczyk; <u>tadeusz.pisarczyk@ipplm.pl</u>
Collaborator from the Institute of Plasma Physics and Laser Microfusions:
J. Badziak, S. Borodziuk, T. Chodukowski, Z. Kalinowska, A. Kasperczuk

Introduction

In the shock ignition (SI) concept [1, 2], energy transfer by fast electrons into the plasma with supercritical density can provide an ablation pressure of several hundred Mbar which is necessary for igniting shock generation [3, 4]. The recent experiments with OMEGA laser [5, 6] have demonstrated an increasing efficiency of the energy transfer to both planar and spherical targets resulting from a contribution of the fast electrons generated due to stimulated Raman scattering and two-plasmon decay in an extended pre-plasma.

This paper extends our previous research [7, 8] performed on the PALS laser facility in which the planar Al and Cu massive targets were irradiated by the 1ω or 3ω PALS beams. The experimental and theoretical investigations allow to conclude that [8] in the case of 1ω and intensities of 10-50 PW/cm², the dominant ablation mechanism is heating the supercritical plasma by fast electrons generated by resonant absorption. For the maximum laser energy of 580 J and intensity of 50 PW/cm², the ablative pressure reaches about 180 Mbar in spite of two-dimensional expansion of the target corona. However, for 3ω the ablation pressure originates from the thermal electron conductivity heating, and its value of about 50 Mbar is several times lower in comparison with the 1ω case. As the next step of these studies the CHPP influence on the ablation and the energy conversion efficiency to the shock wave are presented below.

The interferometric measurements of the CH pre-plasma (CHPP) influence on the efficiency of the laser radiation energy transportinto the shock wave generated in a solid target were carried out at PALS (Prague Asterix Laser System). Two-layer planar targets, consisting of a massive target made of Cu and CH thin layer, were applied. The targets were irradiated by two laser pulses accordingly to the shock ignition (SI) concept. The 1st harmonic (λ_1 = 1315 nm) moderate-intensity (~10¹⁴ W/cm²) pulse was used, which compresses a DT plasma in the SI scenario. The 1st or 3rd harmonic (λ_3 = 438 nm) high-intensity (~10¹⁵-10¹⁶ W/cm²) pulse generated a shock wave, corresponding to the igniting shock in SI. To determine the energy transfer from a laser beam to the target, the crater volume measurements were performed. The measurements using these two diagnostics enabled us to determine the pre-plasma influence on the fast electrons contribution into the transport energy to the solid target. It is shown that the pre-plasma strongly influences the investigated process in the case of using the 1 ω pulse for the shock generation while this influence is insignificant in the case of using the 3 ω pulse.

Experimental set-up and results

The planar layered targets consisting of the massive Cu layer and 25 μm thick layer of the CH were irradiated using two laser pulses, accordingly to the SI concept. The 1ω beam, with energy of 50 J, produced CHPP. The 1ω or 3ω beam with energy about 200 J generated the spike-driven shock wave. The focal spot radii R_L varied in the range 40-160 μm . The delay between the auxiliary and the main laser beams was $\Delta t = 1.2$ ns.

The influence of the pre-plasma on parameters of the shock wave was determined by the crater volume measurements technique (see, for example [9, 10]). and from the electron density distributions measured by 3-frame interferometry. The interferograms were registered 2 ns after the second main laser pulse maximum. This registration time seems to be optimum since the absorption processes of the laser radiation in the ablative plasma terminated already.

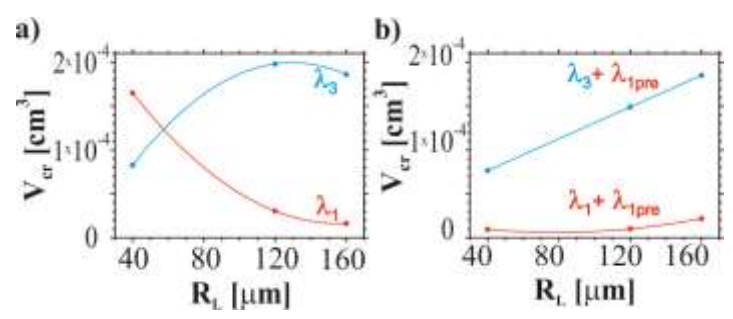


Fig. 1. Dependencies of the crater volume as a function of the focal spot radius: (a) without and (b) with the pre-plasma.

Fig. 1 presents photographs of craters formed on the surface of the target in the case of absent (Fig. 1a) and presence (Fig. 2b) of the CHPP for two wavelength and different focal spot radii (R_1).

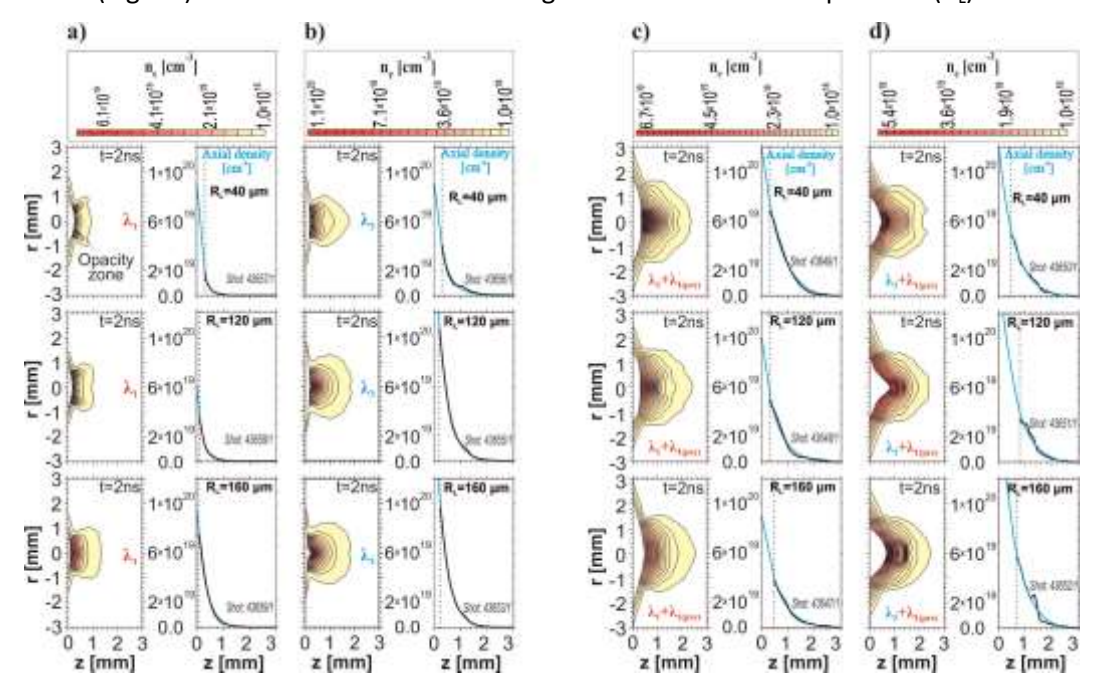


Fig. 2. The equidence and axial profiles of the electron density obtained in the absence of the preplasma in the case of: (a) 1ω and (b) 3ω and in the presence of the pre-plasma in the case of: (c) 1ω and (d) 3ω and different focal spot radii.

The comparison of the crater volumes V_{cr} obtained for two wavelengths and different focal spot radii in the cases of absence and presence of the CHPP is shown in Fig. 1c and 1d, respectively. Without the CHPP (Fig. 1c) the dependences of the V_{cr} on the R_L obtained for two wavelength are very similar to these from the paper [7, 8] (for Cu massive targets). So, for 3ω pulse at the predominant inverse bremsstrahlung absorption, the crater creation efficiency reduces with the decreasing R_L due to the two-dimensional expansion effect. In contrast, for 1ω pulse the crater creation efficiency increases with the decreasing R_L which, according to the numerical simulations [8], directly corresponds to an energy transfer by fast electrons generated due to the resonant absorption. The strong influence of the CHPP on the crater creation process in the case of 1ω is clearly visible in Fig. 1d - the crater volume decreases

by more than one order of magnitude. It testifies the weakness of the fast electrons role (generated by resonant absorption) in the energy transport process. In the case of 3ω , the CHPP influences the crater formation process weakly and the V_{cr} value remains at the same level as in the case of the pre-plasma absence.

To better interpret the electron density distributions, the methodology of the maximum electron density gradient determination was implemented. The aim of this methodology was to obtain the some quantitative information about ablated plasma density gradient observed by interferometry, necessary to determine an influence of CHPP on forming of plasma stream related to a laser beam generating an igniting shock wave. The maximal axial gradient was derived from the approximation of experimental axial density profiles by the exponential function:

$$y = A_0 e^{-z/L} + y_0 (1)$$

The parameters of this function determine the maximal electron density gradient in the opacity zone: $[dy/dz]_{z=0} = A_0/L$, where: L- scale-length of density gradient, and A_0- the maximal electron density. The parameters on the basis of which the maximum gradient of the electron density was calculated, are presented in Table 1. The dependencies of the maximum density gradient on R_L for two harmonic and in the case of without and with CHPP are shown in Fig. 4. At the CHPP absence and 1ω (Fig. 4a), the maximum density gradient increases strongly with the decreasing R_L , while in the case of 3ω , the density gradient decreases with the decreasing focal spot radius. For R_L < 80 μ m, the density gradient scale-length of the ablative plasma created by means of the λ_1 beam is about 200 μ m and it is almost twice smaller in the comparison to plasma produced by λ_3 , see table 1. The decreasing of the maximum density gradient with increasing the focal spot radius in the case of λ_1 results from the smaller maximum electron density which is caused by the decrease of laser beam intensity.

Table 1. The parameters on the basis of which the maximum gradient of the electron density.

R_L	1 ω			3 ω				
[µm]	A/Lx10²¹ [cm ⁻⁴]	Ax10²⁰ [cm ⁻³]	L [μm]	A/Lx10²¹ [cm ⁻⁴]	Ax10²⁰ [cm ⁻³]	L [μm]		
Without pre-plasma								
40	5.7	1.0	180	3.0	0.9	330		
120	3.0	0.6	210	4.9	1.9	380		
160	2.9	0.9	320	5.1	1.9	370		
With pre-plasma								
40	1.9	1.3	667	2.8	1.2	613		
120	1.9	1.0	522	2.4	1.5	623		
160	1.6	0.9	583	3.39	2.0	596		

In the case of the CHPP presence (Fig. 3b) the constraint of the plasma radial expansion by the CHPP causes an elongation of the plasma stream. In the case of 3ω the CHPP constraint is stronger due to the axial character of expansion. The absorption of the main beam in the long, relatively cold pre-plasma occurs mainly by the inverse bremsstrahlung mechanism for both 1ω and 3ω radiation. Under these conditions, the heating is distributed in the area of a significant longitudinal size that leads to the decreasing axial density gradient as compared with the solid target irradiation. The CHPP reduces L for both wavelength above twice. Stronger refraction in the case of 1ω - in comparison to 3ω - leads to a stronger re-distribution of the absorbed energy in the lateral direction that is the reason for an additional decrease of the density gradient. The presence of the CHPP creates poor conditions for resonant absorption for the laser energy conversion to fast electrons. This results in suppression of the fast electrons contribution to the ablation process.

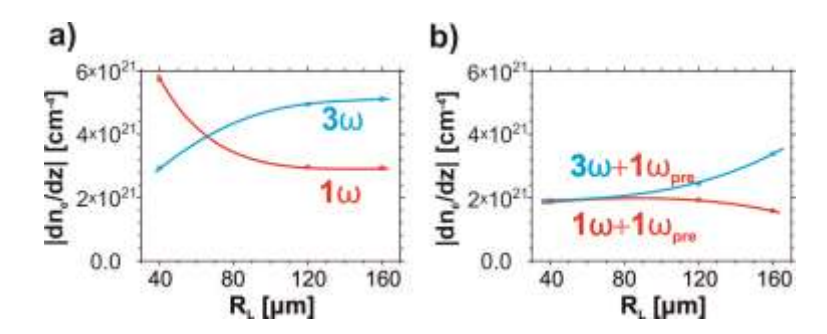


Fig. 3. The maximum density gradient for 1ω and 3ω of laser radiation in the absence (a) and the presence (b) of the pre-plasma.

Conclusions

The interferometric and the crater formation investigations of the two-layer targets directed to imitate the spike-laser interaction with the pre-produced plasma have shown the significantly decreasing efficiency of the 1ω radiation energy transmission to the solid part of the target in comparison with the case of CHPP absent. In previous experiments [8] with the single 1ω beam an enhancement of the energy transfer efficiency to the shock wave associated with the fast electrons energy transfer to the dense plasma region was demonstrated. In the presence of the CHPP, the significantly smaller effectiveness of the energy transfer to the dense plasma region by the high-intensity 1ω pulse is clearly seen from both the craters volumes and the density gradient data. Nevertheless, these two-beams experiments have not provided data indicating alteration of the fast electrons generation due to resonant absorption by any other mechanism connected with parametric instabilities in the CHPP.

Interesting conclusions can be formulated for the 3-harmonic. The interferometric results and the crater creation efficiency measurements, obtained both without and with CHPP, clearly suggest that the minimal focal spot radius is not optimum from point of view of the SI concept. Due to the two-dimensional expansion effect [8], the focal spot radius should be relatively large to minimize this effect. To explain this problem in detail, further investigations with the diagnostics which make the monitoring of the fast electrons emission (e.g. by measure of the K_{α} line from Cu) possible are required.

Collaboration

J. Ullschmied, E. Krousky, J. Skala, Inst. of Plasma Phys. ASCR, Prague, Czech Rep.

M. Pfeifer, K. Rohlena, Inst. of Phys., ASCR, Prague, Czech Rep.

S. Yu. Gus'kov, N. N. Demchenko, P. N. Lebedev Phys. Inst. (FIAN), RAS, Moscow, Russia.

References

- [1] Scherbakov V A 1983 Sov. J. Plasma Phys. 9 240
- [2] Betti R, Zhou C D, Anderson K S et al. 2007 Phys. Rev. Lett. 98 155001
- [3] Gus'kov S Yu, Zverev V V and Rozanov V B 1983 Quantum Electr.13 498
- [4] Gus'kov S, Ribeyre X, Touati M et al. 2012 Phys. Rev. Lett. 102 255004
- [5] Theobald W, Betti R, Stoeckel C et al. 2008 Phys. Plasmas 15 056306
- [6] Theobald W, Nora R, Lafon M et al. 2012 Phys. Plasmas 19 102706
- [7] Kalinowska Z, Kasperczuk A, Pisarczyk T et al. 2012 Nukleonika57 227
- [8] Gus'kov S Yu, Demchenko N N, Kasperczuk A et al. 2013 Laser Part. Beams (in press)
- [9] Gus'kov S Yu, Borodziuk S, Kalal M et al 2004 Quantum Electronics 34989
- [10] Margarone D, Laska L, Torrisi L et al. 2008 Applied Surface Science 254 2797

New, two-dimensional particle-in-cell code for simulation of the laser-induced cavity pressure acceleration (LICPA)

Principal invertigator:
S. Jabłoński; <u>slawomir.jablonski@ipplm.pl</u>
Institute of Plasma Physics and Laser Microfusion

Introduction

Particle-in-cell (PIC) codes are very attractive and usefull tools for kinetic simulations in plasma physics and astro physics. Especially in the case of interaction between high-intensity ($I_L > 10^{18} \text{W/cm}^2$) and short laser pulse ($\tau_L < 2$ ps) [1,2] with target high-precision is demanded for kinetic description of such a physical proccess. High intensities, short time scales and large density gradients, characteristic for such interactions, are a real barrier for the conventional hydrodynamic approaches. PIC simulations make it possible to get insight in the physics of the electromagnetic field interaction with a target in the overdense plasma range (wake field generation, fast electron production [3,4], magnetic field generation) as well as in the underdense plasma range (generation of the ion beams, harmonic generation and so on).

PIC simulations can play crucial role during investigations of the fast ignition (FI) concept interesting for the author of this paper.

Recently, we have proposed a special method named laser-induced cavity pressure acceleration (LICPA) [5]. It was found that for high laser beam intensities of the order of 10^{22} W/cm² and for circular light polarization, a substantial increase in parameters of the accelerated ions is obtained when the target is placed inside a special cavity, into which the laser beam is introduced by a small hole. As compared to the pure radiation pressure acceleration (RPA) scheme, the LICPA scheme leads to an increase in ion energies and the laser-to-ions energy conversion efficiency. All above-mentioned investigations were made by use of custom-made one-dimensional particle-in-cell code PIC1D [6]. Results were very promissing but for a real application we must consider more accurate and realistic schemes. In order to approach to an experiment reasons for LICPA computation, two-dimensional particle-in-cell code PIC2D, presented below, was created.

Description of the PIC2D code

The code PIC2D is fully relativistic (both for electrons as well as for ions), pure electromagnetic code which makes it possible to exam such elements as: geometry of the cavity (input hole dimension, cavity width and height), the cavity wall parameters (reflection coefficients for the laser light, ions and electrons energy losses inside cavity), parameters of the target (its width and thickness, material of the target and target composition (metal target, two chemical elements plastic target, two layers target)) and parameters of the laser light (polarisation, intensity, pulse shape and length, beam convergence).

The main idea of the code is a combination of the Maxwell equations for the fields, and relativistic equations of motion for macro particles as well. It is assumed that main laser pulse propagats along Z axis and $\partial/\partial y=0$.

Changes in the field values (E and B) are calculated by the precise control and calculations of the current densities j. Presented code does not use Poisson solver for EM field calculation and dynamic problem of field evolution can be solved by means of the evolutionary, local equations for B fields and E fields alone. Maxwell equations were solved using of a shifted Euler grids for EM fields E, B and for current densities j. The discretized version of the Maxwell's equations is similar to the idea by K. S. Yee in [8]. The main difference seems to be the transformation of the first order equations for E_v and B_v into

wave equations for E_y and B_y . Such a procedure ensures an excellent stability of the Maxwell equations solver during computations.

The PIC2D algorithm does not use Poisson equation for electric and magnetic fields calculations and the EM fields are calculated by precise analysis of the current densities as it was mentioned above. The procedure responsible for this step of algorithm is similar to a concept proposed by J. Villasenor and O. Buneman in [9]. In this method a particle trajectory over one time step is assumed to be a straight line. In my case, the whole particle trajectory is divided into some subregions. The number of these subregions is dependent on cells number crossed by particle over time step. For each subregion an average current density is calculated. Calculations are realised by recursive procedure in order to eliminate to big number of "IF" statements what was the main objection of T. Umeda et al. [10] concerning the scheme by J. Villasenor and O. Buneman [9]. In the work of T. Umeda et al. [10], authors presented so-called "zigzag scheme" where a particle trajectory are not assmed to be stright line. Presently, it is a very popular method for solving the current density, due to the speed and simplicity. Unfortunately, when a particle trajectory crosses the cell meshes, a small numerical errors can occure in the case of "zigzag" scheme. This fact decided that I used Villasenor method instead of Umeda scheme. To solve the motion equations, I used a time centered scheme of Birdsall and Langdon [7].

In order to deliver more complete description of the PIC2D code, it is indispensable to write a few words about initial and boundary conditions taken into account by the author. At the beginning it is assumed that the charge of the plasma is thorougly balanced and all electric and magnetic fields on the numeric mesh are equal to zero. In the case of the LICPA scheme where simulation box is surrounded by perfectly conducting walls except small input hole (left side of the mesh) and completly open output space (right side of the mesh) as well as in the case of the RPA scheme where walls are absent, it is important to define a method for reflection elimination of electromagnetic waves from the free boundaries. In the code PIC2D for the last (boundary) point of mesh is solved equation $\partial A/\partial t \pm c \cdot \partial A/\partial r = 0$, where A should be substituted by E field or B field, c - speed of light. The sign plus or minus before c is dependent on direction of propagation of the EM wave.

An example of the results obtained from the PIC2D code

As an example, computations made for ELI laser system (1.3 kJ pulse of a 10 PW), where linearly polarised laser beam of intensity $I_L = 2*10^{22}$ W/cm² where pulse-length $\tau_L = 130$ fs and wavelength $\lambda = 0.8$ μ m interact with carbon target inserted or no inside the cavity, are presented. Time shape of the pulse is described by super-gaussian function of order $N_p = 6$. Laser beam profile is described by super-gaussian function of order $N_x = 6$ and beam width (FWHM) is equal to 2.8 μ m.

Starting parameters for the carbon target: maximum concentration of carbon ions $N_C = 1.0*10^{23}$ cm⁻³, target thickness $L_T = 100$ nm, exponential pre-plasma scale length $L_n = 250$ nm, initial temperature for this simulation $T_i = T_e = 0$ eV. The target was completely ionized and its charge was thoroughly balanced. Cavity parameters: width $W_{cav} = 6 \, \mu m$, length $L_{cav} = 40 \, \mu m$, input hole diameter $D_{cav} = 3.0 \, \mu m$. We assumed that cavity walls are perfectly conducting. Time step of simulation $\Delta t = 25.793$ as, space step $\Delta r = 15.465$ nm. Results for LICPA scheme and for no cavity scheme are taken for time t = 160 fs after the first contact of the laser pulse with target. In figure 1 the absolute value of the electric field $|E_y|$ as well as concentration of carbon ions (C^{6+}) and electrons are presented. As an appendix in Fig.1, energy spectrum for the carbon ions was added.

The complex structure of the electric field E_y as well as differences between both scheme of acceleration are shown. High intensity of the laser beam and small thickness of the target leads to its disruption. Trajectories of ions and electrons are very complex. However, even for such short time of interaction (t = 160 fs) between laser beam and target, the LICPA scheme seems to be more effective in acceleration of ions than in the case of the no cavity scheme. The first scheme gives more energetic ions than the second one (see energy spectrum in Fig. 1). For a longer time period this tendency is more

distinct (here it is not presented) due to retention of the beam inside cavity, when the LICPA scheme is in use. In both cases we have deal with TNSA mechanism (predominant for linear polarization) but it is not pure TNSA mechanism. Intensity of the order of 10^{22} W/cm² for starting an acceleration mechanism based on the radiation pressure acceleration effect (RPA) is sufficient. Both mechanisms can produce high energetic ions (for time t = 160 fs) of order 1 GeV and more.

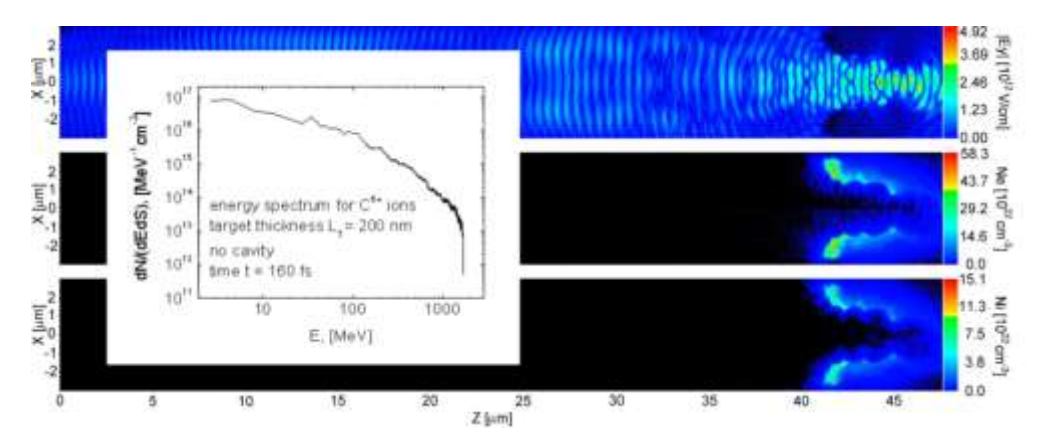


Fig. 1. The PIC2D results for laser acceleration of the carbon target for the no cavity scheme for time t = 160 fs. Top part - absolute value of a electric field E_y , middle part - concentration of the carbon ins, bottom part - concentration of the electrons, inset part - energy spectrum of the carbon ions. $\lambda = 800$ nm, $I = 2*10^{22} \text{W/cm}^2$, $\tau_1 = 130$ fs, linear polarisation, $L_T = 200$ nm, $L_D = 250$ nm.

It is very important to say that RPA mechanism as well as TNSA mechanism is present in both schemes of acceleration (LICPA, no cavity) but the author in Fig. 1 used RPA name as a synonim of the no cavity scheme.

Conclusion

As a conclusion, is worth emphasizing that presented above PIC2D code seems to be a very useful tool for investigations of laser-plasma interaction, especially for the high power laser systems ($I_L > 10^{18}$ W/cm²) and it is able to provide important information requested for real applications of a new methods of acceleration such as the LICPA scheme. At this time a special module answerable for modelling of the cavity walls is finalized. This modification will make it possible to take into account the influence of the plasma generated from the walls of the cavity on the processes in its interior.

References

- [1] D. Strickland and G. Mourou 1985 Opt. Comm. 56 219
- [2] M.D. Perry and G. Mourou 1994 Science 264 917
- [3] P. Gibbon 1994 Phys. Rev. Lett. 73 664
- [4] A. Pukhov and J. Meyer-ter-Vehn 1996 Phys. Rev. Lett. 76 3975
- [5] J. Badziak et al. 2012 Phys. Plasmas 19 053105
- [6] J. Badziak and S. Jabłoński 2010 Phys. Plasmas 17 073106
- [7] C.K. Birdsall and A.B. Langdon 1991 Plasma physics via computer simulation (Adam Hilger, NY)
- [8] K.S. Yee 1966 IEEE Trans. Antennas Propag. 14 302
- [9] J. Villasenor and O. Buneman 1992 Comput. Phys. Comm. 69 306
- [10] T. Umeda et al. 2003 Comput. Phys. Comm. 156 73